**METABOLIC REGULATION AT SUB-ORGANELLE LENGTH SCALES:**

**INTER-ORGANELLE CONTACTS AND LIPID DROPLETS**

APPROVED BY SUPERVISORY COMMITTEE

Mike Henne, Ph.D. (Supervisor)

Arun Radhakrishnan, Ph.D. (Chair)

Jen Liou, Ph.D.

Mike Rosen, Ph.D.

DEDICATION

I would like to thank my wife and best friend, Brandy Rogers,
my parents, Dale and Kelly Rogers, and
my mentor, Mike Henne

# MEATBOLIC REGULATION AT SUB-ORGANELLE LENGTH SCALES:

# INTER-ORGANELLE CONTACTS AND LIPID DROPLETS

by

SEAN W. ROGERS

DISSERTATION

Presented to the Faculty of the Graduate School of Biomedical Sciences

The University of Texas Southwestern Medical Center at Dallas

In Partial Fulfillment of the Requirements

For the Degree of

DOCTOR OF PHILOSOPHY

The University of Texas Southwestern Medical Center at Dallas

Dallas, Texas

December, 2021

METABOLIC REGULATION AT SUB-ORGANELLE LENGTH SCALES:

INTER-ORGANELLE CONTACTS AND LIPID DROPLETS

Sean W. Rogers

The University of Texas Southwestern Medical Center at Dallas, 2021

Supervising Professor: Mike Henne, Ph.D.

For cells to properly respond to environmental changes, cellular interiors must be exquisitely organized both spatially and temporally. In particular, metabolism must be spatially coordinated so metabolites are appropriately shunted into either storage or growth. Despite our understanding of how membrane-bound organelles organize metabolic processes, little is known about how metabolic regulation occurs at sub-organelle length scales. At these length scales, physical interactions between the endoplasmic reticulum (ER) and other organelles at ER-membrane-contact-sites (ER-MCSs) are now recognized as sub-organelle hubs for the regulation of metabolic processes. Our work uses the nucleus-vacuole-junction (NVJ) in *S.*

*cerevisiae* (yeast) as a model ER-MCS to further an understanding about potential general functions of ER-MCSs. We have noted that the NVJ, a physical connection between the nuclear-ER and the vacuole, is a hub for lipid metabolic enzymes and regulators.

When yeast are exposed to low glucose conditions, the NVJ recruits several metabolic proteins, including the enzyme Hmg1. Hmg1 catalyzes the conversion of HMG-CoA to mevalonate and is the rate-limiting enzyme in sterol biogenesis. We noted that Hmg1 is less catalytically active when Nvj1, the protein that recruits Hmg1 to the NVJ, is genetically ablated, or when Nvj1 lacks a minimal motif required to recruit Hmg1. Hmg1 NVJ partitioning is accompanied by its assembly into high molecular weight species, which may underlie its increase in enzymatic efficiency. Indeed, artificial tetramerization of Hmg1 overcomes the deficiencies of an Nvj1 knock-out. During Hmg1 partitioning, mevalonate is preferentially shunted into synthesis of sterol-esters (SEs), which are storage lipids found in large cytoplasmic organelles, lipid droplets (LDs). Coordinately, glucose starvation promotes the degradation of triglycerides (TAGs), the other major lipid species contained in LDs. We found that the SE/TAG imbalance in LDs during glucose starvation leads to a phase separation of SEs from a liquid to liquid-crystalline state. Upon SE phase separation, the proteome of LDs is considerably changed. Collectively, our studies of the NVJ have identified a novel function for an ER-MCS and connected it to a lipid metabolic circuit that controls the proteome of LDs.

## ACKNOWLEDGEMENTS

First, I want thank my mentor, Mike Henne. Mike's positivity and outlook on science fills me with hope and excitement. When I came to graduate school, I was certain about two things: 1) I wanted to use single-molecule techniques to study membrane organization and 2) I did not want to study metabolism. Mike single-handedly overturned both of those certainties, for the better. He introduced me to a new way of thinking about problems and allowed me to identify in myself a deep sense of curiosity. The environment that he has built is inquisitive, creative, and truly interdisciplinary. I hope that the future of science is filled with more people like Mike Henne.

I would like to thank all the members of the Henne lab, past and present: Hanaa Hariri, Anastasiia Kovalenko, Natalie Ortiz, Sanchari Datta, Rupali Ugrankar, Blessy Paul, Jade Bowerman, Chetana Jadhav, Ryan Feathers, Lydia Yang Liu, Emma Reynolds, and Son Tran. Every member of this lab has brought with them a unique perspective and experience that has shaped my time in graduate school. Particularly, Hanaa Hariri mentored me during my rotation in the Henne lab and was also responsible for recruiting me. I fed off her excitement for scientific discoveries, and I am honored to consider her a colleague. Anastasiia Kovalenko taught me what it was to teach and delegate. She is a phenomenal student, and I hope that I was half as good a mentor. All other members of the Henne lab have provided me endless feedback, advice, and laughter. I am truly grateful for every person here.

I would like to thank the members of my thesis committee: Arun Radhakrishnan, Jen Liou, and Mike Rosen. With every committee meeting, I walked out of the conference room feeling better than when I walked in. The advice, guidance, and perspective of all members has fundamentally shaped who I am as a scientist. It has been a great pleasure to be influenced by all three of these individuals and to witness their ways of dissecting problems.

I would like to thank some of the people who helped get me where I am today. Linda Blockus at the University of Missouri-Columbia steered me toward my first research job. She helped place me in Antje Heese's lab in the department of biochemistry, where I worked for the next four years. Antje is methodical, caring, and dedicates a significant portion of her time to training students. While in Antje's lab, I was mentored by Michelle Leslie, who showed an inhuman level of patience while teaching me everything from basic laboratory maintenance to fluorescence microscopy. Without Linda, Antje, and Michelle, I may have never realized that I wanted to pursue a career in research.

I would also like to thank my parents, Dale and Kelly Rogers. My parents ensured that I understood the value of hard work from an early age. They also made one thing very clear: that I would attend college. My parents valued education greatly, and I am forever indebted to them for instilling in me a sense of wonder about the workings of the world. I also must thank my older brother, Grady Rogers, for keeping me on my toes for my entire life. When I was young, I envied him for knowing things I hadn't yet learned in school. I am grateful for our small sibling rivalries that pushed me to learn more, and I am inspired by his willingness to debate any point, even when he knows he's wrong. He may not know it, but those trivial debates we had prepped me for dealing with manuscript reviewers.

Finally, I want to thank my wife, Brandy Rogers. It seems to me the journey of every scientist is filled with high-highs and low-lows. During the high times, Brandy is beside me to celebrate. During the low times, she guides me through troubles and ensures that my focus is kept on what is important. Life, and graduate school, have been made more delightful with Brandy by my side. Brandy is not just my wife, but my best friend and the mother of my two children, Liam and Logan. Science will always be my passion, but my wife and children give me purpose to be a better person every day.

## TABLE OF CONTENTS

## PRIOR PUBLICATIONS

Rogers S.*, Kovalenko A.* Gui L.*, Reetz E., Nicastro D., Henne WM. Liquid-crystalline lipid phase transitions selectively remodel the LD proteome. *BioRxiv*.

Rogers S., Hariri H., Wood NE., Speer NO., Henne WM. (2021) Glucose restriction drives spatial reorganization of mevalonate metabolism. *eLife*. PMID: 33825684.

Rogers S. and Henne WM. (2021) Analysis of Neutral Lipid Synthesis in Saccharomyces cerevisiae by Metabolic Labeling and Thin Layer Chromatography. *JOVE*. PMID: 33616103.

Ugrankar R., Bowerman J., Hariri H., Chandra M., Chen K., Bossanyi MF., Datta S., Rogers S., Eckert KM.,Vale G., Victoria A., Fresquez J., McDonal JG., Jean S., Collins BM., Henne WM. (2019) *Drosophila* Snazarus Regulates a Lipid Droplet Population at Plasma Membrane-Droplet Contacts in Adipocytes. *Dev Cell*, 50: 557-72 e5.

Hariri H., Speer NO., Bowerman J., Rogers S., Fu G., Reetz E., Datta S., Feathers RJ., Ugrankar R., Nicastro D., Henne WM. (2019) Mdm1 maintains endoplasmic reticulum homeostasis by spatially regulating lipid droplet biogenesis. *JCB*. PMID: 30808705.

Hariri H., Rogers S., Ugrankar R., Liu YL., Feathers RJ., Henne WM. (2018) Lipid droplet biogenesis is spatially coordinated at ER-vacuole contacts under nutritional stress. *EMBO Rep*. PMID: 29146766.

## LIST OF FIGURES

## LIST OF SUPPLEMENTARY FIGURES

## LIST OF APPENDICES

## LIST OF DEFINITIONS

| | |
|---|---|
| ER | Endoplasmic Reticulum |
| EM | Electron Microscopy |
| ER-MCS | ER-Membrane Contact Site |
| NVJ | Nucleus-Vacuole Junction |
| OMM | Outer Mitochondrial Membrane |
| IMM | Inner Mitochondrial Membrane |
| PM | Plasma Membrane |
| RCS | Respiratory Supercomplexes |
| CoQ | Coenzyme Q |
| FA | Fatty Acid |
| FFA | Free Fatty Acid |
| HMGCR | HMG-CoA Reductase |
| SE | Sterol-ester |
| LD | Lipid Droplet |
| NL | Neutral Lipid |
| PA | Phosphatidic Acid |
| PC | Phosphatidylcholine |
| PE | Phosphatidylethanolamine |
| DAG | Diacylglycerol |
| PS | Phosphatidylserine |
| PI | Phosphatidylinositol |
| TAG | Triacylglycerol |
| MAM | Mitochondria Associated Membranes |
| ERMES | ER-Mitochondria Encounter Structure |
| ORP | Oxysterol Binding Protein Related Protein |
| UPR | Unfolded Protein Response |
| PX | Phox Homology Domain |
| AH | Amphipathic Helix |

| | |
|---|---|
| AGR | Acute Glucose Restriction |
| BN-PAGE | Blue-Native Polyacrylamide Gel Electrophoresis |
| mNg | mNeonGreen |
| LCL-LD | Liquid-Crystalline Lattice Lipid Droplet |
| LC-MS/MS | Liquid Chromatography Mass Spectrometry |
| Cryo-FIB | Cryo-Focused Ion Beam |
| MDH | Monodansylpentane |
| OA | Oleic Acid/Oleate |
| DGAT | Diacylglycerol Acyltransferase |
| WT | Wild Type |

# CHAPTER ONE

## Introduction

### Background

Cells are constantly challenged by the need to create intricate, ordered, environments in the face of inevitable disorder. As such, cells survive by using clever devices to establish, maintain, and change their organization. Nearly five orders of magnitude separate individual atoms from full cellular systems; however, cellular persistence requires tight regulation at every level of this spatial continuum. Membrane-bound organelles, occupying hundreds of nanometers to a few micrometers, are perhaps the best characterized devices of cellular organization. Controlling biochemical pathway activity, mitigating the accumulation of toxic species, and balancing synthesis/degradation are all made possible, in part, by compartmentalizing biochemical pathways into distinct organelles. However, much less is known about how sub-organelle spatial scales, on the order of a few nanometers to hundreds of nanometers, contribute to cellular fitness.

Organelle sub-domains, portions of organelles with distinct compositions or morphologies, have now been confirmed to exist within every organelle (Kakimoto et al., 2018; Shai et al., 2018; Valm et al., 2017). The Endoplasmic Reticulum (ER) was one of the earliest organelles found to have distinct sub-domains, with the separation of smooth and rough ER being observed by early electron-microscopy (EM) (Porter et al., 1945). Early EM also revealed more intricate sub-domains of the ER including tubules, sheets, exit sites, and ER inter-organelle contact sites; however, these ER sub-domains were largely ignored until biochemistry and fluorescence microscopy provided further evidence for their existence (Vance, 1990; Voeltz et al., 2002).

ER inter-organelle contacts sites, or ER-membrane-contact-sites (ER-MCSs), are defined as sub-domains of non-random physical contact between the ER and at least one other organelle. Relative to their parent organelles, ER-MCSs possess a unique protein composition. Amongst

these proteins are molecular tethers, which enrich at ER-MCSs to hold organelle membranes in close-proximity via protein-protein or protein-lipid interactions (Eisenberg-Bord et al., 2016; Wu et al., 2018). Additionally, many tether proteins also function as recruitment factors by selectively enriching proteins at ER-MCSs to perform localized functions (Gatta and Levine, 2017). From here on, proteins that are recruited by ER-MCS tethers or enrich at ER-MCSs will be referred to as 'client' proteins. Client protein functions fall into several categories including ion transfer, lipid transfer, organelle positioning, organelle biogenesis, and signaling (Gatta and Levine, 2017; Wu et al., 2018). Amongst ER-MCS clients, non-vesicular lipid transport and ion transport between organelles represent two of the best characterized functions, and hereon will be referred to as 'canonical' client functions.

One key knowledge gap in the field includes understanding how non-canonical clients are modulated at ER-MCSs. Particularly, we lack mechanistic understanding about how ER-MCSs regulate enzyme function, organelle biogenesis, organelle fusion/fission, and promote general cellular homeostasis. The model organism *S. cerevisiae* (yeast) has been used extensively to address these questions due to its genetic malleability and the stability of many yeast ER-MCSs (Michel and Kornmann, 2012; Pan et al., 2000; Zaman et al., 2020). One ER-MCS in yeast, nucleus-vacuole-junction (NVJ), maintains a particularly staggering compositional plasticity, wherein clients from nearly all functional classes are recruited to the NVJ by distinct stress states (Kvam, 2004; Kvam et al., 2005; Pan et al., 2000; Roberts et al., 2003). Given this, the NVJ provides an exceptional opportunity to bridge the major knowledge gaps existing in both ER-MCS literature and our understanding of metabolic regulation at sub-organelle length scales.

My work is dedicated to understanding how partitioning of lipid metabolic enzymes at the NVJ regulates their function. Specifically, I have used the NVJ to begin addressing the following: 1) the influence of enzyme partitioning at an ER-MCS on enzymatic activity and 2) the down-stream effects of enzyme partitioning at an ER-MCS. Collectively, our work demonstrates that the NVJ functions as a metabolic scaffold by spatially organizing proteins during distinct stress

states. Spatial partitioning of proteins at the NVJ can influence enzyme activity, organelle biogenesis, resumption of cell growth following stress, and organelle lipid organization. The literature review below covers both historic perspectives and recent updates on the role of sub-organelle organization in regulating metabolic processes. Our work on the NVJ has found an unexpected home amongst this literature, connecting an ER-MCS to regulation of lipid metabolism and organelle biogenesis.

**Sub-organelle organization of metabolism**

*Metabolons and multi-protein complexes*

Sub-organelle organization occurs across a wide array of biological scales, ranging from the size of multi-subunit complexes to entire organelle sub-domains. As such, a few examples of metabolic regulation across this spatial continuum will be considered, beginning with the formation of multi-subunit metabolic complexes. Multi-subunit complexes catalyzing sequential reactions, or metabolons, were popularized by Paul Srere as a potential mechanism to regulate metabolic processes (Srere, 1972; Sumegi et al., 1991). One factor that distinguishes metabolons from other large cellular complexes, such as the ribosome, is the catalytic independence of complex formation. That is, each subunit of a metabolon carries an enzymatic activity which is not dependent on the formation of the complex. Partly because of this, metabolic regulation through formation of metabolons remained hypothetical for decades. In fact, explicit evidence of the TCA cycle metabolon was given only recently (Zhang et al., 2017), which underlies the technical difficulty not only to detect certain forms of sub-organelle metabolic regulation, but also to define the biochemical functions of these large, often transient, complexes.

What exactly, then, are the functions of a metabolon? Substrate channeling, the sequential passing of substrates and products from one enzyme to the next, was ranked as the primary function of these multi-component complexes at the inception of the metabolon hypothesis (Srere, 1972). Indeed, formation of the purinosome, a metabolon of nine enzymes responsible for purine biosynthesis, both increases enzymatic efficiency of purine biosynthesis, and biases

the conversion of inosine monophosphate to adenosine 5-monophosphate, over that of guanosine 5-monophosphate (Chan et al., 2015; Pedley and Benkovic, 2018). Therefore, metabolons may play multi-faceted roles in regulating enzyme activity, mitigating the accumulation of toxic species, and biasing the production of certain metabolites at metabolic branchpoints.

Although several direct observations of metabolons have now been made (Pedley and Benkovic, 2018; Puchulu-Campanella et al., 2013; Zhang et al., 2017), there remains a growing list of multi-enzyme metabolic complexes that do not clearly fit the metabolon mold. One clear demonstration of this is the formation of enzyme polymers or filaments. Most enzyme filaments form homopolymers (Park and Horton, 2019) and are observed to assemble in response to cellular stress states (e.g. starvation), which may indicate their role in adapting pathway fluxes to promote cellular survival. One example of an enzyme filament, acetyl-CoA carboxylase (ACC), assembles in the presence of high citrate concentrations (Kim et al., 2010; Meredith and Lane, 1978). ACC filamentation can either positively or negatively regulate its enzymatic activity (Beaty and Lane, 1983; Meredith and Lane, 1978). In one structural confirmation, ACC filaments increase enzymatic efficiency by ~60 fold by locking the enzyme in an active state, while two other filamentous confirmations of ACC inhibit enzymatic activity. Other examples of metabolic enzyme filamentation includes phosphofructokinase, glucokinase, CTP synthase, and glutamine synthetase (Lynch et al., 2017; Petrovska et al., 2014; Stoddard et al., 2020; Webb et al., 2017). While fluorescence microscopy and biochemical reconstitution has significantly aided the identification of enzyme polymers, several questions remain regarding their contribution to the adaption of cellular stress states.

Indeed, ongoing structural studies of both metabolons and enzyme filaments may aid in the identification of enzyme mutants that are catalytically active but deficient in the formation of complexes. If such backgrounds could be identified, a deeper understanding could be attained about the roles of metabolic complex formation in cellular homeostasis. Additional inquiry into how changing cellular environments promotes or prevents the assembly of metabolic

enzyme complexes will also be essential in dissecting the utilities of such complexes. As such, technology needs to be developed that empowers investigations into the physiochemical properties of sub-organelle compartments, such as local pH, ion concentrations, or membrane compositions. Another factor that complicates our understanding of the formation, maintenance, and function of multi-enzyme metabolic complexes is distinguishing between contributions of the individual complexes and the organellar sub-domains in which they occupy, which will be discussed below.

*Metabolic sub-organelle domains*

The advent of fluorescence microscopy brought with it a growing appreciation for the unequal distribution of proteins within organelles. Though dozens of organelle sub-domains have been identified to date, very little is known about how most of them participate in metabolic regulation. As mentioned above, it is technically challenging to distinguish between the contributions of organelle sub-domains in metabolism from the contribution of their principle lipid and protein components. However, at least one case has been rigorously studied for which parallels can be drawn to other systems.

Some of the most striking evidence for the roles of metabolic regulation by organelle sub-domains comes from the organization of the mitochondrion. Mitochondria have two membrane bilayers, the outer mitochondrial membrane (OMM) and inner mitochondrial membrane (IMM), whose structure and morphologies profoundly influence ATP generation. Particularly, the IMM is shaped into characteristically curved and elongated membrane protrusions known as cristae. Cristae, importantly, house all five of the multi-subunit respiratory complexes, which possess fascinating organizational properties across a wide spatial scale (Cogliati et al., 2016). Each respiratory complex is made up of several individual subunits that must be properly assembled and membrane-embedded for respiratory function (Kühlbrandt, 2015). Additionally, respiratory complexes have also been shown to associate with one another, forming high molecular weight respiratory chain supercomplexes (RCSs) (Dudkina et al., 2005; Lobo-Jarne and Ugalde, 2018). Recently, cristae assembly was shown to influence the

formation of RCSs (Gu et al., 2016; Guo et al., 2018), thereby controlling respiration through the curvature of this organelle sub-domain. Although the size, composition, and stoichiometry of RCSs appears to be different across distinct kingdoms of life, the relationship between cristae formation and RCS function is unmistakable. Therefore, mitochondrial respiration is a clear instance in which organization across a wide spatial scale, from the folding of individual proteins to the formation of highly curved cristae membranes, is necessary for normal cellular function.

Aside from the relationship between mitochondrial cristae and respirasome function, several other metabolic sub-domains have been identified in cellular environments, including caveolae at the plasma membrane, coenzyme Q domains at ER-mitochondria MCSs, and biomolecular condensates of metabolic enzymes in the cytoplasm (Jin et al., 2017; Parton et al., 2018; Subramanian et al., 2019). Though long observed, the mechanisms that govern their respective protein compositions, and thereby their influence on metabolism, remain to be discovered. As an extension of this, ER-MCSs have recently garnered attention as essential metabolic organelle sub-domains, particularly in the synthesis, transport, and organization of lipids. Before moving into the details of ER-MCSs, the introduction will next provide a brief overview of lipid synthesis in the ER so that we may appreciate the current understanding of the ER's participation in these processes from an organelle perspective before we consider the sub-organelle perspective.

**Lipid synthesis and regulation in the ER**

The ER is the major site of most cellular lipid synthesis. Due to the negative consequences that lipid excess or deficiency can have on cells, lipid synthesis, degradation, and transport are tightly regulated. Major lipids synthesized or regulated by the ER can be split into three general classes: sphingolipids, sterols, and glycerolipids. Below, the major roles of the ER in synthesizing and regulating each of these lipid classes will be described.

*Sphingolipid synthesis and regulation in the ER*

Before describing the roles of the ER in lipid synthesis, the basic building block of nearly all lipids must be considered: fatty acids (FAs). FA synthesis occurs primarily in the cytoplasm. It is initiated when ACC converts acetyl-CoA building blocks into malonyl-CoA (Wakil et al., 1983). Malonyl-CoA is the primary substrate of the fatty acid synthase complex (FAS; or FASN in higher eukaryotes) (Trotter, 2001; Wakil et al., 1983). FAS is a large multi-subunit enzyme complex that contains all of the enzymatic activities necessary to synthesize and elongate the acyl chain of FAs. In both animals and fungi, FAS progressively adds two-carbon units to a growing FA chain. However, FAS possess an acyl chain length limit of C16. Therefore, further chain elongation is performed by elongation of very long chain fatty acid (ELOVL) enzymes in the ER (Sassa and Kihara, 2014). From the ELOVL enzymes, cells can synthesize a range of C18 to C26 FAs.

Sphingolipid biosynthesis begins in the ER with the action of serine palmitoyl transferase (SPT), which is also the rate-limiting step of sphingolipid biosynthesis (Hanada, 2003; Lowther et al., 2012). Unlike many other lipids, sphingolipids bear a characteristic serine head group, which is attached to a fatty-acyl CoA by SPT. 3-ketodihydrosphingosine, the product of SPT, is a transient species which is quickly converted to dihydrosphingosine (Gault et al., 2010). Finally, the ER is responsible for the conversion of dihydrosphingosine to ceramide, through the action of ceramide synthases (Mullen et al., 2012; Wegner et al., 2016). This represents a branchpoint in sphingolipid metabolism. Both dihydrophingosine and ceramides can be further modified into complex sphingolipids and complex ceramides, respectively. However, much of this occurs outside of the ER (Wegner et al., 2016). Because ceramide accumulation in the ER can lead to ER stress, export of these species is very important (Park and Park, 2020). Ceramide can be trafficked from the ER to the Golgi via vesicular trafficking or through the action of the soluble ceramide transport protein CERT (Hanada et al., 2009). Ceramide and sphingolipids can also be regulated within the ER through degradation, which returns serine and fatty acyl-CoA as byproducts. Regardless of the well characterized mechanisms for synthesizing and degrading sphingolipids in the ER, much remains to be

discovered about the ways in which sphingolipid metabolism and distribution is regulated in a cellular context.

*Sterol synthesis and regulation in the ER*

In humans, *de-novo* biosynthesis of cholesterol, the predominant cellular sterol, is carried out by twenty enzymes and begins with acetyl-CoA as a substrate (Jordá and Puig, 2020; Luo et al., 2020). The first eleven steps of sterol biogenesis, conversion of acetyl-CoA to lanosterol, are conserved from yeast to humans. However, the pathways differ after this step, which results in the synthesis of cholesterol for humans and ergosterol in yeast (Burg and Espenshade, 2011). The early steps of sterol production occur in the cytoplasm and are amenable to a soluble environment. But later steps in sterol synthesis result in highly hydrophobic compounds such as squalene, which requires a membrane medium for efficient substrate partitioning and catalysis. Though the late-stage steps of sterol biosynthesis can occur in a few different membrane compartments, the ER is undoubtedly a focal point for both sterol synthesis and homeostasis.

The rate limiting step of sterol biosynthesis is the conversion of HMG-CoA to mevalonate by the ER enzyme HMG-CoA Reductase (HMGCR) (Burg and Espenshade, 2011). HMGCR is present in all kingdoms of life and has a conserved mechanism of catalysis (Istvan, 2001). Eukaryotic HMGCRs typically have between two to eight ER-embedded transmembrane domains and a c-terminal catalytic domains that faces the cytoplasm (Burg and Espenshade, 2011). In humans, HMGCR forms a tetramer, a dimer of dimers, and the active sites are formed at the monomer-monomer interfaces; therefore, residues from each monomer participate in catalysis (Istvan et al., 2000). While the catalytic portion of HMGCR lies in the cytoplasm, much of the known mechanisms for HMGCR regulation occur through the ER membrane domains (Hampton et al., 1996; Rodwell et al., 1976). Due to highly active sterol export from the ER, sterol concentrations in the ER are kept low in normal high-nutrient conditions (~5 mol%). If ER cholesterol content falls below 5 mol%, the membrane-bound transcription factor sterol-regulatory-element-binding-protein (SREBP) is trafficked from the ER to the Golgi

(Radhakrishnan et al., 2008). Once at the Golgi, the membrane anchor of SREBP can be cleaved, which allows for translocation to the nucleus and subsequent activation of the HMGCR gene. HMGCR is also regulated at the protein level, in part, through its binding partner insulin-induced-gene (INSIG) (Jo and Debose-Boyd, 2010). When ER cholesterol content rises above 5 mol%, INSIG forms a complex with HMGCR and recruits proteins that conjugate ubiquitin to HMGCR. Once ubiquitinated, HMGCR is targeted for degradation by the proteasome. Similarly, yeast HMGCRs (there are two redundant orthologs—Hmg1 and Hmg2) are regulated at both the transcriptional and translational levels. During sterol-depleted conditions, two membrane-embedded transcription factors, Upc2 and Ecm22, can translocate to the nucleus and activate transcription of genes involved in sterol biosynthesis and uptake (Yang et al., 2015). Yeast HMGCRs, Hmg1 and Hmg2, are also regulated at the protein level via proteasomal degradation during sterol replete conditions; however, the specific molecular components responsible for this process are less clear (Hampton and Bhakta, 1997; Hampton and Rine, 1994).

Other than export of sterols from the ER, other mechanisms exist to ensure cells don't accumulate excess sterol in the ER. First, isoprenoids derived from mevalonate can be shunted into several pathways, rather than being processed into sterol. Specifically, isoprenoids are used in CoQ synthesis, dolichol synthesis, and protein prenylation (Szkopińska et al., 1993; Turunen et al., 2004; Wang and Casey, 2016). Though the mechanisms governing the synthesis of all of these species are relatively well characterized, how cells dictate the amount of isoprenoids destined for sterol versus other non-sterol species is not thoroughly understood. Finally, excess sterol in the ER can also be converted to sterol-esters through the action of acyl-coenzyme a-acyltransferase (ACAT) enzymes (Chang et al., 1997). Sterol-esters (SEs) are stored inside of cytoplasmic organelles called lipid droplets (LDs), which act as neutral lipid (NL) reservoirs and will be the topic of a subsequent section.

*Glycerolipid synthesis and regulation in the ER*

Glycerolipid synthesis, and glycerophospholipid synthesis as an extension, begins in the ER with the rate limiting enzyme glycerol-3-phosphate acyl transferase (GPAT) (Henry et al., 2012; Vance, 2015). GPAT conjugates a long chain fatty acyl-CoA to glycerol-3-phosphate to produce lysophosphatidic acid (Lyso-PA). Lyso-PA is further acted upon by 1-acyl-glycerol-3-phosphate-O-acyltransferase (AGPAT) to add a second fatty acyl-CoA to lyso-PA and create phosphatidic acid (PA). PA acts as a central lipid in glycerolipid synthesis and turnover because it can be shunted either into storage lipids or further processed into membrane phospholipids for growth (Barbosa et al., 2015). In both cases, regulation of ER enzymes is essential for choosing between these two fates for PA.

Phosphatidylcholine (PC), the most abundant phospholipid in yeast and humans, can be made through two pathways: The Kennedy pathway or conversion from phosphatidylethanolamine (PE) (Vance, 2015). The Kennedy pathway is the predominant means of producing PC in yeast and in most mammalian tissues (Gibellini and Smith, 2010). PA can be converted to diacylglycerol (DAG) by ER-bound phosphatidic acid phosphatase (PAP/Lipins in humans; Pah1 in yeast), which marks the beginning of the Kennedy pathway (Zhang and Reue, 2017). Finally, CDP-choline can be attached to DAG for the production of PC. Though PC synthesis enzymes can be found in multiple compartments, the ER undoubtedly acts as a major source for the supply of this lipid. Similar to PC synthesis, PE can be synthesized in the ER by addition of CDP-ethanolamine to DAG. Alternatively, PE can be made through de-carboxylation of phosphatidylserine (PS); however, this reaction likely happens predominantly in the mitochondria. PS is synthesized differentially in mammalian cells and yeast cells. In mammals, PS can be synthesized in the ER from either PE or PC by a base exchange reaction (Vance, 2015). However, PS in yeast is synthesized by a PS synthase reaction that conjugates serine to CDP-DAG (Henry et al., 2012). CDP-DAG also functions as a necessary precursor for phosphatidylinositol (PI) species. Though PI and PIPs perform several important biological functions, their synthesis, regulation, and transport will not be discussed in this section. Finally, PA and DAG can be shunted away from phospholipid synthesis by conversion of DAG to triacylglycerol (TAG). Diacylglycerol-acyltransferase (DGAT1/2 in humans, Dga1/Lro1 in

yeast) conjugate FFA to DAG to create TAG (Bhatt-Wessel et al., 2018; Sorger and Daum, 2003). TAG is a storage lipid which is found almost solely in LDs. Energy can be harvested from the acyl-chains of TAG via β-oxidation, wherein even a single TAG molecule can generate a significant number of ATP molecules (>100). The storage of TAG into LDs will be the focus of a subsequent section.

*Regulation & Trafficking of lipids between organelles*

Glycerolipids can be regulated through multiple pathways that involve the ER. Though much has been discovered regarding the mechanisms of glycerolipid regulation in the ER, I will focus on two points: 1) regulation of glycerolipids by DAG/PA formation and 2) trafficking of phospholipids via the ER. Dephosphorylation of PA by PAP/Pah1 marks an important event in phospholipid regulation because it creates a free pool of DAG that can undergo several fates (Barbosa et al., 2015). As such, how PAP/Pah1 is regulated has been an area of intense investigation. First, the action of PAP/Pah1 is set against the reverse reaction catalyzed by diacylglycerol kinase (DGK), which phosphorylates DAG to produce PA (Ericson et al., 1987). Balancing the protein levels of PAP/Pah1 and DGK in cells can significantly alter the respective pools of these lipids. PAP/Pah1 is also regulated by binding to the ER. When cells are treated with excess FFA, PAP/Pah1 re-localizes from the cytoplasm to the ER to increase the cellular pool of DAG that can be converted to TAG (Zhang and Reue, 2017). PAP/Pah1 is also sensitive to the membrane environment. CDP-DAG, PI, and cardiolipin have been shown to increase PAP/Pah1 activity; however, activity is decreased by several sphingolipid species (Wu and Carman, 1996; Wu et al., 1993). Finally, phosphorylation is a key modulator of PAP/Pah1. For Pah1 in yeast, the Spo1/Nem7 phosphatase acts on Pah1 to promote its translocation to the ER and subsequent increase in activity (Mirheydari et al., 2020).

Because the ER is the major source of *de-novo* phospholipid synthesis, multiple mechanisms must exist to export phospholipids from the ER to other compartments. As for proteins, phospholipids can be supplied through the secretory pathway in the form of vesicles (Yang et al., 2018). This was the predominant hypothesis for several years; however, some organelles

like the mitochondrion are not connected to canonical vesicular traffic. Additionally, trafficking of proteins from the ER to the PM appears to be significantly slower than the trafficking of certain phospholipids from the ER to the PM (Yaffe and Kennedy, 1983). This raised several questions about alternative routes for ER export of phospholipids. Close apposition of the ER with virtually every other organelle has been observed for several decades by electron microscopy (Porter et al., 1945). However, these sites were mostly overlooked as artifacts of sample preservation or the crowding of cellular environments. More recent imaging using fluorescence markers like GFP, together with live-cell imaging, has also revealed that organelles make extensive contacts with one another (Shai et al., 2018; Valm et al., 2017).

In addition to imaging MCSs, numerous functions for MCSs in cell physiology have also been revealed. In 1990 Jean Vance identified a biochemically isolated fraction of mitochondria which showed increased activity for enzymes thought to exist solely in the ER (Vance, 1990). Later, this fraction was attributed to co-isolation of ER membranes tethered to mitochondria, ER-MCSs. After several decades of work, we now know that ER-MCSs are major cellular junctions for the exchange of lipids between membranes. Though new functions of ER-MCSs are being uncovered rapidly, the germinal discovery of ER-MCSs was connected to lipid synthesis and exchange.

**Architectures and functions of ER-MCSs**

The ER is an expansive organelle that carries the brunt of cellular anabolic metabolism. To properly respond to environmental cues, the ER needs to keep open lines of communication with every other cellular organelle. Rather than trying to cover the extensive list of functions and components found at ER-MCSs, I will instead focus on three points: 1) major tethering complexes at ER-MCSs and their best characterized client proteins, 2) ‘canonical’ functions performed across different ER-MCSs, and 3) the current interpretation about why these functions are best performed at ER-MCSs. The following sub-sections address the above three points for ER-Mitochondria (ER-Mito), ER-PM, and yeast ER-Vacuole contact sites, which

have served as model ER-MCSs. The goal of this section is to attain an appreciation for ER-MCSs as sub-organelle modulators of biochemical processes.

*Tethers and functions of ER-Mito MCSs*

Continuing from the above discussion of phospholipid metabolism, PE can be either synthesized from PC in the ER or from PS in the mitochondrion. However, mitochondria lack the enzymes for PS synthesis. Early studies of mitochondria-associated membranes (MAMs) identified enrichment of PS and PE synthesis enzymes in biochemically isolated MAM fractions (Vance, 1990). The prevailing model was that ER-Mito MCSs facilitated a cycle of PS transport from the ER to the mitochondria, whereby it could be converted into PE and transferred back to the ER. While several elegant biochemical investigations have provided strong evidence for the transport of PS via ER-Mito MCSs, the influence of MAMs on PE synthesis and export from mitochondria has not been clearly demonstrated to date.

The clearest example for a lipid transfer function at ER-Mito MCSs comes from investigations of the yeast ER-mitochondria encounter structure (ERMES). ERMES constitutively tethers ER to mitochondria via the proteins Mdm34, Mdm10, Mdm12, and Mmm1 (Kornmann et al., 2009). As expected, deletion of the ERMES tethering complex reduces conversion of PS to PE (Kawano et al., 2018; Kojima et al., 2016; Michel and Kornmann, 2012). Replacement of the ERMES complex with an artificial tethering system is partially sufficient to restore PS to PE conversion in ERMES deletion cells. However, whether ERMES functions solely as a tether or as a direct shuttle of lipids is still debated (Kawano et al., 2018; Nguyen et al., 2012). It is likely that loss of ERMES can be compensated by increased contact from other MCSs (i.e. the vacuole-mitochondria patch (VCLAMP)) (Elbaz-Alon et al., 2014). Additionally, the ERMES complex proteins Mdm12, Mmm1, and Mdm34 contain synaptotagmin-like mitochondrial lipid binding protein (SMP) domains, which are found in soluble lipid transport proteins (AhYoung and Egea, 2019; Alva and Lupas, 2016). Several ERMES client proteins also bear lipid transfer functions, including the proteins Ltc1/Lam6 and Vps13 (Elbaz-Alon et al., 2015; Jentsch et al., 2018; Lees and Reinisch, 2020; Tong et al., 2018). Collectively, ERMES appears

to be a hub for lipid transfer between the ER and mitochondria. Aside from lipid transfer, the early biochemical evidence pointing to enrichment of phospholipid processing enzymes in MAMs has not been corroborated by live-cell imaging for ERMES. While early discovery of MAMs pointed to a clean-cut model for ER to Mito lipid transport, more investigation is needed to mechanistically explain how ER-Mito MCSs participate in mitochondrial PE synthesis and export.

No homologues of ERMES have been identified in mammalian cells to date, but extensive contacts between the ER and mitochondria still exist. Whereas yeast ERMES has been more clearly demonstrated to participate in lipid exchange between ER and Mitochondria, mammalian ER-Mito MCSs have more clear roles in calcium transfer, mitochondrial fission, and autophagy (Belgareh-Touzé et al., 2017; Bononi et al., 2012; English et al., 2020; Friedman et al., 2011; Hirabayashi et al., 2017; Yang et al., 2020). Mammalian ER can be tethered to mitochondria through at least two protein complexes: 1) IP3R3-Grp75-VDAC1 and 2) VAPB-PTPIP51 (Bartok et al., 2019; Basso et al., 2020; Gomez-Suaga et al., 2017). Briefly, IP3R3 is an ER $Ca^{+2}$ ion channel that controls the release of $Ca^{+2}$ from the ER lumen (Mikoshiba, 2007). Likewise, VDAC1 (voltage-dependent-anion-channel 1) is the major anion uniporter localized on the OMM (Blachly-Dyson and Forte, 2001). The cytosolic protein Grp75 can bridge these two ion channels, which facilitates $Ca^{+2}$ transfer from the ER lumen to the inner membrane space of the mitochondria (Bartok et al., 2019). Similarly, the ER membrane protein VAPB can bind to the OMM protein PTPIP51 to mediate calcium homeostasis at the ER-Mito interface (Gomez-Suaga et al., 2017).

Indeed, $Ca^{+2}$ transfer between organelles is a trademark function of ER-MCSs; however, a long-standing question in the field is whether ER-MCSs possess unique physiochemical environments (e.g. distinct local $Ca^{+2}$ concentrations or lipid compositions), or if ER-MCSs simply aid biochemical reactions by bridging two organelle membranes. While the physiochemical properties of ER-MCSs is not well understood, they clearly have distinct protein compositions relative to their resident organelles (Cho et al., 2020; Lee and Min, 2018;

Montesinos and Area-Gomez, 2020). ER-Mito MCSs have been reported to enrich greater than 60 proteins, pointing to a compositional complexity that is just now being understood (Cho et al., 2020). To add to this existing complexity, the protein composition of ER-MCSs is dynamic and sensitive to environmental cues. For example, ERMES contacts expand significantly during times of cellular respiration, which may function to recruit yet unidentified ERMES clients (Kornmann et al., 2009). Collectively, our understanding of how ER-MCSs function throughout different organisms will be reliant, in part, on our understanding of their resident protein and lipid compositions. One factor that controls the composition of ER-MCSs are the resident tethers themselves. The ER-Mito tether VAPB acts not only as a tether, but also as a scaffold protein to recruit clients such as the high molecular weight lipid transfer protein Vps13 (Kumar et al., 2018). As with ER-Mito MCSs, lipid and calcium transfer occurs at other ER-MCSs and will be discussed further in the subsequent sections.

*Tethers and functions of ER-PM MCSs*

Unlike ER-Mito MCSs between yeast and humans, many tethers found at ER-PM contacts have been conserved throughout evolution. A few of the conserved and best characterized ER-PM tethers fall into three distinct protein families, given here as (human/yeast): **1**) TMEM16/Ist2, **2**) (VAPA/VAPB)/(Scs2/Scs22), and **3**) extended synaptotagmins (E-Syts)/tricalbins (Tcb1/2/3) (Manford et al., 2012; Zaman et al., 2020). While very little is known about the individual function of yeast Ist2, the physiological roles played by the other two ER-PM classes are better described.

As mentioned in the above section, VAPB functions as an ER-Mito tether. However, VAPs can be found at several ER-MCSs, which is likely controlled by their phosphorylation (Di Mattia et al., 2020; Kumar et al., 2018). At ER-PM contacts, VAPs are thought to bridge the space between ER and PM while also recruiting several client proteins via their FFAT motifs (Murphy and Levine, 2016). One of the best characterized clients of VAP are those in the oxysterol-binding-protein-related-protein (ORP) family. ORPs are canonical ER-MCS clients that mediate transfer of sterols and PS from the ER to the PM (Ghai et al., 2017; Naito et al.,

2019; Sohn et al., 2018; Wong et al., 2021). In exchange, phosphoinositide-4-phosphate (PI4P) is transferred from the PM to the ER in counterflow, which is thought to aid in moving sterol/PS up their concentration gradient (Moser von Filseck et al., 2015; Sohn et al., 2018). As a part of this cycle, the PI4P phosphatase, Sac1, also enriches at ER-PM contacts (Dickson et al., 2016; Zewe et al., 2018). Localization of Sac1 supports a model where incoming PI4P from the PM can be converted to PI, whereby it can be transferred from the ER back to the PM by another set of lipid transfer proteins, Nir2/3. Nir2 and Nir3 transfer PA from the PM to the ER in counterflow, which can be converted back to PS in the ER (Chang and Liou, 2015; Kim et al., 2015). Altogether, a significant amount of data now supports ER-PM contacts as being enriched for lipid synthesis and exchange circuits that allow for the movement of lipids up their concentration gradients.

As expected, ablation of all six ER-PM tethers in yeast disrupts the volume of ER in close proximity to the PM, which is accompanied by a disruption of phosphoinositide signaling from the PM (Manford et al., 2012). One unexpected outcome of disconnecting the ER from PM is an activation of the unfolded protein response (UPR), pointing to a yet unknown role for ER-PM MCSs in mitigating ER stress (Manford et al., 2012). One possible mechanism for activation of UPR during ER-PM MCS ablation is through mis regulation of phospholipid trafficking. Alternatively, disruption of cellular calcium signaling could be the culprit; however, these two mechanisms are not necessarily mutually exclusive. In fact, several PM surface receptors activate phospholipase C (PLC), which hydrolyzes phosphoinositide bisphosphates ($PIP_2$) from the PM to create $IP_3$. $IP_3$ can subsequently bind to ER $Ca^{+2}$ channels leading to a release of ER luminal $Ca^{+2}$ into the cytoplasm. To rapidly regenerate PM $PIP_2$ levels, PI is transferred from the ER and further converted to $PIP_2$ at the PM. Altogether, the cooperation of lipid synthesis, lipid transport, and calcium signaling at ER-PM MCSs represents one of the best characterized biochemical circuits localized at an ER-MCS, but still requires significant investigation to understand its regulation and underlying role in cellular homeostasis.

As with other ER-MCSs, several questions remain about the functions and architectures of ER-PM MCSs. Some evidence from yeast ER-PM MCSs suggests that not all ER-PM contacts are compositionally the same. The three classes of yeast ER-PM tethers can occupy distinct regions with little to no overlap, pointing to another layer of complexity to be investigated (Hoffmann et al., 2019). Also, it is unknown whether localization of enzymes, like Sac1, at an ER-PM MCS influences enzyme function. Early reports proposed that ER-bound Sac1 may directly catalyze conversion of PI4P to PI at the PM in trans, without need to first transfer PI4P to the ER. Undoubtedly, there is much work to be done to uncover both how compositional control is established at ER-MCSs and the influence of partitioning enzymes at an ER-MCS on enzyme function.

*Tethers and functions of the Nucleus-Vacuole Junction (NVJ)*

Aside from MAMs, the NVJ in *S. cerevisiae* was one of the first observed ER-MCSs. The NVJ consists of a physical tethering between the nuclear envelope and the vacuole, which is maintained by at least two tethering systems. The tether Nvj1 was first identified biochemically when Goldfarb and colleagues searched for novel binding partners of the vacuole protein Vac8 (Pan et al., 2000). The authors also noted that Nvj1 was ER-embedded and localized to a sub-portion of the nuclear envelope that was always adjacent to the vacuole. Using structure-function analyses, the N-terminal domain of Nvj1 was found to reside in the ER lumen, where it may interact with the inner nuclear envelope via a hydrophobic domain (Kvam, 2004; Kvam et al., 2005; Roberts et al., 2003). Nvj1 crosses the ER membrane via a single-pass transmembrane domain and contains a large cytosolic portion capable of recruiting several client proteins to the NVJ. Nvj1 is predicted to be predominantly unstructured, but some evidence suggests that it may become more rigid upon binding to Vac8 or client proteins (Jeong et al., 2017; Manik et al., 2017). Fluorescence microscopy has allowed for the identification of over a dozen protein clients that can localize to the NVJ. These proteins function in autophagy, lipid synthesis, organelle biogenesis, lipid transfer, and proteostasis (Barbosa et al., 2015; Hariri et al., 2018, 2019; Kvam, 2004; Kvam et al., 2005; Roberts et al., 2003).

Unlike ER-PM MCSs, the potential connection amongst all NVJ clients is unclear. Additionally, many NVJ clients are recruited to the NVJ only under distinct stress states, pointing to an unidentified mechanism for compositional plasticity at the NVJ. During nitrogen starvation both the fatty acid elongase, Tsc13, and the proposed soluble lipid transport protein, Osh1, enrich at the NVJ (Kvam, 2004; Kvam et al., 2005). Meanwhile, glucose deprivation leads to recruitment of the client protein Snd3, which serves a role as a chaperone during ER membrane protein insertion (Tosal-Castano et al., 2021). Further, certain metabolic states promote the enrichment of lipid transport proteins Vps13 and Ltc1/Lam6 at the NVJ (Elbaz-Alon et al., 2015; Lang et al., 2015). Much is to be discovered about how the NVJ regulates each client protein, but one unmistakable theme amongst NVJ client functions is their participation in lipid metabolic processes.

Several clients with canonical ER-MCS functions enrich at the NVJ, as mentioned above. These clients include Vps13, Ltc1/Lam6, and Osh1. All three proteins share a putative function for non-vesicular lipid transport. Osh1 is homologous to the mammalian ORP proteins discussed in the ER-PM MCS section. Like its mammalian homologues, Osh1 can bind both PI4P and sterol (yeast ergosterol in the case of Osh1). Osh1 binds Nvj1 through an Ankyrin repeat domain during stress states that promote NVJ expansion (Kvam, 2004). While at the NVJ, Osh1 is proposed to transfer ergosterol and PI4P between the perinuclear ER and the vacuole. Interestingly, the PI4P phosphatase Sac1 can also enrich at the NVJ, which may suggest a circuit of phosphoinositide exchange exists at the NVJ, as it does at ER-PM MCSs (Stefan et al., 2011). Lam6/Ltc1 is shown to reside at several ER-MCSs, including ERMES (Elbaz-Alon et al., 2015). Lam6/Ltc1 contains a START domain that can bind and transfer sterol between liposomes *in-vitro* (Tong et al., 2018). Overexpression of Lam6/Ltc1 also results in the physical expansion of several ER-MCSs, hinting at its potential role as an ER-MCS tether. Though much work is now being performed on Lam6/Ltc1, its *in-vivo* function is still up for debate. Vps13 is a non-vesicular lipid transporter that has recently stolen the spotlight in the ER-MCS community. Unlike the previously described lipid transfer proteins, Vps13 seems to transfer several lipid molecules at a time, acting like a ‘lipid shuttle’ or ‘lipid

syringe' between organelle membranes. Like Lam6/Ltc1, Vps13 localizes to several ER-MCSs in yeast and humans, which is predominantly controlled by the tethers of the respective ER-MCS. Vps13 does not appear to selectively bind any lipid; rather, it is thought that hydrophobic grooves within the rod-shaped structure allow for transport of lipids down their concentration gradient. Along these lines, Vps13 may localize to sites where lipids are in high demand, like sites of autophagosome biogenesis.

While the function of canonical transfer proteins may obviously benefit from localization at ER-MCSs, the function for localizing several non-canonical clients to the NVJ remains a mystery. One clue may reside in the NVJ enrichment of the non-canonical ER-MCS client protein, Pah1. As discussed previously, Pah1 is an enzyme that PA to DAG upon binding to the ER. Some genetic mutants of Pah1 that are constitutively active localize exclusively to the NVJ (Barbosa et al., 2015). Whether the NVJ possesses a unique lipid composition that promotes Pah1 binding or whether Pah1 becomes more active at the NVJ remains to be uncovered. Furthermore, how the NVJ influences clients with non-canonical ER-MCS functions, like the enzymes Pah1 and Tsc13, will be instrumental in understanding ER-MCS client functions elsewhere. Because of its compositional heterogeneity, responsiveness to stress states, and link to several biochemical pathways, the NVJ has been used as a 'model ER-MCS' to better understand the foundational utilities of ER-MCSs elsewhere.

More than a decade after the discovery of the Nvj1-Vac8 tethering complex, the protein Mdm1 was identified to function as an independent NVJ tether (Henne et al., 2015). Mdm1 is an ER integral membrane protein that binds the vacuole via a c-terminal PI3P-binding Phox Homology (PX) domain (Yu and Lemmon, 2001). During the post-diauxic shift and stationary growth phases in yeast, LD biogenesis is upregulated, wherein LDs become spatially concentrated at the NVJ. Our group identified that NVJ LD positioning is mediated by Mdm1 (Hariri et al., 2018, 2019). Artificial re-localization of Mdm1 to other ER-MCSs is sufficient to re-define sites of LD biogenesis. While the biochemical mechanisms for spatial control of LD biogenesis is unclear, Mdm1-mediated positioning of LDs appears to be important for

mitigating ER stress (Hariri et al., 2019). While not conclusive, one attractive model is that Mdm1 works with FFA processing machinery to define the fates of FFAs toward storage or membrane biogenesis.

Though Mdm1 and Nvj1 spatially share an ER-MCS, these tethers are functionally distinct in most cases. All NVJ clients identified to date have been exclusively recruited by either Nvj1 or Mdm1, with no overlap between these tethers. Nvj1 and Mdm1 also occupy different spatial patterns within the NVJ. In three dimensions, the NVJ resembles a disk with Nvj1 occupying the 'core' and Mdm1 residing in the 'periphery' of the disk (Hariri et al., 2018). Intriguingly, deletion of Nvj1, Mdm1, or both tethers together give distinct cellular phenotypes which may point to some cooperativity between these tethers.

One landmark achieved by studying the NVJ is an appreciation that ER-MCSs do not exist solely to hold organelle membranes in close proximity. Some functions may obviously become more efficient when occurring at ER-MCSs (e.g. non-vesicular lipid transport between the ER and other membranes). Other client proteins may not require apposition to another organelle, per se, but instead be regulated at an ER-MCSs via a concentration effect within their resident organelle (e.g. concentration of lipid metabolic enzymes like Tsc13). Therefore, ER-MCSs like the NVJ may be spatial platforms used to regulate processes involving all the organelles at a junction, while also serving to concentrate processes within a single organelle. Though some examples of the down-stream effects for lipid transfer and $Ca^{+2}$ homeostasis have been mapped for ER-MCSs, the influence of clustering dozens of other clients remains to be explored. For the NVJ, clients involved in lipid metabolism may ultimately influence LD biogenesis or turnover, as per the connection with Mdm1. Below, the current understanding of LD biology will be described to serve as a reference for later findings.

**Lipid droplet biogenesis, protein targeting, and compositional control**

*Lipid droplets biogenesis*

LDs are the major NL storage organelle throughout all eukaryotes. LDs are peculiar organelles that lack an aqueous interior. Instead, LDs are composed of a NL 'core' encased by a phospholipid monolayer (Walther et al., 2017). LD biogenesis begins with the synthesis of SE and TAG in the ER bilayer. When the NL composition of the ER reaches a critical threshold, the NLs can phase separate between the acyl chains of the phospholipid bilayer, creating a structure called a lens (Thiam et al., 2013).

In the current model of LD biogenesis, proteins like Seipin and LDAF/Promethin recognize NL lenses within the ER bilayer, wherein they can bind to and promote the growth of lenses into mature LDs (Castro et al., 2019; Chung et al., 2019). As mentioned for Mdm1, sites of LD biogenesis in the ER appear to be non-random. Artificial re-localization of Seipin to ER-PM MCSs is sufficient to also re-localize nascent LDs to this site (Chung et al., 2019). It is possible that Seipin not only recognizes LD lenses in the ER bilayer, but helps promote their stability. Interestingly, LD biogenesis sites in the ER are also sites of peroxisome biogenesis, suggesting organelle biogenesis sites in the ER are distinct metabolic sub-domains (Joshi et al., 2018).

One property of organelle biogenesis sites that may make them amenable to LD biogenesis is a distinct lipid composition across each leaflet of the bilayer. LDs predominantly bud from the ER bilayer away from the ER lumen and toward the cytoplasm. In times of FFA overload, the cell can also create LDs that bud toward the nucleus, but these events are quite rare (Romanauska and Köhler, 2018). For several years, those interested in LD biology wondered about the mechanisms controlling directional LD budding into the cytoplasm. Using beautiful *in-vitro* models, Thiam and colleagues showed that bilayer tension across one leaflet can control which direction LDs bud (Chorlay and Thiam, 2018; Chorlay et al., 2019). For proper directional budding and LD size control, the cytoplasmic leaflet of the ER bilayer needs to decrease surface tension in the face of a growing LD lens. If the ER bilayer carries too much tension, a significantly larger lens will be required to escape the ER bilayer, leading to larger mature LDs. Though LD biogenesis can be recapitulated *in-vitro* without proteins, it is likely that several proteins, like Seipin, help control the tension of the ER bilayer during LD budding.

Indeed, Seipin deletion cells accumulate super-sized LDs, consistent with a tension imbalance in the ER (Cartwright et al., 2015; Wang et al., 2016).

Phospholipid composition of the ER likely also plays an important role in directional LD budding. Treatment of giant-unilamellar-vesicles (GUVs) with phospholipase $A_2$ ($PLA_2$), which converts PC to lyso-PC, decreases surface tension on one leaflet of a bilayer (Ben M'barek et al., 2017) and promotes LD budding *in-vitro*. As expected, knock-out of $PLA_2$ in cells results in larger LDs, much like a Seipin knock-out, which is consistent with a model of tension-controlled LD budding from the ER. Altogether, both *in-vitro* and *in-vivo* data agree that control of the ER phospholipid content, and membrane physical properties therein, significantly influences LD budding from the ER and the downstream size distribution of LDs.

One remaining question in the field of LD biogenesis is whether LDs stay attached to the ER throughout their entire life, thereby creating a constitutive ER-LD MCS. Once LDs reach maturity, they are treated as separate entities from the ER due to their distinct lipid and protein compositions; however, the ER clearly influences both properties. Some pose that mature LDs are excised from the ER, while other propose that a lipidic bridge constitutively exists between ER and LDs to control NL content during distinct physiological states (Cottier and Schneiter, 2022; Jacquier et al., 2011). How lipids are distributed between the ER and LD is not well understood, but the field is slowly beginning to understand how proteins target to LDs, which is discussed below.

*Mechanisms of lipid droplet protein targeting*

At least routes exist for protein targeting to LDs: 1) cytoplasm to LD targeting or 2) ER to LD targeting. For proteins that target LDs from the cytoplasm, three mechanisms have been discovered. First, proteins can be anchored to LDs via a lipid moiety like palmitoylation or prenylation. Second, some proteins are targeted to LDs via protein-protein interactions, but do not possess LD-interacting motifs themselves. Lastly, cytosolic proteins can associate with LDs via amphipathic helices (AHs) (Kory et al., 2016). LDs are encased by a phospholipid

monolayer rather than a bilayer, which also possesses phospholipid packing defects that expose the hydrophobic core of LDs to hydrophilic environments (Bacle et al., 2017). Exposure of NLs to the cytosol is energetically unfavorable; therefore, amphipathic helices insert into the packing defects of the monolayer to mitigate NL exposure (Giménez-Andrés et al., 2018). AHs resemble molecular hairpins, with each side of the hairpin facing the cytosol and the hinge embedded into the core of the LD. The tops of the hairpin are typically composed of charged residues that can interact with the phospholipid head groups. Another characteristic feature of LD-targeting AHs is the presence of bulky hydrophobic residues (i.e. phenylalanine and tryptophan) that may interact with phospholipid acyl chains or recognize packing defects (Prévost et al., 2018). Unexpectedly, some AH hinges have large positively charged residues that are thought to interact with hydrated TAG at the interface between the phospholipid acyl chains and the NL core (Kim and Swanson, 2020). Because the model of AH binding to LDs has mostly been uncovered through understanding 'model' proteins, it is likely that much is to be discovered about mechanisms of cytosol to LD targeting.

Much less is known about targeting of ER proteins to LDs, even though this represents a large class of proteins. Generally, ER proteins can target LDs via a 'hydrophobic helix' or 'module' that may function similarly to the AHs described above (Olarte et al., 2020). Changes in the phospholipid bilayer of the ER, such as fluidity or TAG concentration, may promote the translocation of proteins from the ER to LDs. On the other hand, some ER to LD targeting proteins may recognize NL lenses during LD growth and biogenesis (Caillon et al., 2020). Nonetheless, LDs require a mechanism to exclude non-specific ER proteins from docking; however, the field's current model suggests that simple energetic favorability could perform this role. Due to the lack of aqueous interiors in LDs, non-specific targeting of ER proteins to the LD is considered energetically unfavorable. One further complicating factor about LD protein targeting are the compositional heterogeneities observed inside of living cells. Some LD proteins specifically enrich on sub-sets of LDs. Some have proposed that there are distinct populations of LDs within cells, which may be distinguished by their NL content (Eisenberg-Bord et al., 2018; Zhang et al., 2016). How cells create and regulate different lipid

compositions inside of LDs is not well understood, but may be essential for unraveling the mystery of LD formation and function.

*Lipid droplet compositional control*

For LDs to be efficient reservoirs of cellular energy, the NLs within need to be accessible for degradation. One pathway for NL degradation, lipolysis, employs TAG and SE lipases to cleave FFA moieties from the respective NLs. Once cleaved, FFAs can be targeted for β-oxidation to produce ATP. An alternative pathway for LD turnover is lipophagy. Lipophagy is a form of micro-autophagy that selectively degrades lipid droplets in the lysosome of mammalian cells or the vacuole of yeast (Schulze et al., 2017; Zechner et al., 2017). Once engulfed into the lysosome, acid lipases and proteases can degrade the lipids and proteins, respectively. While proteins can be degraded following lipophagy, LD proteins can also be selectively degraded by the proteasome. Some LD proteins are targeted to the proteasome directly from the LD surface, while others appear to translocate to the ER prior to degradation (Bersuker and Olzmann, 2017; Roberts and Olzmann, 2020). There have even been proteins suggested to require LD targeting for proteasomal degradation. It is not yet clear if specialized degradation machinery is required to remove proteins from the LD prior to degradation, but this is a model that is currently being explored.

The second means of controlling LD protein composition involves changing the lipid content of LDs. By genetically removing the enzymes required for TAG or SE synthesis, some groups have observed that TAG-only and SE-only LDs harbor distinct proteomes (Gao et al., 2017). Considering again the binding of AHs to LDs, some proteins may require hydrated TAG to bind LD, wherein they become unstable if not LD bound (Olarte et al., 2020). While not currently addressed in the field, phospholipid acyl chain saturation may also contribute to LD protein composition by modulating monolayer fluidity. Fluidity would likely affect most profoundly ER to LD targeting proteins by adding an additional barrier to diffusion from the lipid bridge connecting ER to LDs. One final LD organizational factor that may influence LD protein targeting is the phase of NLs in the LD core. A few studies have now proposed that the

SEs within the core of LDs can undergo a liquid to liquid-crystalline phase transition (Czabany et al., 2008; Mahamid et al., 2019). Along these lines, SEs in the core of LDL particles have also been proposed to exist in a liquid crystalline state called a smectic phase (Kroon, 1981). Smectic phase SEs are found abundantly in the fatty streaks of human aortas, which is correlated with heart disease (Engelman and Hillman, 1976). Furthermore, TAG assists in solubilizing SEs *in-vitro* (Kroon, 1981). Taken together, the requisite of TAG presence for LD protein targeting could be influenced by both the reduction of TAG or the phase of SEs. If smectic phase SEs are the closest NL to the phospholipid acyl chains, it may resemble the proteome of SE-only LDs. However, the connection between SE phase and LD proteomes has not been conducted to date.

**Hypothesis**

While much has been uncovered about ER-MCSs in the previous two decades, several knowledge gaps still exist in our mechanistic understanding of ER-MCSs. Revisited from the beginning of this section: 1) how does partitioning of clients at ER-MCSs alter their function, especially for 'non-canonical' ER-MCS clients? 2) what are the down-stream influences of client partitioning on cellular physiology? While these questions are broad, they can be focused to specifically address the role of ER-MCSs in spatially regulating metabolic processes. The yeast NVJ serves as an excellent model ER-MCS given that the tethers are well characterized, the NVJ is responsive to several cellular stresses, and a few 'non-canonical' clients have already been localized to the NVJ.

My hypothesis is that **the NVJ spatially concentrates lipid metabolic proteins to control either their degradation or their activity**. As with Pah1, the NVJ may control the activity of lipid metabolism enzymes for the sake of modulating key pathways during the response to cellular nutrient stress. By controlling enzyme activity, pathways may be differentially wired to bias the production of lipids that would promote survival in the face of starvation. Alone these lines, **I propose that partitioning of non-canonical clients at the NVJ will influence LD protein or lipid composition**. Though some lipid metabolic enzymes concentrate at the

NVJ, the down-stream destination for their products have not been mapped. LDs seem like a likely destination, given the existing connection between the NVJ and LD positioning.

In the pages below, I will describe my cumulative work on the NVJ. Using biochemistry, fluorescence microscopy, and yeast genetics, I characterized a novel NVJ client protein, Hmg1, whose catalytic activity is modulated by the NVJ during glucose starvation. Via spatial concentration of Hmg1 at the NVJ, it appears Hmg1 assembles into high molecular weight species, which increases its activity. Finally, the down-stream products of the Hmg1 pathway, SEs, are packaged into LDs during glucose starvation, which re-organizes the LD NL core. I found that SEs undergo liquid to liquid-crystalline phase transitions during glucose stress that are induced by TAG lipolysis and re-organize the LD proteome. Altogether, this work begins to answer a few of the critical questions surrounding ER-MCSs. The details of ER-MCSs as sub-organelle platforms that modulate metabolism are now coming into focus. To further develop this work, a mixture of biochemistry and structural biology would shine light on the compositional complexity of the NVJ and how several biochemical processes may function together in unexpected ways.

# CHAPTER TWO

## Glucose restriction drives spatial reorganization of mevalonate metabolism


### Abstract

Eukaryotes compartmentalize metabolic pathways into sub-cellular domains, but the role of inter-organelle contacts in organizing metabolic reactions remains poorly understood. Here, we show that in response to acute glucose restriction (AGR) yeast undergo metabolic remodeling of their mevalonate pathway that is spatially coordinated at nucleus-vacuole junctions (NVJs). The NVJ serves as a metabolic platform by selectively retaining HMG-CoA Reductases (HMGCRs), driving mevalonate pathway flux in an Upc2-dependent manner. Both spatial retention of HMGCRs and increased mevalonate pathway flux during AGR is dependent on NVJ tether Nvj1. Furthermore, we demonstrate that HMGCRs associate into high molecular weight assemblies during AGR in an Nvj1-dependent manner. Loss of Nvj1-mediated HMGCR partitioning can be bypassed by artificially multimerizing HMGCRs, indicating NVJ compartmentalization enhances mevalonate pathway flux by promoting the association of HMGCRs in high molecular weight assemblies. Loss of HMGCR compartmentalization perturbs yeast growth following glucose starvation, indicating it promotes adaptive metabolic remodeling. Collectively we propose a non-canonical mechanism regulating mevalonate metabolism via the spatial compartmentalization of rate-limiting HMGCR enzymes at an inter-organelle contact site.


### Introduction

The complexity of eukaryotic metabolism requires spatial organization, so membrane-bound and membraneless organelles compartmentalize enzymes into distinct sub-cellular regions. Enzyme partitioning into spatially defined domains is a cellular organizational principle observed in cytoplasmic assemblies (Chan et al., 2015), enzyme homo-polymers (Meredith

and Lane, 1978) and biomolecular condensates (Banani et al., 2017; Jin et al., 2017). Such enzymatic assemblies, or metabolons, enhance or fine-tune metabolic flux, locally sequester toxic intermediates, or limit product shunting to competing pathways. Enzyme partitioning has also been exploited in synthetic bioengineering to artificially force enzymes into close proximity to drive local reactions or metabolic channeling through enzymatic cascades (Dueber et al., 2009).

Inter-organelle contact sites also serve as platforms for enzymatic organization and lipid synthesis reactions. In particular, the endoplasmic reticulum (ER) partitions lipogenic processes like non-vesicular lipid transport and organelle biogenesis at inter-organelle junctions (Friedman et al., 2011; Hariri et al., 2018; Lev, 2012). In yeast and humans, mitochondrial-associated membranes with the ER (MAMs) harbor enhanced metabolic activity to support reactions such as the biosynthesis and transport of phosphatidylserine (Gaigg et al., 1995; Vance, 1990). More recent work has highlighted the role of ER-mitochondrial contacts defining distinct sub-domains within mitochondria that support the formation of multi-enzyme complexes that drive Coenzyme Q synthesis (Eisenberg-Bord et al., 2019; Subramanian et al., 2019). In yeast the nuclear envelope (continuous with the ER network) also makes extensive contact with the vacuole (equivalent to the lysosome), forming a nucleus-vacuole junction (NVJ). Formed through hetero-dimerization of nuclear envelope protein Nvj1 and vacuole-associated protein Vac8, the NVJ is a disc-shaped inter-organelle contact that acts as a multi-functional platform to organize lipid transport, fatty acid synthesis, and lipid droplet (LD) biogenesis, particularly during metabolic stress (Hariri et al., 2018; Kvam et al., 2005; Murley et al., 2015). Despite these insights, few studies mechanistically dissect how metabolic cues regulate enzyme recruitment and compartmentalization at inter-organelle contacts. Furthermore, how inter-organelle junctions enable enzyme spatial organization to fine-tune or enhance metabolic flux remains poorly described. Such inter-organelle crosstalk is particularly pertinent to understanding adaptive responses to stresses such as glucose starvation, which is characterized by drastic decreases in cellular ATP as well as changes in cytoplasmic pH and fluidity that alter macromolecular trafficking (Joyner et al., 2016; Munder et al., 2016).

Here, we use budding yeast as a genetically enabling model system to dissect the role of ER-lysosome contacts (e.g. the NVJ) as organizational platforms in mevalonate metabolism. We find that in response to acute glucose restriction (AGR), yeast actively partition and selectively retain HMG-CoA Reductase (HMGCR) enzymes at the NVJ in a Nvj1 and Upc2-dependent manner. This enzyme sub-compartmentalization enhances mevalonate pathway flux and promotes sterol-ester biosynthesis during AGR-induced metabolic remodeling. Failure to compartmentalize HMGCRs affects resumption of yeast growth following re-introduction to glucose containing media, but can be rescued by addition of exogenous mevalonate. We also find that NVJ compartmentalization of HMGCRs is accompanied by an Nvj1-dependent association of HMGCRs into high molecular weight complexes. Interestingly, both the growth resumption delay and mevalonate production phenotypes observed in Nvj1 knock-out cells can be rescued by the artificial multimerization of HMGCRs via a tetramerizing tag.

## Results

### Yeast Hmg-CoA Reductases (HMGCRs) inducibly partition at the nucleus-vacuole junction (NVJ) in response to acute glucose restriction (AGR)

Given that ER-mediated contact sites in *Saccharomyces cerevisiae* act as lipogenic domains, we visually screened GFP-tagged neutral lipid metabolism enzymes for signs of compartmentalization at ER inter-organelle contact sites in yeast exposed to AGR. Note that AGR is operationally defined here as culturing yeast in synthetic complete (SC) media containing 2% glucose, then briefly centrifuging them and placing them into SC media containing 0.001% glucose. Screening revealed that endogenously GFP-tagged HMG-CoA Reductases (HMGCR) Hmg1 and Hmg2, which localize throughout ER network and particularly on the nuclear envelope (NE), enriched at the regions where the nuclear surface was in contact with the vacuole following AGR (**Figure 2.1A**). This nucleus-vacuole interface was confirmed to be the NVJ as Hmg1-GFP co-localized with NVJ tether Nvj1-mRuby3

following AGR treatment for 4hrs (**Figure 2.1B**). As Hmg1 and Hmg2 are functionally redundant in mevalonate synthesis, a central metabolite that supplies diverse cellular pathways including sterol biogenesis, we chose to dissect the mechanisms underlying Hmg1 NVJ partitioning. To investigate whether the NVJ was required for Hmg1 partitioning, we imaged Hmg1-GFP in the absence of NVJ tethers Nvj1 and Vac8 (Henne et al., 2015), and found they were required for Hmg1-GFP partitioning during AGR (**Figure 2.1C**). Furthermore, time-lapse imaging revealed that Hmg1-GFP NVJ partitioning peaked after ~4hrs of introducing yeast to AGR (**Figure 2.1D-F**). During this period, Hmg1-GFP was ~15-times enriched at the NVJ relative to other NE regions. Collectively this suggests that AGR induces the time-dependent compartmentalization of Hmg1/2 at the NVJ in a Nvj1 and Vac8 dependent manner.

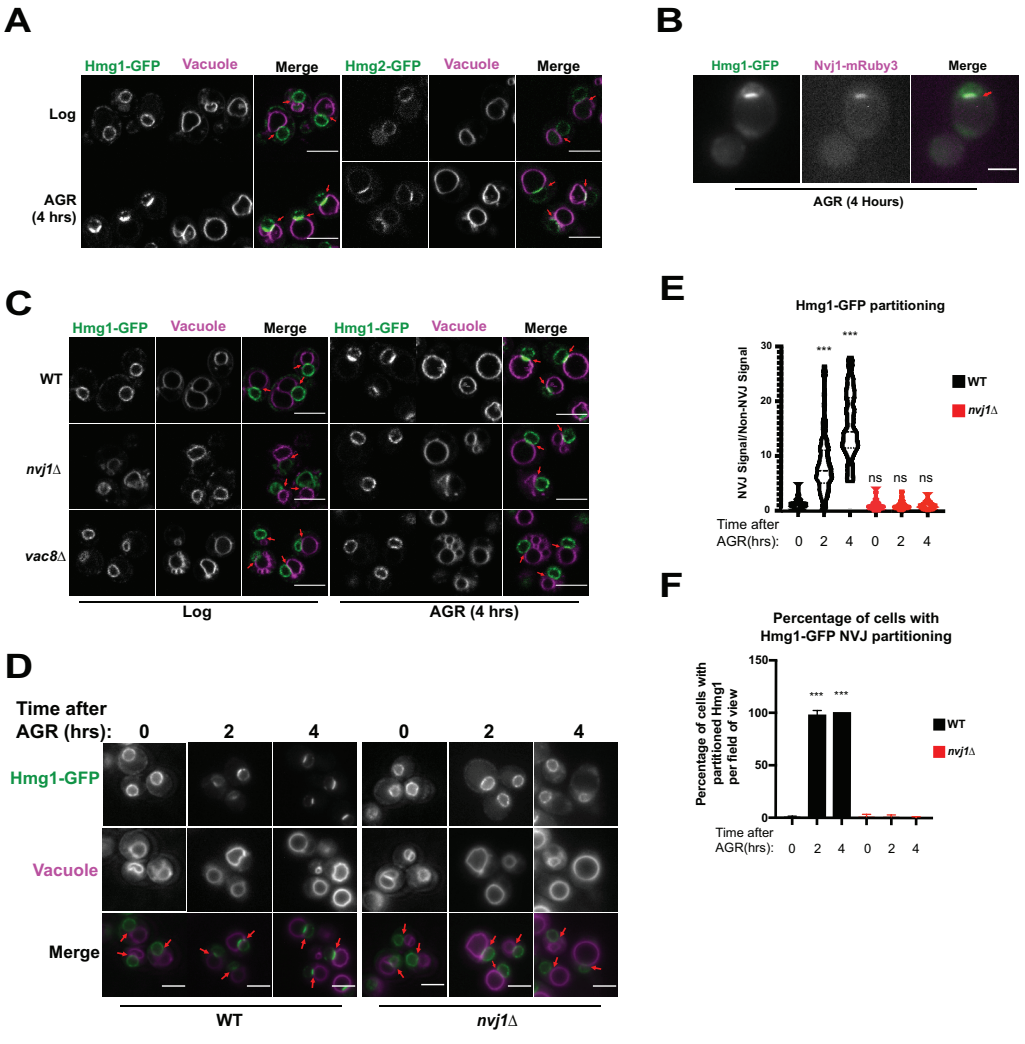

**Figure 2.1. The HMG-CoA Reductases, Hmg1 and Hmg2, enrich at the NVJ in an Nvj1-dependent manner during AGR**

**A)** Confocal microscopy images of yeast expressing endogenously tagged Hmg1-GFP or Hmg2-GFP (green) grown in SC media with 2% glucose to an OD of 0.5 (Log), or in 0.001% glucose for 4hrs (AGR). Vacuoles (magenta) were visualized by staining with FM4-64. Red arrows represent the relative location of the Nucleus-Vacuole Junction (NVJ), or where the nuclear envelope is closely apposed to the vacuole in *nvj1*Δ cells. Scale bars=5μm.

**B)** Epifluorescence microscopy images showing the overlap of Hmg1-GFP with Nvj1-mRuby3 after cells were exposed to four hours of AGR. Red arrows represent the location of the NVJ. Scale bars=5μm

**C)** Confocal microscopy images of yeast expressing endogenously tagged Hmg1-GFP (green) in wild type (WT), *nvj1*Δ, or *vac8*Δ yeast. Red arrows represent the location of NVJ. **D)** Epifluorescence microscopy images of WT or *nvj1*Δ yeast expressing endogenously tagged Hmg1-GFP growing in 2% glucose to an OD of 0.5 (Log) or in 0.001% glucose for 2 or 4hrs (AGR).

**E)** Quantification of Hmg1 partitioning measured by line scan across the nuclear envelope (NE) and plotted as the ratio of Hmg1-GFP intensity at the NVJ relative to Hmg1-GFP intensity opposite the NVJ. Scale bars represent 5μm. (Brown-Forsyth and Welch ANOVA. N≥51 cells. ***p-value<0.001).

**F)** Quantification of percentage of cells displaying Hmg1 NVJ partitioning per field of view. Any cell with partitioning >2.0 was considered as displaying Hmg1 NVJ partitioning. (Brown-Forsyth and Welch ANOVA. N≥51 cells. ***p-value<0.001)

## NVJ compartmentalization of HMGCRs is independent of other mevalonate pathway enzymes and lipid trafficking proteins Osh1 and Ltc1

Inter-organelle contacts are implicated as domains coordinating the recruitment of supra-molecular enzyme complexes that constitute metabolic pathways. The HMGCRs are the rate-limiting enzymes of the mevalonate pathway that generates ergosterol, the cholesterol analog of yeast. To dissect whether other proteins along the mevalonate pathway also partition at the NVJ during AGR, we imaged 20 endogenously mNeonGreen (mNG)-tagged proteins involved in ergosterol biosynthesis under ambient and AGR stress, but surprisingly none detectably enriched at the NVJ (**Figure 2.2A**). As the NVJ has also been proposed to function in sterol transport between the vacuole and ER network, we also examined whether loss of the NVJ-resident proteins Osh1 and Lam6/Ltc1, implicated in the inter-organelle trafficking of lipids and/or sterols, would impact Hmg1-GFP NVJ recruitment (Kvam, 2004; Murley et al., 2015). Hmg1-GFP efficiently partitioned at the NVJ following AGR in both *osh1*Δ and *lam6/ltc1*Δ yeast (**Figure 2.2B**). Collectively, this suggests that detectable Hmg1/2 NVJ enrichment is unique among enzymes involved in ergosterol metabolism, and is therefore unlikely to constitute a “classical” multi-enzyme metabolon.

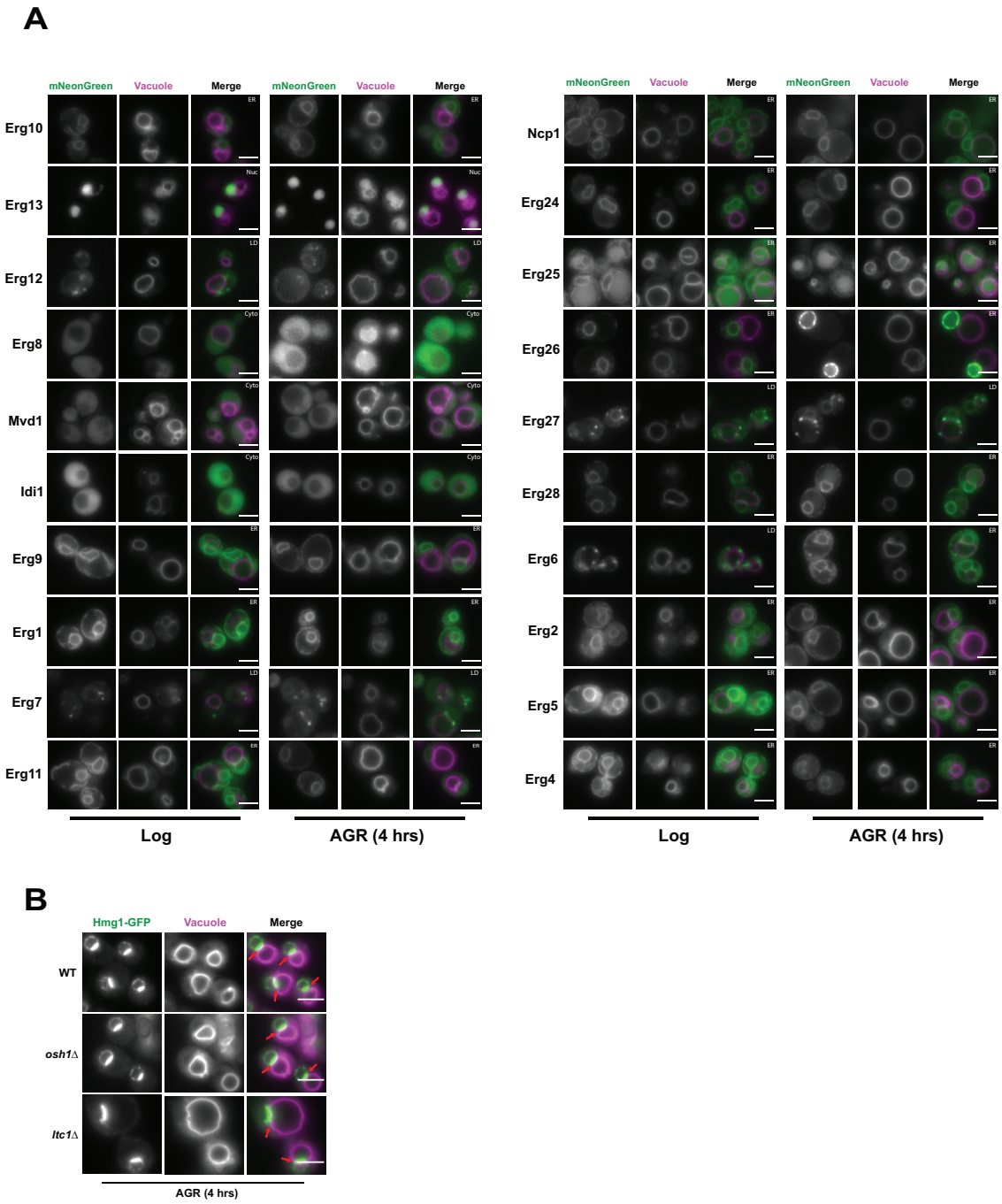


**Figure 2.2. Hmg1 NVJ partitioning is specific amongst ergosterol biosynthesis proteins and independent of NVJ-associated sterol transport proteins**

**A)** Epifluorescence microscopy images of twenty ergosterol biosynthesis proteins endogenously tagged with mNeonGreen (mNg) imaged in log phase and after 4hrs of AGR. Cells were co-stained with FM4-64 (magenta) to visualize vacuoles. Cellular compartments occupied by each protein are designated in white text in the top right corner of each image. Scale bars=5µm.

**B)** Epifluorescence microscopy images of cells endogenously tagged with Hmg1-GFP in wild type (WT), *osh1*Δ, or *ltc1*Δ cells exposed to 4hrs of AGR. Scale bars=5µm.

**Hmg1-GFP is selectively retained at the NVJ in a Nvj1-dependent manner**

Next, we investigated the mechanistic basis for NVJ compartmentalization of Hmg1-GFP. We began by interrogating whether the NVJ-partitioned and non-partitioned Hmg1-GFP pools were physically segregated along the NE. Using fluorescence recovery after photobleaching (FRAP), we determined that the non-partitioned Hmg1-GFP pool can enter the NVJ (**Figure 2.3A,B**); therefore, there is likely no diffusion barrier at the NVJ allowing selective entry of only specific pools of Hmg1-GFP protein. Next we interrogated whether Hmg1-GFP was selectively retained after entry into the NVJ region. Fluorescence loss in photobleaching (FLIP) revealed the average lifetime of NVJ-partitioned Hmg1-GFP was >100sec, compared to only ~25sec for Hmg1-GFP along the rest of the NE (**Figure 2.3C,D**). Given that most of the Hmg1-GFP signal within the NVJ-partitioned population was not photobleached to completion, calculated halftimes may underestimate the actual halftime. Collectively, this indicates that upon AGR, Hmg1-GFP is recruited and selectively retained at the NVJ. Surprisingly, the halftime of Hmg1-GFP was also significantly increased during AGR in *nvj1*Δ cells. This may be connected to a change in cytoplasmic viscosity which has been discussed previously (Joyner et al., 2016); however further analysis is required to determine if this reduced mobility is specific to Hmg1-GFP or a general consequence of AGR.

Next, we dissected which regions of Hmg1 and Nvj1 were required for Hmg1-GFP NVJ retention. We generated truncated versions of GFP-tagged Hmg1 containing only its integral transmembrane (TM) region and lacking its cytoplasm-exposed catalytic domain. This $Hmg1_{1-525}$-GFP truncation was sufficient to localize to the NVJ during AGR, indicating the integral membrane region of Hmg1 was sufficient for NVJ recruitment (**Figure 2.3E,F**). To dissect the Nvj1 regions required for Hmg1-GFP recruitment, we expressed mNg-tagged Nvj1 fragments in yeast co-expressing Hmg1-mRuby3 (**Figure 2.3G**). A Nvj1-mNG chimera lacking its cytoplasm-exposed region and containing a vacuole-binding PX domain in place of its Vac8-binding domain (Nvj1-PX) was sufficient to tether between the nucleus and vacuole, and was sufficient to partition Hmg1-mRuby3 at the NVJ during AGR, indicating the Nvj1 cytoplasmic domain is not required for Hmg1 recruitment (**Supplementary Figure 2.3A**). Similarly, a

Nvj1-mNG chimera with its TM region replaced with the TM of Nvj2 ($Nvj1_{Nvj2TM}$) also partitioned Hmg1-mRuby3 at the NVJ, indicating the TM and cytoplasmic regions are not required for Hmg1-mRuby3 recruitment (**Supplementary Figure 2.3A**). However, expression of a full length Nvj1-mNG lacking residues 15-30 ($Nvj1_{\Delta 15\text{-}30}$) of its luminal region formed an NVJ contact but failed to recruit Hmg1-mRuby3. Re-addition of six residues to this construct ($Nvj1_{\Delta 15\text{-}24}$) rescued Hmg1-mRuby3 recruitment. Furthermore, mutation of arginine and lysine residues at positions 28/29 to alanines ($Nvj1_{RK\rightarrow AA}$) also ablated AGR-induced recruitment of Hmg1 to the NVJ, suggesting residues 25-30 of the Nvj1 luminal domain play a key role in Hmg1-mRuby3 NVJ partitioning (**Figure 2.3G-I**). Collectively, these data indicate that the ER embedded region of Hmg1 is recruited to the NVJ in a manner requiring the ER-luminal Nvj1 region, and that Hmg1 partitioning is not dependent on the Hmg1 cytoplasmic catalytic domain nor the Nvj1 cytoplasmic/vacuole binding region.

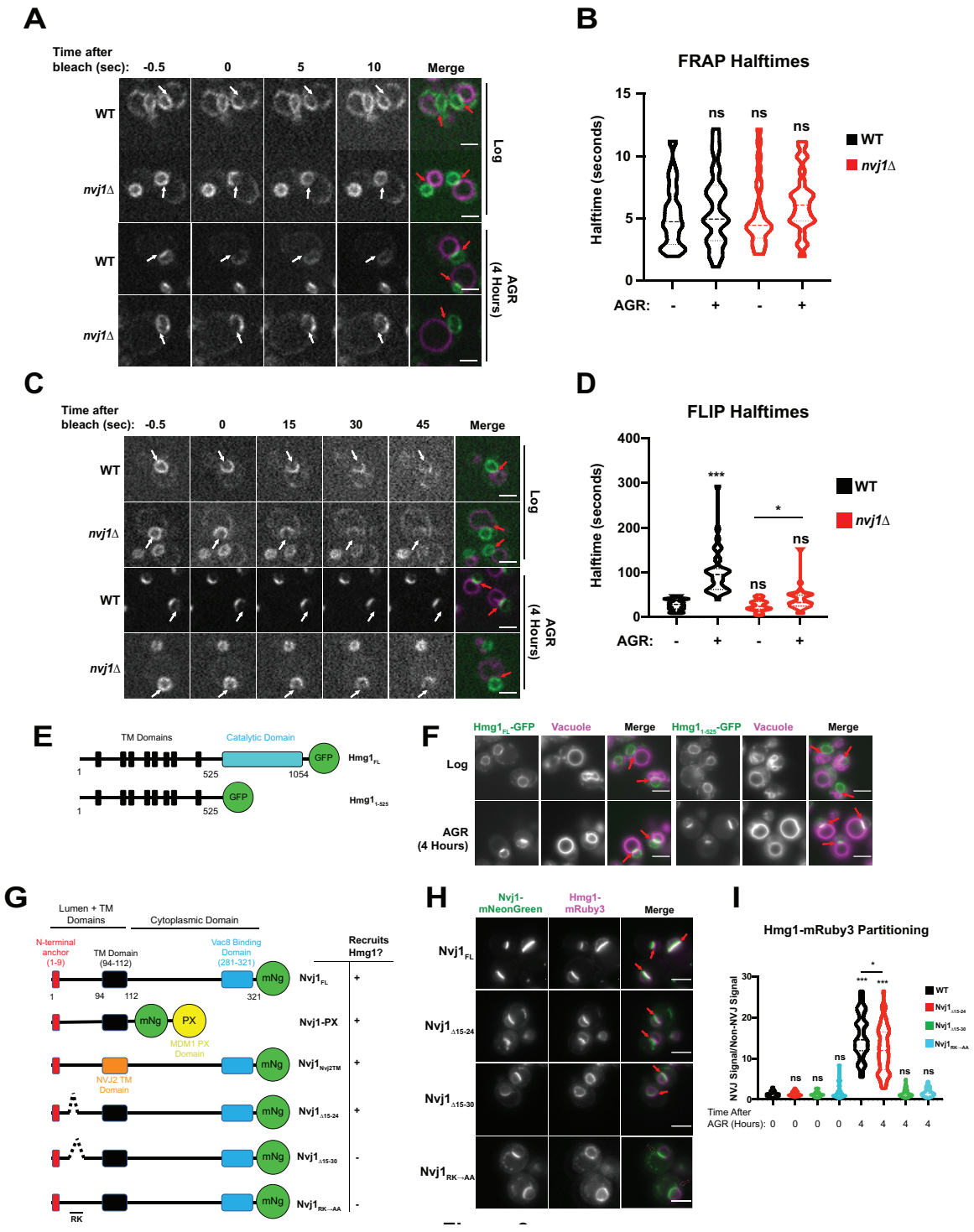


**Figure 2.3. Hmg1 is selectively retained at the NVJ and requires a luminal domain of Nvj1**

**A)** Spinning disk confocal microscopy images from FRAP movies of yeast expressing endogenously tagged Hmg1-GFP and stained with FM4-64 (magenta). Portions of the NE corresponding to the NVJ were photobleached (white arrows) and recovery was monitored in both WT and *nvj1*Δ cells grown to log phase or after 4hrs of AGR. Red arrows represent the location of the NVJ.

**B)** Quantification of Hmg1-GFP FRAP halftimes after photobleaching. (Brown-Forsyth and Welch ANOVA. N≥26 cells)
**C)** Spinning disk confocal microscopy images taken from FLIP movies. Conditions and strains were the same as in (A). One region of the NE that lies opposite the NVJ was photobleached every 5 seconds (white arrows) and Hmg1-GFP signal at the NVJ was monitored for loss of fluorescence. Time above the images indicates seconds after the first bleach pulse. Red arrows represent the location of the NVJ
**D)** Quantification of FLIP halftimes. (Brown-Forsyth and Welch ANOVA. N≥29 cells. *p-value>0.05 ***p-value<0.001).
**E)** Cartoon of Hmg1-GFP constructs endogenously expressed in yeast with both the cytosolic catalytic domain (blue) and TM/luminal domains (black) ($Hmg1_{FL}$) or the TM/luminal domains alone ($Hmg1_{1\text{-}525}$).
**F)** Epifluorescence microscopy images of yeast expressing endogenously tagged $Hmg1_{FL}$-GFP or $Hmg1_{1\text{-}525}$-GFP.
**G)** Cartoon of Nvj1-mNeonGreen constructs expressed in *nvj1*Δ cells. $Nvj1_{FL}$-mNg contains all domains of Nvj1 including the N-terminal luminal anchor (red), the TM domain (black), and the Vac8-binding domain (VBD) (blue). Chimeric constructs either replaced the VBD with a vacuole-binding PX domain ($Nvj1_{PX}$) or replaced the endogenous TM domain with the TM domain of Nvj2 ($Nvj1_{NVJ2TM}$). Images of these constructs can be found in Supplemental figure 1A. Truncations of Nvj1 removed either residues 15-24 ($Nvj1_{15\text{-}24\Delta}$), 15-30 ($Nvj1_{15\text{-}30\Delta}$), or mutated residues 28 and 29 to alanine ($Nvj1_{RK\rightarrow AA}$).
**H)** Epifluorescence microscopy images of yeast expressing truncation constructs depicted in (G). Cells were co-expressing endogenously tagged Hmg1-mRuby3 (magenta). Scale bars represent 5µm.
**I)** Quantification of Hmg1 partitioning at the NVJ for yeast expressing truncations of Nvj1-mNg and Hmg1-mRuby3. (Brown-Forsyth and Welch ANOVA. N≥61 cells. *p-value<0.05 ***p-value<0.001)

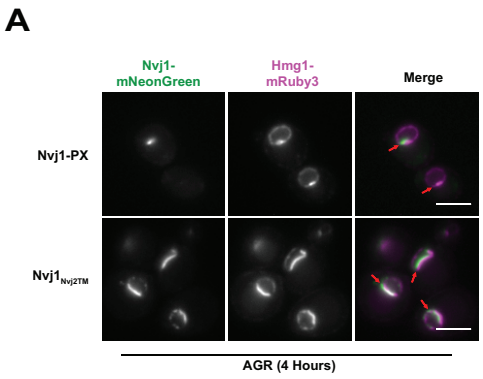


**Supplemental Figure 2.3. Hmg1 NVJ partitioning is not dependent on the cytoplasmic or transmembrane regions of Nvj1**
**A)** Epifluorescence microscopy images of cells expressing ADH promoter-driven Nvj1-mNeonGreen (Nvj1-mNg) chimeric constructs (green) either substituting the endogenous transmembrane region with that of Nvj2 ($Nvj1_{Nvj2TM}$) or substituting the endogenous Vac8 binding domain with a vacuole binding PX domain (Nvj1-PX). Chimera strains co-expressed endogenously tagged Hmg1-mRuby3 (magenta) and lacked endogenous Nvj1. Images were taken after exposing cells to four hours of AGR. Scale bars represent 5µm.

## NVJ partitioning of Hmg1 is Upc2 dependent and correlates with sterol-ester biosynthesis

The NVJ was previously identified as a site for starvation-induced microautophagy of the nucleus (Roberts et al., 2003), where NVJ-associated proteins accumulate and are subsequently

engulfed by the vacuole. HMGCRs are also known to undergo proteasomal degradation during specific metabolic cues. To determine if NVJ partitioning of Hmg1-GFP regulated Hmg1 protein abundance or turnover, we performed immunoblot analysis of Hmg1-GFP in log-phase and 4hrs AGR-treated cells. AGR increased steady-state Hmg1-GFP protein levels, indicating glucose restriction promoted Hmg1 protein accumulation (**Figure 2.4A**). Interestingly, *nvj1*Δ yeast displayed a more marked increase in Hmg1-GFP protein compared to wildtype. To determine the influence of proteasomal degradation on Hmg1 protein levels during AGR, we treated cells with proteasome inhibitor MG132 and observed only a moderate increase in steady state Hmg1-GFP protein levels (**Figure 2.4B**). In contrast, treatment with the translation inhibitor cycloheximide during AGR returned Hmg1-GFP protein abundance to levels comparable with log-phase cells. Collectively, this analysis suggests that proteasomal degradation does not contribute significantly to controlling Hmg1-GFP protein abundance during AGR, and the increase is likely due to *de novo* protein synthesis during glucose restriction.

To further explore the metabolic cues governing AGR-induced Hmg1 synthesis and spatial partitioning, we monitored Hmg1-GFP localization in yeast lacking the major glucose-sensing kinase Snf1, the yeast AMPK homolog that regulates metabolic remodeling during changes in glucose availability (Hedbacker and Carlson, 2008). Surprisingly, *snf1*Δ yeast maintained AGR-induced Hmg1-GFP partitioning at the NVJ, indicating Hmg1-GFP recruitment to the NVJ was not dependent on Snf1/AMPK signaling (**Figure 2.4C**). We next examined whether Hmg1-GFP NVJ partitioning required the ergosterol-sensing transcription factor Upc2 that controls yeast sterol synthesis in a manner similar to mammalian SREBP signaling (Yang et al., 2015). Indeed *upc2*Δ yeast failed to partition Hmg1-GFP at the NVJ during AGR, and this was specific to *upc2*Δ, as Hmg1-GFP maintained NVJ partitioning in *ecm22*Δ yeast, a Upc2 paralog (**Figure 2.4D-F**). To determine whether loss of Upc2 was influencing Hmg1 partitioning through Nvj1, we imaged Nvj1-mNg in wild type or *upc2*Δ cells. We found that neither Nvj1 localization, Nvj1 expression, nor NVJ size was affected in the absence of Upc2 (**Supplementary Figure 2.4A-C**); therefore, loss of Hmg1 NVJ partitioning in *upc2*Δ cells occurs independently of Nvj1. Additionally, we monitored Hmg1-GFP expression in *upc2*Δ

cells and found no significant changes when compared to Hmg1-GFP wild type cells (**Supplementary Figure 2.4D**). These data suggest that there are yet unidentified factors that are needed for Hmg1 NVJ partitioning that require the presence of Upc2, as well as the luminal region of Nvj1, and that partitioning might be uncoupled from Hmg1 protein expression.

Control of Hmg1 partitioning via Upc2 implied that Hmg1-GFP NVJ partitioning correlated with alterations in cellular ergosterol levels. In line with this, Hmg1-GFP NVJ partitioning was also induced by treatment with the squalene epoxidase inhibitor terbinafine, which blocks *de novo* ergosterol biogenesis (**Figure 2.4G-I**). To directly examine cellular sterols, we conducted thin layer chromatography (TLC). Indeed, following 4hrs of AGR when Hmg1-GFP is NVJ partitioned, yeast exhibited ~30% more steady-state levels of sterol-esters (SE), while free ergosterol levels were unchanged (**Figure 2.5A,B**). Co-treatment with the HMGCR inhibitor lovastatin during AGR suppressed this SE elevation, indicating the elevated SE pool originated from *de novo* SE synthesis rather than esterification of pre-existing ergosterol. Altogether, this suggests that AGR induces an Upc2-dependent compartmentalization of Hmg1 at the NVJ, which correlates with elevated *de novo* SE synthesis.

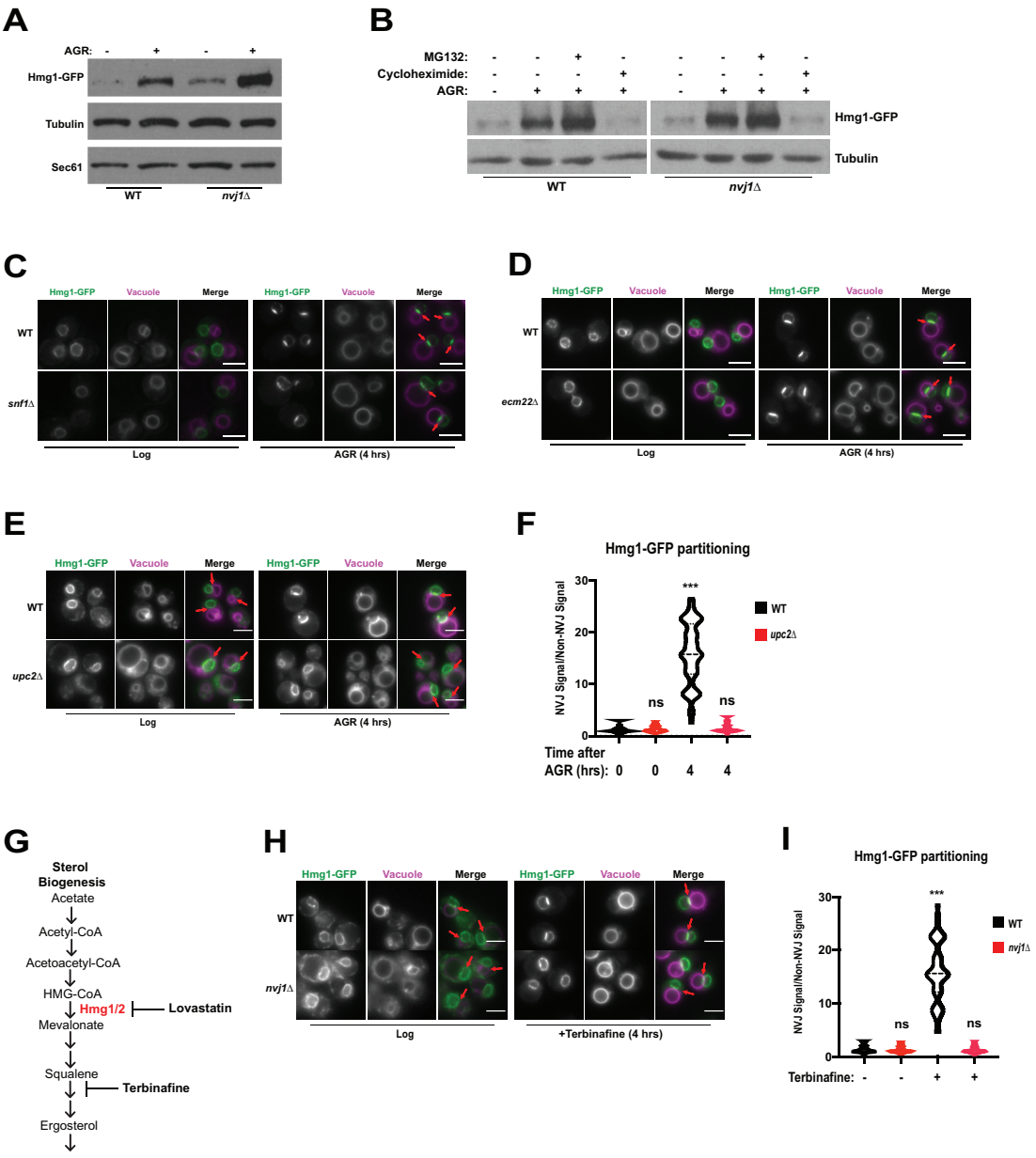


**Figure 2.4. Hmg1 protein accumulates in *nvj1*Δ yeast via enhanced synthesis, which coincides with Upc2-dependent Hmg1 clustering at the NVJ**

**A)** Immunoblot of cells expressing endogenously-tagged Hmg1-GFP grown to log-phase or treated with AGR for 4hrs. Tubulin and Sec61 antibodies were used as loading controls.

**B)** Immunoblot of Hmg1-GFP expressing cells grown to log-phase or treated with AGR for four hours. AGR-treated cells were also co-treated with either 100µg/mL cycloheximide or 25µM MG132. Tubulin was used as a loading control.

**C)** Epifluorescence microscopy images of cells expressing endogenously tagged Hmg1-GFP in either a wild type (WT) or Snf1 knock-out (*snf1*Δ) background.

**D)** Epifluorescence microscopy images of cells expressing endogenously tagged Hmg1-GFP in either a wild type (WT) or *ecm22*Δ background. Scale bars=5µm.

**E)** Epifluorescence microscopy images of endogenously tagged Hmg1-GFP (green) with FM4-64 stained vacuoles (magenta) grown to log phase or after 4hrs of AGR in wild type (WT) and *upc2*Δ yeast. Scale bars=5µm. Red arrows indicate relative position of the NVJ.
**F)** Quantification of Hmg1-GFP partitioning at NVJ from images represented in (E). (Brown-Forsyth and Welch ANOVA. N≥49 cells. ***p-value<0.001).
**G)** Schematic representing abbreviated ergosterol biogenesis pathway.
**H)** Epifluorescence microscopy images of wild type and *nvj1*Δ cells expressing endogenously tagged Hmg1-GFP treated with 10µg/mL of terbinafine for four hours. Scale bars represent 5µm.
**I)** Quantification of Hmg1-GFP partitioning at the NVJ from images shown in (H). (Brown-Forsyth and Welch ANOVA. N≥51 cells. ***p-value<0.001).

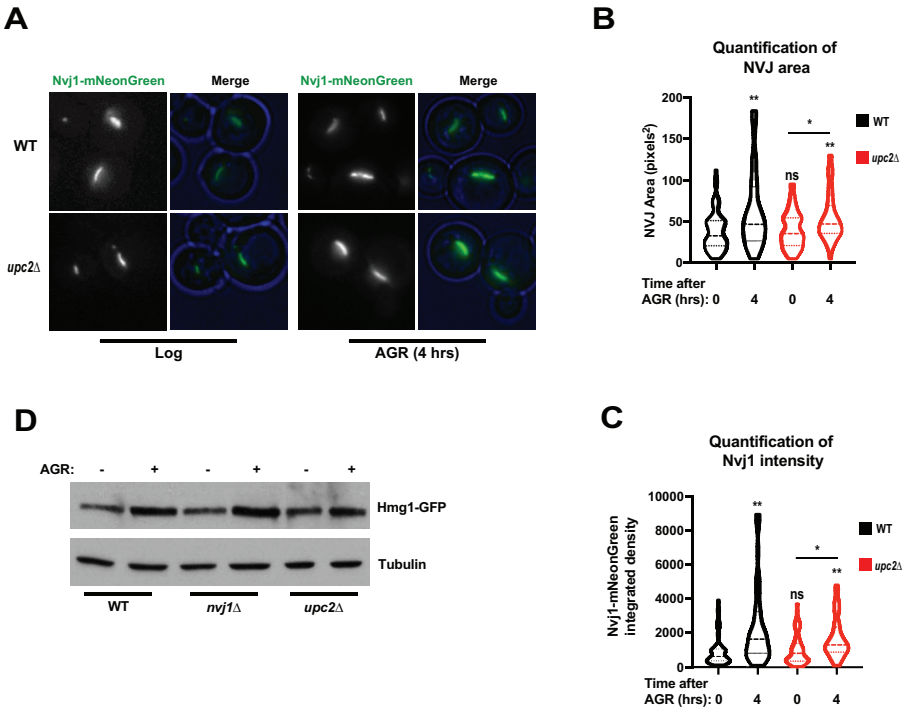


**Supplementary Figure 2.4. Loss of Hmg1 partitioning in *upc2*Δ cells does not function through Nvj1 or Hmg1 expression**
**A)** Epifluorescence images of yeast expressing Nvj1-mNeonGreen in either a WT or *upc2*Δ background. Blue outline was generated in Fiji by converting brightfield images to blue images and using 'adjust color balance' function.
**B)** Quantification of NVJ area, as measured by the length of Nvj1-mNeonGreen signal in each cell. (Brown-Forsyth and Welch ANOVA. N≥68. *p-value<0.05 **p-value<0.01).
**C)** Quantification of Nvj1-mNeonGreen signal intensity in either WT or *upc2*Δ cells. (Brown-Forsyth and Welch ANOVA. N≥68. *p-value<0.05 **p-value<0.01).
**D)** Immunoblot analysis of cells expressing endogenously tagged Hmg1-GFP in either WT, *nvj1*Δ, or *upc2*Δ backgrounds grown to either log phase or treated with four hours of AGR. Tubulin was used as a loading control.

## NVJ partitioning of HMGCR enhances mevalonate pathway flux

Given that *nvj1*Δ yeast accumulate more Hmg1-GFP protein than wildtype cells (**Figure 2.4A**), we were surprised to find that *nvj1*Δ yeast produce similar steady-state levels of SEs following AGR. This implied that HMGCR enzymes in *nvj1*Δ yeast could be catalytically less efficient. If true, we would expect: 1) accumulation of the HMGCR substrate HMG-CoA, and 2) a decrease in downstream mevalonate pathway products such as squalene, ergosterol, and SEs. To interrogate whether Hmg1 spatial compartmentalization influenced Hmg1 enzymatic activity and/or mevalonate pathway flux, we used $^{14}$C-acetate pulse-radiolabeling to monitor these mevalonate pathway components. Indeed, *nvj1*Δ yeast exhibited significantly elevated $^{14}$C-labeled HMG-CoA after a 15-minute radio-pulse, and contained significantly less $^{14}$C-labeled squalene, ergosterol, and SE (**Figure 2.5C-F**, **Supplementary Figure 2.5A**). However, $^{14}$C-diacylglycerol (DAG) was not significantly impacted, suggesting these alterations were specific to mevalonate pathway flux and not due to a non-specific dilution of the $^{14}$C-acetate radiolabel in *nvj1*Δ cells (**Figure 2.5G**).

To investigate whether these changes in mevalonate metabolism affected yeast fitness or growth, we monitored yeast growth after a 10hr period of AGR stress, followed by re-introduction to SC-media containing 2% glucose (SC+glucose). Indeed, *nvj1*Δ yeast displayed slower growth in culture following an AGR to SC+glucose transition compared to WT (**Figure 2.5H**). Notably, this was rescued by addition of exogenous mevalonate, suggesting the growth defect was attributed to defects in the mevalonate pathway (**Figure 2.5H**). To dissect the nature of this delayed cell growth, we conducted single-cell time-lapse imaging of yeast exposed to 10hrs of SC media lacking glucose (which induces cell cycle arrest and a halt to cell budding), followed by a glucose replenishment phase when yeast were again re-supplied with SC+glucose media, which promoted budding resumption. Quantifying the time required for growth resumption following this SC to SC+glucose transition, as measured by the appearance of the first daughter bud, showed that *nvj1*Δ cells had a significant delay in growth resumption (**Figure 2.5I**). In line with this, doubling times of cells were not affected by either loss of Nvj1 or addition of mevalonate following growth resumption (**Supplementary Figure 2.5B**). Together, these findings indicate that *nvj1*Δ yeast unable to spatially compartmentalize Hmg1

manifest alterations in mevalonate pathway flux, and that *nvj1*Δ yeast manifest growth defects following AGR that can be rescued by exogenous mevalonate addition.

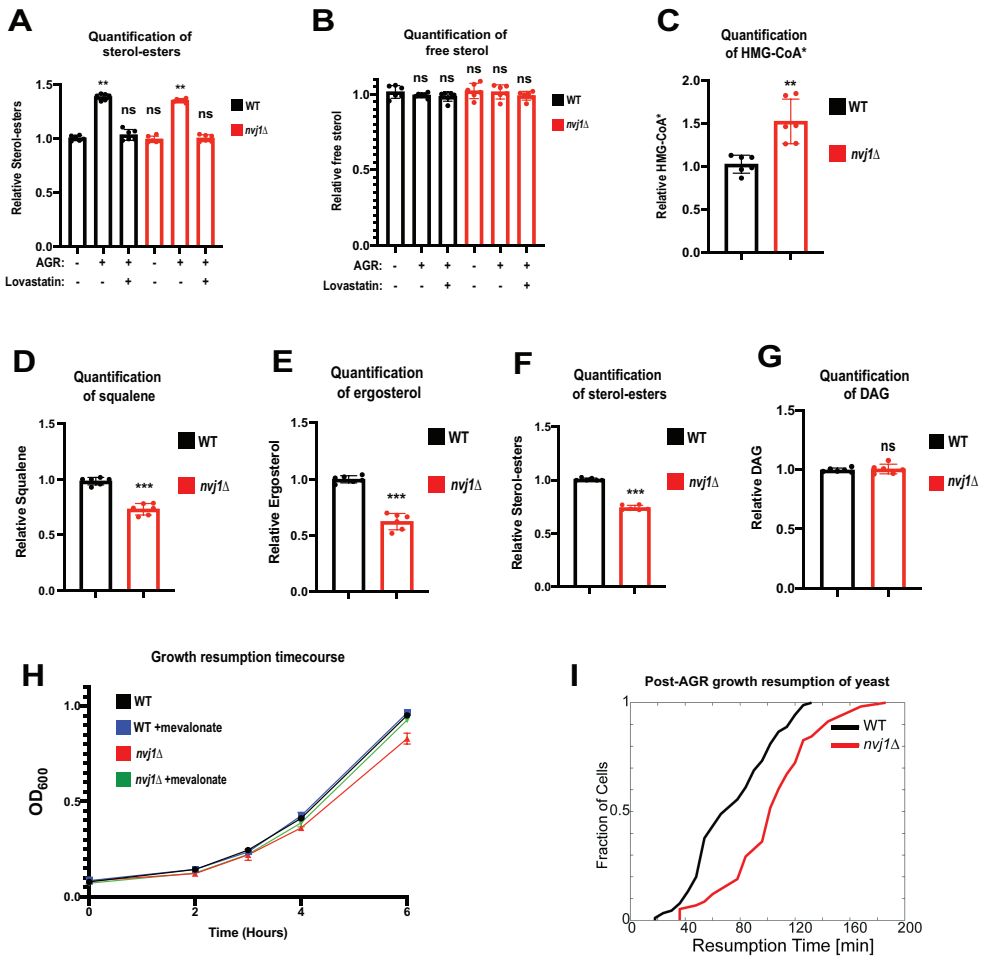


**Figure 2.5. Hmg1 NVJ partitioning coincides with *de novo* sterol-ester production and increased Hmg1 catalytic efficiency**

**A)** Quantification of SEs in wild type and *nvj1*Δ cells collected at log phase, after 4hrs of AGR, or after a 4hr co-treatment of AGR in the presence of 20μg/mL lovastatin. Neutral lipids were extracted, separated by TLC, and visualized using Cu(II) Sulfate spray and charring. Quantification performed by densitometry. (Brown-Forsyth and Welch ANOVA. N=6. **p-value<0.01)

**B)** Quantification of free sterols using the same strains and methodology as in (A). (Brown-Forsyth and Welch ANOVA. N=6. ***p-value<0.001).

**C)** Scintillation counting quantification of radiolabeled HMG-CoA* produced after a 15 minute pulse with $^{14}$C-acetate in intact WT or *nvj1*Δ cells grown for 4hrs in AGR. After quenching the radio-labeling reaction, soluble metabolites were isolated and endogenous HMG-CoA was converted into mevalonate using an *in vitro* HMGCR reaction. Mevalonate was subsequently separated and isolated by TLC, visualized by autoradiography, and quantified by scintillation counting. (Brown-Forsyth and Welch ANOVA. N=6. **p-value<0.01).

**D-G)** Quantifications of radiolabeled DAG and mevalonate-derived lipids. Radio-labeling was performed as described in (C). Lipids were extracted and separated by TLC and visualized by autoradiography. Squalene and SE bands were

quantified by scintillation counting. Ergosterol and DAG bands were quantified by densitometry. (Brown-Forsyth and Welch ANOVA. N=6. ***p-value<0.001).

**H)** Growth curves of WT and *nvj1*Δ cells. Cells were treated with AGR for 10 hrs in the absence or presence of 10μg/mL mevalonate, and subsequently diluted to $OD_{600}$=0.1 in SC media containing 2% glucose lacking mevalonate. $OD_{600}$ measurements were taken every hour following dilution in fresh glucose-containing media. (I) Resumption probability graph depicting probability of cells producing a daughter bud as a function of time following an SC to SC+glucose transition (N≥85 cells).

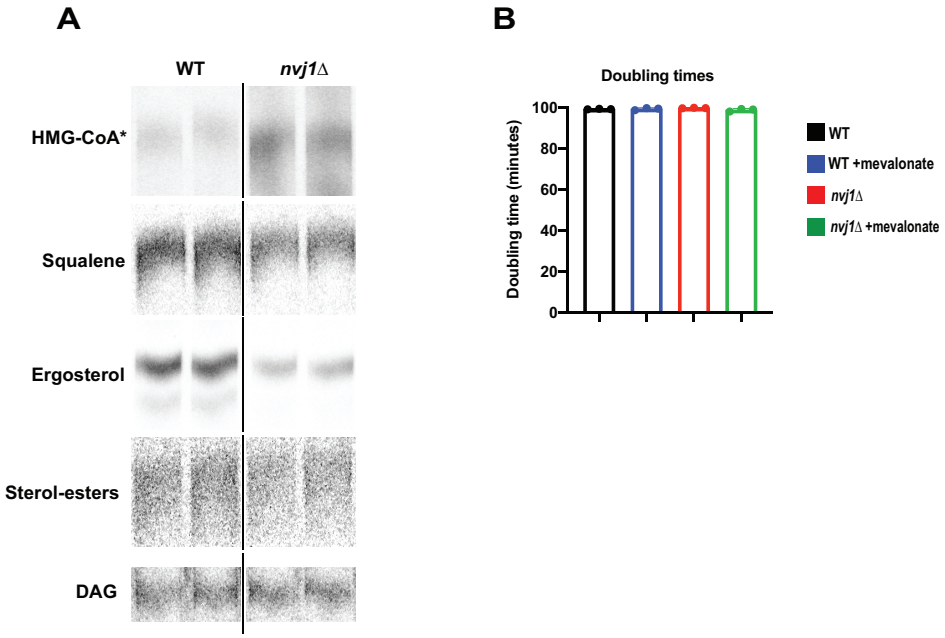


**Supplementary Figure 2.5. Cells lacking endogenous Nvj1 accumulate Hmg1 substrates and have decreased mevalonate-derived pathway products**

(A) Autoradiograms taken of TLC plates to visualize HMG-CoA* (visualized as mevalonate, see Fig 3 legend or supplemental methods) or squalene, ergosterol, SE, and DAG in wild type (WT) or *nvj1*Δ cells. Squalene, ergosterol, SE, and DAG were visualized on the same plate. DAG was used as a control band for neutral lipid species. Brightness/contrast was adjusted linearly in ImageJ to visualize bands. (B) Quantification of growth resumption in WT and *nvj1*Δ cells after ten hours in AGR. Resumption of growth was scored using single-cell time lapse imaging. Cells lacking Nvj1 exhibit approximately a 30-minute delay in growth resumption after re-introduction to glucose.

## Altered mevalonate pathway flux is not due to the general loss of the NVJ

To rule out the possibility that complete ablation of the NVJ contact site itself was responsible for reduced mevalonate pathway flux in *nvj1*Δ cells, we subjected *nvj1*Δ*hmg2*Δ cells expressing either $Nvj1_{FL}$ or $Nvj1_{RK\rightarrow AA}$ to radio-pulse analysis of the mevalonate pathway. Because the $Nvj1_{RK\rightarrow AA}$ mutant still formed NVJs but did not recruit Hmg1, we were able to more precisely determine the role of Hmg1 partitioning specifically on mevalonate pathway flux. As seen for *nvj1*Δ cells, $Nvj1_{RK\rightarrow AA}$ cells accumulated labeled HMG-CoA after a short

pulse with $^{14}$C-acetate (**Figure 2.6A**). Furthermore, $^{14}$C-labeled squalene, ergosterol, and sterol-esters were significantly decreased in the Nvj1$_{RK\rightarrow AA}$ mutant, while DAG production was unaffected (**Figure 2.6B-D**; **Supplementary Figure 2.6A,B**). We also observed by single-cell time lapse imaging that the Nvj1$_{RK\rightarrow AA}$ mutant cells experience growth resumption delay following an SC to SC+glucose media transition, similar to *nvj1*Δ cells (**Figure 2.6E,F**). It is unlikely that these effects can be contributed to different Hmg1 expression in the given backgrounds, as Hmg1-mRuby3 fluorescence intensity in Nvj1$_{FL}$ and Nvj1$_{RK\rightarrow AA}$ cells were comparable during AGR (**Supplementary Figure 2.6C**). Overall, this further supports a model where Hmg1 partitioning at the NVJ, and not simply the presence of an NVJ contact, contributes to increased mevalonate pathway flux and resumption of growth following glucose starvation.

**Uncoupling Hmg1 abundance from compartmentalization indicates a role for NVJ partitioning in mevalonate pathway flux**

The AGR-induced increases in Hmg1 protein abundance made it more challenging to specifically dissect the role of Hmg1 spatial compartmentalization in mevalonate metabolism. To mechanistically dissect this compartmentalization and uncouple it from Hmg1 protein level, we generated yeast strains lacking endogenous Hmg1 and Hmg2 and expressing Hmg1-GFP from a non-native *ADH* promoter (**Figure 2.6G**). This new strain (ADHpr:Hmg1-GFP) maintained similar Hmg1-GFP protein levels with and without AGR treatment, and in the presence or absence of Nvj1 (**Figure 2.6H**). Critically, ADHpr:Hmg1-GFP yeast still partitioned Hmg1-GFP at the NVJ during AGR in an Nvj1-dependent manner, indicating we had uncoupled Hmg1 protein levels from Hmg1-GFP spatial compartmentalization (**Figure 2.6I**).

Next, we dissected whether loss of NVJ spatial compartmentalization in this ADHpr:Hmg1-GFP yeast impacted mevalonate pathway flux. Radio-pulse analysis revealed that *nvj1*Δ yeast with ADHpr:Hmg1-GFP displayed exacerbated alterations in mevalonate pathway flux, exhibiting elevated $^{14}$C-labeled HMG-CoA levels and decreased $^{14}$C-squalene, ergosterol, and

SEs (**Figure 2.6J-M**, **Supplementary Figure 2.6D**). Once again, $^{14}$C-DAG levels were unaffected, indicating that *nvj1*Δ yeast manifested specific defects in mevalonate metabolism and not other ER-associated lipid metabolic pathways (**Supplementary Figure 2.6E**). This suggests that Hmg1-GFP NVJ spatial partitioning, independent of Hmg1 protein levels, promotes mevalonate pathway flux.

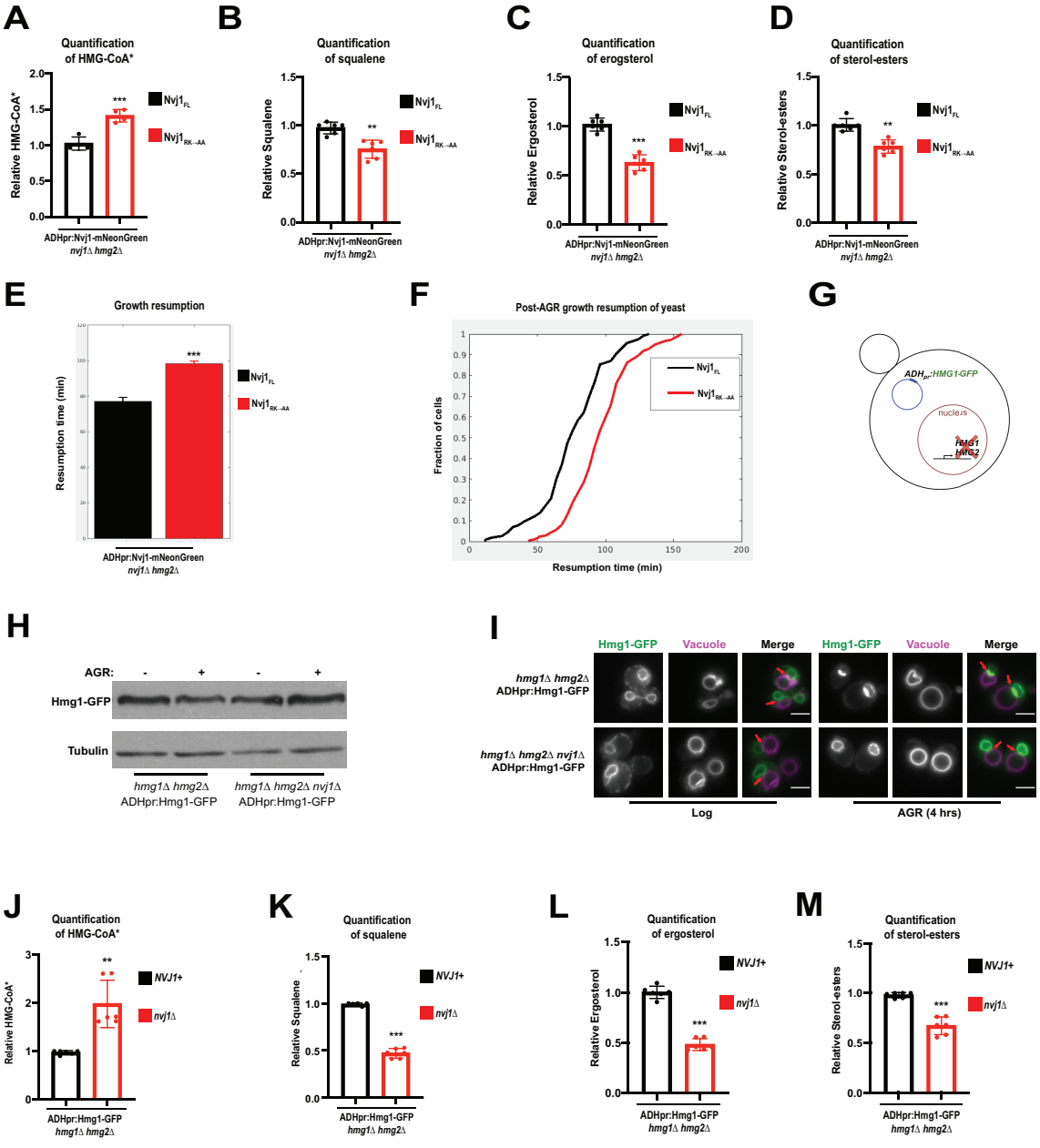

**Figure 2.6. AGR-induced compartmentalization of Hmg1 increases enzymatic efficiency**

**A)** Quantification of radiolabeled HMG-CoA* from *nvj1*Δ*hmg2*Δ yeast expressing either $Nvj1_{FL}$ or $Nvj1_{RK\rightarrow AA}$. Growth and radiolabeling was performed as described above. (Brown-Forsyth and Welch ANOVA. N=6. ***p-value<0.001).

**B-D)** Quantification of radiolabeled squalene, ergosterol, and SE produced from a 15-minute radio-labeling pulse in *nvj1*Δ*hmg2*Δ yeast expressing either $Nvj1_{FL}$ or $Nvj1_{RK\rightarrow AA}$. (Brown-Forsyth and Welch ANOVA. N=6. **p-value<0.01, ***p-value<0.001).

**E)** Quantification of growth resumption times during SC to SC+glucose transition in *nvj1*Δ*hmg2*Δ yeast expressing either $Nvj1_{FL}$ or $Nvj1_{RK\rightarrow AA}$ (N>82 cells).

**F)** Resumption probability graph depicting probability of cells producing a daughter bud as a function of time following an SC to SC+glucose transition ($N\geq 82$ cells) (***p<0.0001, Kolmogorov-Smirnov test).

**G)** Cartoon representation of ADHpr:Hmg1-GFP strains. Strains were generated by removal of endogenous Hmg1 and Hmg2, and replacing with ADH promoter-driven Hmg1-GFP (ADHpr:Hmg1-GFP).

**H)** Immunoblot of Hmg1-GFP isolated from ADHpr:Hmg1-GFP strains before or after treatment with AGR. Tubulin was used as a loading control.

**I)** Epifluorescence imaging of ADHpr:Hmg1-GFP strains showing that Hmg1 NVJ partitioning can be uncoupled from endogenous protein expression. Red arrows indicate relative position of the NVJ. Scale bars = 0.5μm.

**J)** Quantification of radiolabeled HMG-CoA* from yeast expressing ADHpr:Hmg1-GFP in wildtype (*NVJ1*+) or *nvj1*Δ yeast. Growth and radiolabeling was performed as described above. (Brown-Forsyth and Welch ANOVA. N=6. **p-value<0.01).

**K-M)** Quantification of squalene, ergosterol, and SE produced from a 15 minutes radio-labeling pulse in ADHpr:Hmg1-GFP strains. (Brown-Forsyth and Welch ANOVA. N=6. ***p-value<0.001).

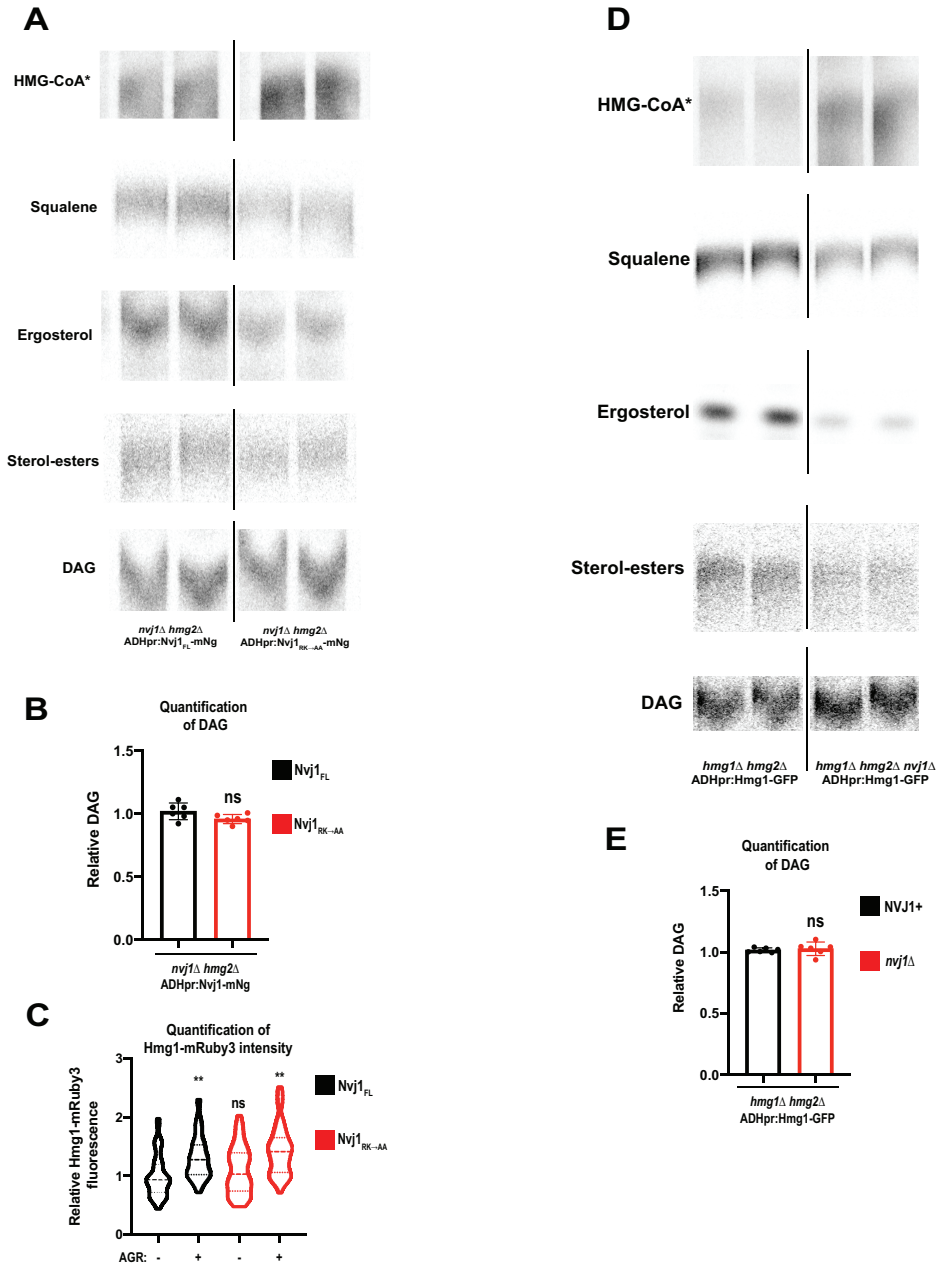


**Supplementary Figure 2.6. Cells expressing ADHpr:Hmg1-GFP in the absence of endogenous Nvj1 have exacerbated Hmg1 catalytic deficiency phenotype**

**A)** Autoradiograms taken of TLC plates to visualize HMG-CoA*, squalene, ergosterol, SE, and DAG in *nvj1Δhmg2Δ* cells expressing either $Nvj1_{FL}$ or $Nvj1_{RK\rightarrow AA}$. Bands were visualized as described in Fig S3.

**B)** Densitometry quantification of DAG bands as shown in (A). (Brown-Forsyth and Welch ANOVA. N=6).

**C)** Quantification of Hmg1-mRuby3 signal in log phase or after four hours of AGR treatment in *nvj1Δhmg2Δ* cells expressing either $Nvj1_{FL}$ or $Nvj1_{RK\rightarrow AA}$. (Brown-Forsyth and Welch ANOVA. N=88. **p-value<0.01).

**D)** Autoradiograms taken of TLC plates to visualize HMG-CoA*, squalene, ergosterol, SE, and DAG in ADHpr:Hmg1-GFP lines in the presence or absence of Nvj1. Bands were visualized as described in Fig S3.

**E)** Densitometry quantification of DAG bands as shown in (D). (Brown-Forsyth and Welch ANOVA. N=6).

**Loss of Hmg1 NVJ partitioning can be bypassed by compartmentalizing Hmg1 via artificial multimerization**

Bioengineering studies indicate that HMGCR enzymatic domains exhibit enhanced catalytic activity when forced into close proximities via multi-valent flexible scaffolds (Dueber et al., 2009). Similarly, human HMGCR requires tetramerization for catalytic activity (Istvan et al., 2000). We hypothesized that Hmg1 NVJ partitioning may enhance enzymatic activity by promoting the probability of close physical associations between HMGCR enzymes as they are retained in NVJ. Indeed, when we analyzed Hmg1-3HA using blue native PAGE (BN-PAGE) we found that Hmg1 associated in high molecular weight (HMW) species corresponding to an approximate molecular mass of 720kDa (**Figure 2.7A,B**). Appearance of Hmg1 HMW species was dramatically increased during AGR, and HMW species were significantly reduced in *nvj1*Δ cells. Differences in HMW species abundance was not simply due to Hmg1-3HA expression, as the trend was observed even when Hmg1-3HA loading was adjusted evenly as observed by SDS-PAGE from the same samples (**Figure 2.7A, B**).

To test whether loss of Hmg1 HMW species in *nvj1*Δ cells was contributing to lower mevalonate pathway flux, we fused Hmg1 to a constitutively tetrameric fluorescent protein, DsRed2, and determined whether this artificial multimerization could bypass the loss of NVJ-mediated compartmentalization by comparing it to Hmg1 tagged with a monomeric fluorescent protein, mRuby3 (**Figure 2.7C**). Both Hmg1-mRuby3 and Hmg1-DsRed2 tagged strains manifested similar increases in Hmg1 abundance in AGR, suggesting this tagging did not affect AGR-induced Hmg1 protein increase (**Supplementary Figure 2.7D**). Furthermore, Hmg1-DsRed2 protein migrated at higher than expected molecular weight even in SDS-PAGE gels compared to Hmg1-mRuby3, suggesting the DsRed2 tag promoted self-association (**Supplementary Figure 2.7E**). Hmg1-DsRed2 foci were also noted on the NE during AGR, consistent with stabilized Hmg1 multimers (**Supplementary Figure 2.7A**).

As expected, *nvj1*Δ cells tagged with mRuby3 still manifested elevated $^{14}$C-labeled HMG-CoA and reduced squalene, ergosterol, and SE labeling associated with NVJ loss (**Figure 2.7D-G**). Strikingly, these perturbations were rescued in the *nvj1*Δ Hmg1-DsRed2 strain, closely

mirroring wildtype $^{14}$C-labeled levels of Hmg-CoA, squalene, ergosterol, and SE (**Figure 2.7D-G**, **Supplementary Figure 2.7B,C**). Once again, appending either mRuby3 or DsRed2 tags to Hmg1 did not significantly alter expression of the protein from what was observed with other tags, and our data cannot be explained by differences in Hmg1 expression alone (**Supplementary Figure 2.7D**). Collectively, this indicates that artificial multimerization of Hmg1 can bypass the loss of NVJ-mediated Hmg1 compartmentalization.

Next, we interrogated whether Hmg1-DsRed2 tagging would rescue the growth resumption delay observed for *nvj1*Δ yeast following 10hr exposure to SC media lacking glucose. As expected, growth resumption delay was observed in *nvj1*Δ yeast expressing Hmg1-mRuby3. Remarkably, expression of Hmg1-DsRed2 in *nvj1*Δ cells rescued this defect (**Figure 2.7H, I**). Collectively, this is consistent with a model where NVJ-dependent Hmg1 spatial compartmentalization via NVJ partitioning or artificial multimerization enhances mevalonate pathway flux as well as defects in growth resumption following glucose starvation.

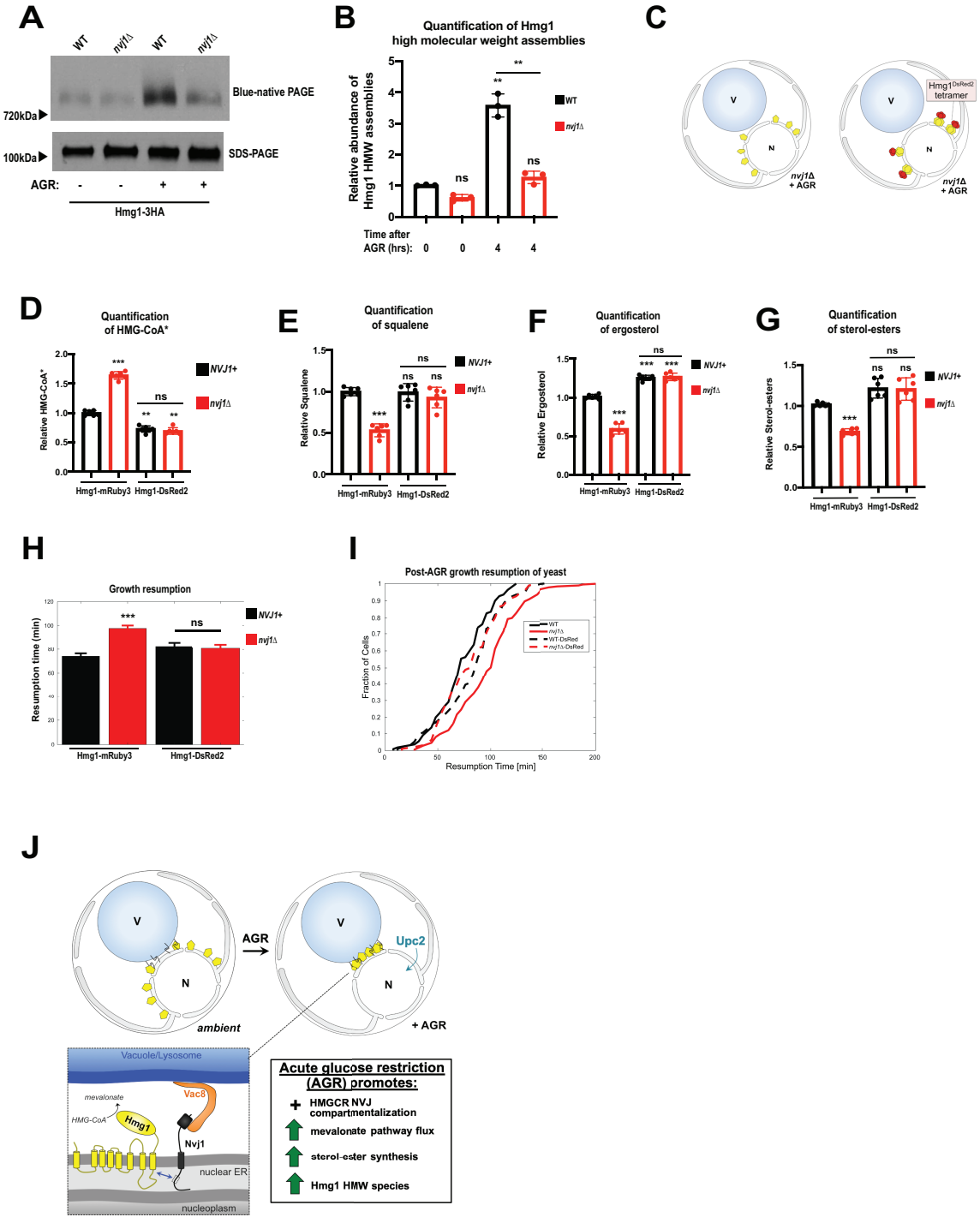


**Figure 2.7. Artificial multimerization of Hmg1 rescues enzymatic deficiencies of *nvj1*Δ cells**

**A)** Blue native PAGE (BN-PAGE) and SDS-PAGE analysis of Hmg1-3HA expressed in either WT or *nvj1*Δ cells under log-phase or AGR growth conditions. Samples were loaded to mitigate differences in total Hmg1 loading such that differences in the BN-PAGE could be easily interpreted. Arrows on the side indicate relative molecular mass in corresponding region as determined by molecular weight standards.

**B)** Quantification of BN-PAGE and SDS-PAGE analysis as shown in (A). For quantification of relative Hmg1-3HA abundance in HMW species, fold change relative to WT log samples were first calculated for BN-PAGE species and subsequently normalized by total expression of Hmg1 in each sample/condition as determined by SDS-PAGE. (Brown-Forsyth and Welch ANOVA. N=3. **p-value<0.01).
**C)** Cartoon representation of Hmg1 artificial tetramerization by DsRed2 tagging in *nvj1*Δ cells.
**D)** Scintillation counting quantification of radiolabeled HMG-CoA* from yeast expressing endogenously tagged monomeric Hmg1-mRuby3 or tetrameric Hmg1-DsRed2 in wildtype (*NVJ1*+) or *nvj1*Δ yeast. Quantification performed as in (Fig 6A). (Brown-Forsyth and Welch ANOVA. N=6. **p-value<0.01 ***p-value<0.001).
**E-G)** Quantification of radiolabeled squalene, ergosterol, and SE produced in Hmg1-mRuby3 or Hmg1-DsRed2 yeast. Radio labeling and quantifications performed as in (Fig 6B-D). (Brown-Forsyth and Welch ANOVA. N=6. ***p-value<0.001).
**H)** Average growth resumption times measured by single-cell time lapse microscopy. (WT: N=110, nvj1Δ: N=175, WT Hmg1-DsRed2: N=94, nvj1Δ Hmg1-DsRed2: N=96). (N≥94 cells, **p<0.001, Kolmogorov-Smirnov test).
**I)** Resumption probability graph depicting probability of cells producing a daughter bud as a function of time following an SC to SC+glucose transition. (N≥94 cells).
**J)** Cartoon representation of Nvj1 and Upc2-mediated Hmg1 partitioning at the NVJ. Spatial partitioning of Hmg1 at the NVJ coincides with increased production of mevalonate-derived metabolites.

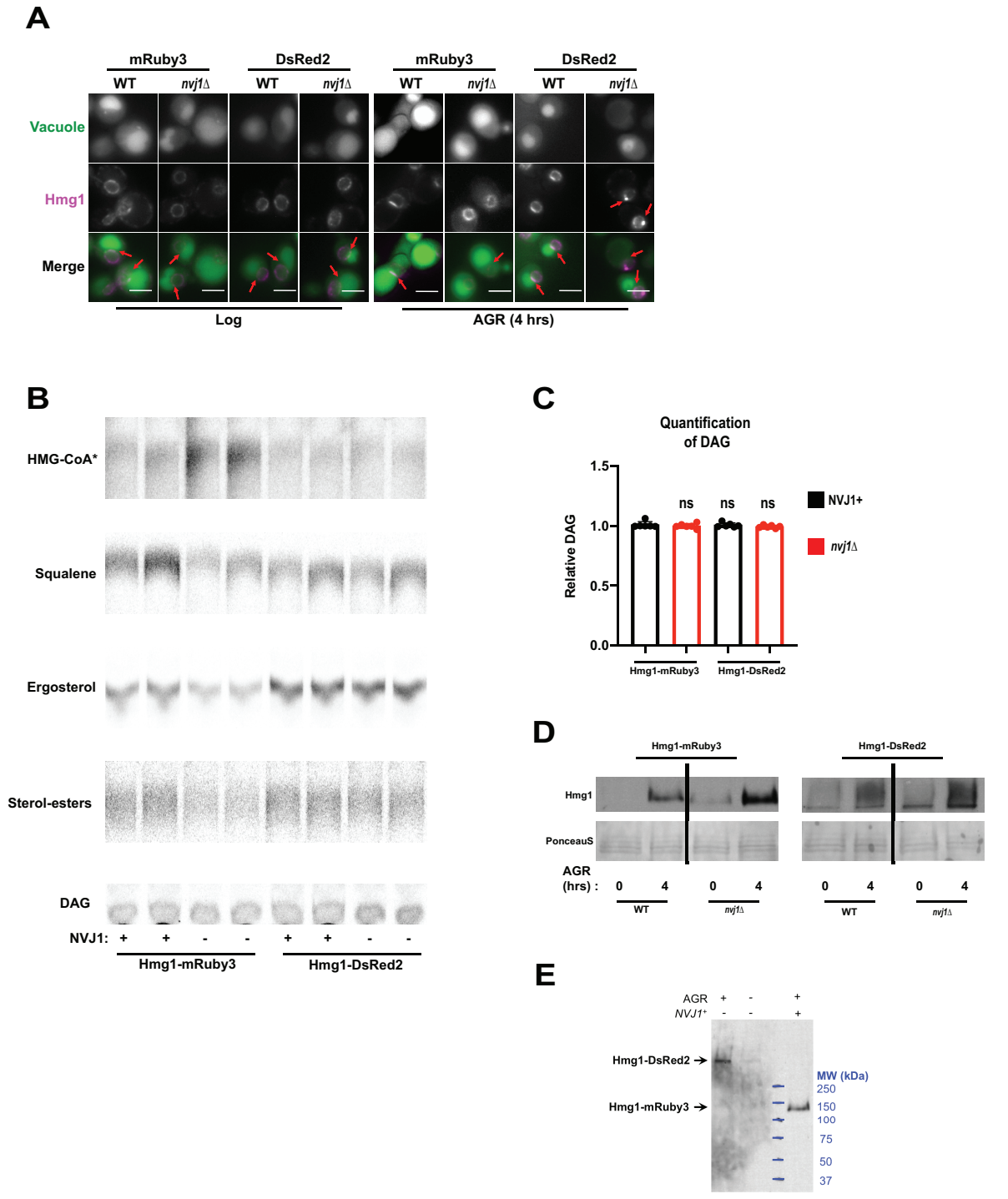


**Supplementary Figure 2.7. Artificial inter-enzyme association via DsRed2 tagging rescues *nvj1*Δ associated Hmg1 catalytic deficiency**

**A)** Epifluorescence imaging of yeast expressing endogenously tagged Hmg1-mRuby3 or Hmg1-DsRed2 (magenta) in log-phase and after four hours of AGR treatment. Vacuoles (green) were stained by incubating yeast with 5µg/mL

CMAC dye for two hours prior to imaging. Red arrows in merged images indicate the NVJ. Red arrows in the Hmg1-DsRed2 *nvj1*Δ AGR-treated greyscale image indicates prominent Hmg1-positive foci on the NE. Scale bars=0.5μm.
**B)** Autoradiograms taken of TLC plates to visualize HMG-CoA* (as previously described) or squalene, ergosterol, SE, and DAG in cells expressing endogenously tagged monomeric Hmg1-mRuby3 or tetrameric Hmg1-DsRed2 in the presence or absence of endogenous Nvj1. Bands were visualized as described in Fig S3.
**C)** Densitometry quantification of DAG bands as shown in (A). (Brown-Forsyth and Welch ANOVA. N=6).
**D)** Immunoblot analysis of Hmg1-mRuby3 and Hmg1-DsRed2 strains expressed in either WT or *nvj1*Δ yeast. PonceauS total protein stain was used as a loading control.
**E)** Immunoblot analysis of Hmg1-DsRed2 and Hmg1-mRuby3 strains indicating that Hmg1-DsRed2 runs higher in the SDS-PAGE gel than expected. Blue lines indicate position of molecular weight standards. One lane of Hmg1-mRuby3 is included for comparison.

## Discussion

Acute changes in nutrient availability trigger metabolic remodeling that is characterized by alterations in metabolic pathway flux and metabolite supply and demand. How cells spatially and temporally coordinate this remodeling remains poorly characterized, yet critical to our understanding to cell adaptation and survival. Changes in nutrient availability can drive the sub-cellular re-distribution of enzymes within cells, as well as the formation of enzyme assemblies or complexes that promote or fine-tune metabolic pathways. Here, we present evidence that AGR in yeast enhances mevalonate pathway flux, and propose the mechanism underlying this requires the spatial compartmentalization of the rate-limiting HMGCR enzymes at the yeast NVJ (**Figure 2.7J**).

Through time-lapse and FRAP/FLIP-based imaging, we find that Hmg1 is recruited and selectively retained at the NVJ in a manner requiring basic residues within the Nvj1 luminal domain. We also demonstrate that Hmg1 partitioning at the NVJ can be uncoupled from Nvj1 binding of Vac8, which further supports a model where Hmg1 partitioning is being controlled predominantly from the ER. One model is that Hmg1 is selectively recruited as an enzyme "client" to the Nvj1 "scaffold" during AGR, but we cannot rule out the possibility that other factors may be involved together with Nvj1 in Hmg1 selective retention at the NVJ. Indeed, Upc2, a sterol-sensing transcription factor required for Hmg1 NVJ partitioning, appears to influence Hmg1 independent of either Nvj1 expression or localization, which may suggest additional factors required for Hmg1 partitioning at the NVJ. Both the requirement of Upc2 and the sufficiency of the Erg1 inhibitor terbinafine to induce Hmg1 NVJ partitioning is

consistent with AGR stress producing a cellular demand for mevalonate. In line with this, we observe an increase in *de novo* SE synthesis during AGR; however, we cannot rule out that other mevalonate-derived metabolites may play important roles during AGR. In fact, we would expect AGR to promote a metabolic switch to mitochondrial respiration, which in part utilizes at least one mevalonate-derived metabolite, coenzyme Q, to function as an electron carrier. In support of this, we do not observe significant decline of steady-state SE levels in *nvj1*Δ cells, suggesting that mevalonate may be shunted into several pathways during AGR. Remarkably, *nvj1*Δ yeast manifest alterations in mevalonate pathway flux and growth defects when faced with glucose starvation, which can be rescued by the addition of exogenous mevalonate (the HMGCR enzymatic product).

We have additionally uncovered that mevalonate pathway flux can be rescued in *nvj1*Δ cells by artificially multimerizing Hmg1 using a tetrameric fluorophore. In line with this, we have observed that Hmg1 has a propensity to assemble into HMW species >720kDa during AGR in a Nvj1-dependent manner. Thus, mevalonate pathway flux during AGR appears tightly correlated with the ability to form HMW Hmg1 species at the NVJ, rather than the total Hmg1 protein level in the cell. To more fully dissect the role of HMGCR spatial compartmentalization on mevalonate metabolism, we generated an artificial yeast strain that maintains more constant Hmg1 protein levels and inducibly accumulates at the NVJ, thus functionally uncoupling Hmg1 protein abundance from NVJ spatial compartmentalization. Remarkably, this strain exhibits defects in mevalonate pathway flux when Hmg1 cannot be NVJ partitioned, again underscoring the role of Hmg1 spatial compartmentalization in fine-tuning mevalonate metabolism. Collectively, we present a model where AGR-induced metabolic remodeling of mevalonate metabolism is spatially coordinated at the NVJ via selective retention of HMGCRs and their subsequent incorporation into HMW species. An intriguing possibility is that, in general, inter-organelle contact sites act as platforms that slow the diffusion of proteins that enter them via their interactions with resident tether "scaffolds", thus increasing the local concentrations of proteins and enzymes sufficient to fine-tune metabolic flux.

Glucose and other nutrient limitations can induce autophagy and have previously been shown to induce micro-lipophagy, where lipid droplets are engulfed by the yeast vacuole (Seo et al., 2017). Indeed, we have observed that LDs accumulate in close proximity to the NVJ during periods of glucose limitation (Hariri et al., 2018, 2019). The relationship between LD biogenesis and HMGCR partitioning at the NVJ is not fully resolved here and requires further study. An intriguing possibility is that the spatial re-organization of HMGCRs may contribute to LD biogenesis or compositional remodeling during the general metabolic remodeling required during glucose restriction.

In addition to inducing the compartmentalization of HMGCRs at the NVJ, yeast glucose starvation has also been shown to induce the formation of several cytoplasmic enzyme assemblies involved in nucleotide (Ura7), amino acid (Gly1), and lipid (Acs1) metabolism (Munder et al., 2016). These cytoplasmic assemblies are thought to reduce enzymatic activity and promote the transition into cellular dormancy. In contrast, other protein assemblies promote enzymatic activity. In the liver, the protein Mig12 binds to cytosolic acetyl-CoA carboxylases (Acc) and promotes their polymerization and catalytic activity, which elevates fatty acid synthesis and eventual triglyceride accumulation in hepatocytes (Kim et al., 2010). Our work provides evidence that HMGCRs form similar spatial assemblies at yeast ER-lysosome contact sites, implicating a role for inter-organelle junctions in the spatial coordination of metabolically-induced enzymatic assembly formation. With this, we have added to a long, and growing, list for roles fulfilled by inter-organelle contact sites in metabolic regulation.

## CHAPTER THREE

# Liquid-crystalline lipid phase transitions in lipid droplets selectively remodel the LD proteome


### Abstract

Lipid droplets (LDs) are reservoirs for triglycerides (TGs) and sterol-esters (SEs). How lipids are organized within LDs and influence the LD proteome remains unclear. Using *in situ* cryo-electron tomography, we show that glucose restriction triggers lipid phase transitions within LDs creating liquid-crystalline lattices inside them. Mechanistically, this requires TG lipolysis, which alters LD neutral lipid composition and promotes SE transition to a liquid-crystalline phase. Fluorescence imaging and proteomics further reveal that LD liquid-crystalline lattices selectively remodel the LD proteome. Canonical LD proteins including Erg6 re-localize to the ER network, whereas others remain on LDs. Model protein LiveDrop also redistributes from LDs to the ER, suggesting liquid-crystalline phases influence ER-LD inter-organelle movement. Proteomics also indicates glucose restriction elevates peroxisome lipid oxidation, suggesting TGs provide fatty acids for cellular energetics. We propose that glucose restriction drives TG mobilization that alters the phase properties of LD lipids and selectively remodels the LD proteome.


### Introduction

Lipid droplets (LDs) are unique endoplasmic reticulum (ER)-derived organelles dedicated to the storage of energy-rich neutral lipids. Structurally LDs are composed of a hydrophobic core of triglycerides (TGs) and sterol-esters (SEs) that is surrounded by a phospholipid monolayer that either contains or is decorated by specific proteins. Beyond their roles in energy homeostasis, recent work highlights the roles of LDs in signaling, development, and metabolism (Olzmann and Carvalho, 2019; Walther et al., 2017; Welte and Gould, 2017). These diverse jobs are largely dictated by the LD proteome, but a pervasive question is how

specific proteins are targeted to the LD surface. Furthermore, whether the LD proteome is static or dynamic, and how metabolic cues influence LD protein residency is poorly understood.

LDs are generated at the ER and often remain connected to the ER bilayer for extended periods (Jacquier et al., 2011; Kassan et al., 2013). As such, Type I LD proteins can translocate between the ER and LD monolayer via lipidic bridges connecting the two organelles (Wilfling et al., 2013). Elegant *in vitro* studies have suggested that LD localization promotes energetically favorable conformational changes within some proteins, and the movement of proteins to LDs from the ER network can even influence their enzymatic activities, or target them for degradation (Caillon et al., 2020; Chorlay and Thiam, 2018; Leber et al., 1998; Ohsaki et al., 2006; Schmidt et al., 2013). A second mechanism of LD targeting occurs from the cytoplasm, where soluble proteins insert into the LD monolayer via a hydrophobic region, amphipathic helix, or lipid moiety. Here hydrophobic protein regions recognize packing defects between the phospholipid monolayer lipid head groups, enabling their insertion into the neutral lipid core (Chorlay and Thiam, 2020).

Although monolayer phospholipids can regulate LD protein targeting, how neutral lipids influence protein localization is less understood. However, neutral lipids clearly impact the composition of the LD surface proteome; for example, in yeast, some proteins preferentially decorate TG-rich LDs (Gao et al., 2017). Molecular studies also indicate that protein insertion into the LD neutral lipid core enables proteins to fold with lower free energy, and polar residues within hydrophobic regions can even interact with TG, further anchoring them to the LD (Olarte et al., 2020). However, how neutral lipid pools ultimately influence the composition and dynamics of the LD proteome is relatively unexplored, yet central to our understanding of LD organization and functional diversity.

Neutral lipids generally form an amorphous mixture within the hydrophobic LD core. This organization can change in response to various cellular stimuli. HeLa cells induced into mitotic arrest or starvation exhibit lipid phase transitions within their LDs, generating liquid-crystalline lattices (LCLs) inside LDs with a striking onion-like appearance by cryo-electron tomography (cryo-ET) (Mahamid et al., 2019). Yeast biochemical studies also proposed similar segregation of TGs and SEs into discrete layers within LDs (Czabany et al., 2008). This

lipid reorganization is attributed to the biophysical properties of SEs, which can transition from disordered to ordered smectic phases under physiological conditions (Czabany et al., 2008; Ginsburg et al., 1984; Kroon, 1981; Shimobayashi and Ohsaki, 2019). Such phase transitions are also associated with human pathologies including atherosclerosis, and liquid-crystalline LDs were even observed in the macrophage of a patient with Tangier disease (Katz et al., 1977; Lundberg, 1985). How these phase transitions are triggered, however, and whether they influence organelle physiology, or are simply a biophysical consequence of the properties of SEs, is unknown.

Here, we utilized budding yeast to dissect the metabolic cues governing lipid phase transitions within LDs. We used cryo-ET of cryo-focused ion beam (cryo-FIB) milled yeast cells to study the *in situ* architecture of LDs in their native environment, under ambient or glucose-starved conditions. We show that in response to acute glucose restriction, yeast initiate TG lipolysis, which induces the formation of LCLs within LDs. In line with this lipid mobilization, global proteomics reveals that glucose restriction promotes metabolic remodeling favoring peroxisome fatty acid oxidation. Furthermore, we find LD liquid-crystalline remodeling selectively changes the LD surface proteome, promoting the translocation of some proteins from the LD surface to the ER network while others are retained on LCL-LDs.

## Results

### Acute glucose restriction promotes TG lipolysis-dependent liquid-crystalline phase transitions in LDs

Previous studies from our group indicated that budding yeast exposed to acute glucose restriction (AGR), where yeast are transferred from a glucose-rich (2%) synthetic complete media to a low-glucose (0.001%) media, exhibit metabolic remodeling that favors the production of SEs, which are stored in LDs (Rogers et al., 2021). We used cryo-ET to investigate if AGR also impacts LD morphology. We rapidly froze yeast cells that were either in 2% glucose-fed logarithmic (log-phase) growth or exposed to 4 hrs of AGR, and used cryo-FIB milling to generate 100-200-nm-thick lamellae of the vitrified cells. These lamellae were then imaged by cryo-ET to reveal the three-dimensional (3D) structure of native LDs *in situ*.

The cryo-FIB milled lamella exhibited a well-preserved yeast ultrastructure, including the nucleus, vacuole, mitochondria and LDs (**Figure 3.1A**). Normal LDs could be distinguished from other cellular organelles by their relatively electron-dense, amorphous interior that was surrounded by a thin phospholipid monolayer (**Figure 3.1B**). In contrast to normal LDs in glucose-fed log-phase cells, ~77% of the LDs observed in 4hrs AGR-treated yeast displayed reorganization of their lumen, including the appearance of distinct concentric rings in the LD periphery (**Figure 3.1 C-D, L for quantification**). These rings appear similar to lattices previously observed in liquid-crystalline-phase LDs, which exhibited a regular spacing of ~3.4-3.6nm between their layers, suggesting they were composed of sterol-esters (Engelman and Hillman, 1976; Mahamid et al., 2019). Indeed, our line-scan analysis showed a regular 3.4nm spacing between rings (**Figure 3.1E**), suggesting these LDs exhibited liquid-crystalline lattices (LCLs). Thus, we refer these "onion-like" LDs as LCL-LDs. Notably, these were never observed in the log-phase yeast (**Figure 3.1B, L**).

In addition to the peripheral lattices, the amorphous center of LCL-LDs was unusually sensitive to electron radiation, causing excessive radiolysis and "bubbling" (i.e. the generation of a gas bubble trapped in the ice that appears white in cryo-EM images) during tilt-series acquisition (**Figure 3.1C, white arrow**). This increased radiation sensitivity was only observed in LCL-LDs, but not in LDs with entirely amorphous lumen (i.e. not observed in the 23% unordered LDs of AGR-treated yeast, nor in any LDs of log-phase yeast). We generated comparative 'bubblegrams', i.e. a series of 2D cryo-EM images where the same sample area was exposed to an increasing amount of electron dose, which revealed that the centers of LCL-LDs exhibited bubbling following exposure to <30 e/Å$^2$, whereas amorphous LDs from log-phase yeast did not show any bubbling even at 400 e/Å$^2$ dosages (**Supplementary Figure 3.1A-J**). Previous studies of electron radiation-induced bubbling of frozen biomolecules in aqueous solution and cells demonstrated that similar gas bubbles contained mostly molecular hydrogen (Aronova et al., 2011; Leapman and Sun, 1995). Although the mechanism of radiation-induced bubbling and increased radiation-sensitivity within the center of LCL-LDs is not clear, it may be due to the production of gases derived from a specific combination of lipids or metabolites present within LCL-LDs.

To investigate the effects of AGR stress on yeast neutral lipid pools, we monitored TG and SE levels in log-phase and 4hrs AGR-treated yeast. Indeed, AGR treated yeast contained significantly less TG (**Figure 3.1K)**. As expected, AGR yeast also had increased amounts of SEs (**Figure 3.1K)**, as previously observed (Rogers et al., 2021), indicating the TG:SE ratio within the LDs was significantly decreased to ~0.5:1.5 compared to a normal ratio of ~1:1 (Leber et al., 1994). We hypothesized that LCL-LD formation was promoted by TG loss from LDs. To test this, cryo-ET was performed on yeast lacking the major TG lipases (*tgl3,4,5*Δ). Indeed, 4hrs AGR treated *tgl3,4,5*Δ yeast did not form any detectable LCL-LDs (**Figure 3.1G**), suggesting TG lipolysis was required for LCL-LD formation. In support of this, LDs in wildtype (WT) AGR-treated yeast were significantly smaller in diameter than log-phase LDs, and this reduced size was suppressed in *tgl3,4,5*Δ yeast (**Figure 3.1N**), suggesting the size reduction was due to lipid loss via TG lipolysis.

To further dissect how TGs influence LCL-LDs, we treated yeast with 0.1% oleic acid (OA), which promotes TG synthesis. This considerably increased the size of LDs in glucose-fed log-phase yeast **(Figure 3.1H, N)**. As expected, OA elevated cellular TG levels in yeast when they were cultured in it during 4hrs AGR treatment (**Figure 3.1L**), and notably no LCL-LDs were observed during log-phase nor in this AGR condition (**Figure 3.1F, H, M**). In line with this, whereas LD sizes in AGR-treated yeast were significantly smaller than in log-phase cells, their sizes slightly recovered under the AGR plus OA condition **(Figure 3.1M)**. Since we previously observed that the nucleus-vacuole junction (NVJ) can serve as a site for LD biogenesis during nutrient stress (Hariri et al., 2018), we also examined whether NVJ loss impacted LCL-LD formation. Cryo-ET of *nvj1*Δ yeast cells showed the expected loss of tight contacts between the outer nuclear envelope and the vacuole **(Supplementary Figure 3.1 K, L)**. However, *nvj1*Δ yeast exhibited ~75% LCL-LDs under AGR conditions, indicating that the NVJ was not required for LCL-LD formation (**Figure 3.1I, J, M**).

Since SEs can form liquid-crystalline lattices, we tested whether SEs were required for LCL-LD formation. We monitored LDs in *are1are2*Δ yeast that cannot synthesize SEs. Surprisingly, in cryo-tomograms of *are1are2*Δ yeast no LDs could be observed (**Supplementary Figure 3.1M**). However, fluorescence staining with monodansylpentane (MDH) confirmed the

presence of LDs in *are1are2*Δ yeast during AGR stress, but they were small and sparse in many yeast compared to any of the other examined strains (**Supplementary Figure 3.1N**). The reduction in LD size and abundance may account for the inability to observe LDs in the cryo-tomograms of the 100-200nm thick lamellae.

Collectively, these data suggest that TG abundance is a key modulator of the SE phase transitions within the LD, and indicate Tgl-dependent TG lipolysis during AGR promotes LCL-LD formation by depleting the TG pool that maintains SE in its disordered phase.

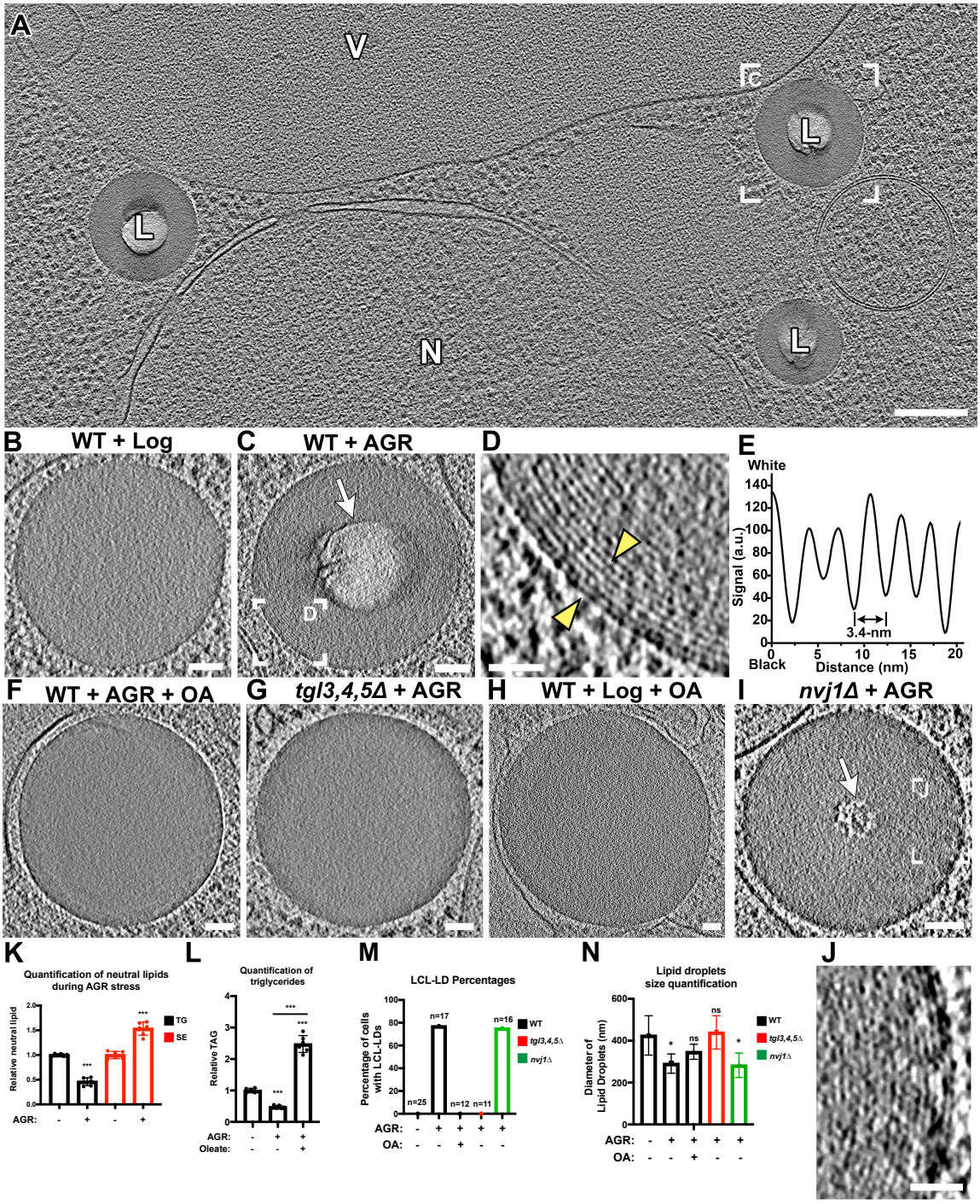


**Figure 3.1. Visualization of the liquid-crystalline layers in lipid droplets (LCL-LD) promoted by TG lipolysis using *in situ* cryo-ET.**

**A)** Representative tomographic slice from a cryo-FIB-milled and cryo-ET reconstructed wildtype (WT) yeast cell grown for 4hrs under acute glucose restriction (AGR). Note the "bubbled" (lighter) centers of the LDs (L). V, vacuole. N, nucleus. A different tomographic slice of the boxed LD is also shown in (C).

**B-J)** Representative tomographic slices of LDs in yeast

**C)** WT after 4hrs AGR (C, boxed area magnified in D, E shows line-scan plot of area between yellow arrowheads)
**F)** WT after 4hrs AGR + 0.1% oleate (OA)
**G),** *tgl3,4,5*Δ yeast after 4hrs AGR
**H)** WT cultured with 2% glucose and 0.1% OA
**I)** *nvj1*Δ after 4hrs AGR (I, and boxed area magnified in J)**.** White arrows highlight the 'bubbles' due to electron radiation in centers of LCL-LDs.
**K)** Quantification of relative whole-cell TGs and SEs in log and 4hrs AGR conditions.
**L)** Relative TGs in log and 4hrs AGR conditions
**M, N)** % abundance of LCL-LDs (M) and diameters of LDs (N) under various conditions measured in cryo-tomograms. Note that the observed diameter depends on the plane at which the LDs were sectioned; therefore, for size measurements, only LDs with clearly visible monolayer (indicating a slice through the LD center) were included. Scale bars: 200nm (A). 50nm (B-C, F-I). 20nm (D, J).

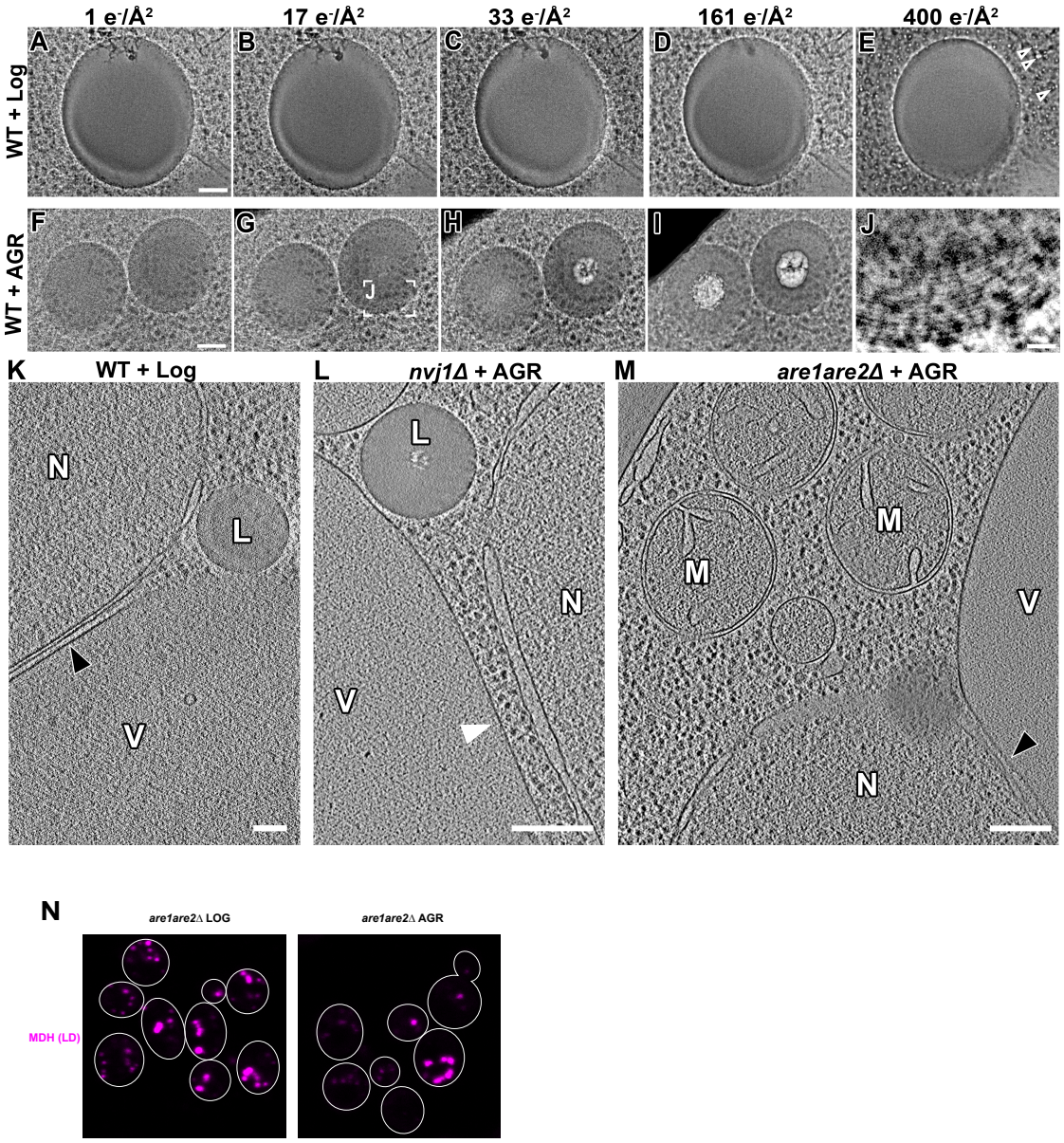


**Supplementary Figure 3.1. LD lipid phase transitions characterized by cryo-FIB and cryo-ET**

**A-J)** Electron dose series ("bubblegrams") for LDs from cryo-FIB milled WT yeast in log phase (A-E) or after AGR (F-J); series of 2D cryo-EM images were recorded of the same LDs exposed to increasing electron dose (1 - 400 e-/Å2). Note that liquid-crystalline layers (LCLs) (see box in G magnified in J) and excessive bubbling in LD centers (starting at an electron dose <30 e-/Å$^2$) occurred only under AGR. Even at 400 e-/Å$^2$ electron dose, minimal bubbling (white arrowheads in E).was observed in log WT.
**K-M)** Representative tomographic slices from cryo-FIB-milled and cryo-ET reconstructed WT in log phase (K), *nvj1Δ* yeasts after 4hrs AGR (L), and *are1are2Δ* yeast after 4hrs AGR (M). The nucleus-vacuole junction (black arrowheads in K and M) was observed in WT and *are1are2Δ* yeasts, but absent in *nvj1Δ* yeast (white arrowhead in L). No LDs were found in *are1are2Δ* yeast. V, vacuole. N, nucleus. L, lipid droplet, M, mitochondrion.
**N)** Yeast stained with LD marker MDH in log and 4hrs AGR. Scale bars: 50nm (A-I), 200nm (K-M), 25nm (J)

## LCL-LD formation selectively remodels the LD proteome

While studies indicate that LD proteins may interact with TGs contained within the LD interior (Olarte et al., 2020; Santinho et al., 2021), it is unknown whether smectic phase transitions influence LD protein targeting. Therefore, we imaged the canonical LD protein Erg6 tagged with mNeonGreen (Erg6-mNg) over time in AGR conditions. As expected, Erg6-mNg initially colocalized with monodansylpentane (MDH) LD stain at the start of AGR (t=0). However, the Erg6 staining pattern changed after ~1hr AGR, and primarily decorated the cortical ER and nuclear envelope (**Figure 3.2A**). Erg6-mNg remained at the ER network throughout 2, 4, and 24 hrs AGR, and notably the LD stain gradually dimmed over these time-points, consistent with the loss of LD volume via lipolysis. Notably, the addition of 0.1% OA, or genetic ablation of TG lipases, rescued Erg6-mNg LD targeting at 4hrs AGR (**Figure 3.2B, Supplementary Figure 3.2A**). Since our cryo-ET results showed lack of LCL-LD formation in these conditions, it suggested that Erg6-mNg de-localization from LDs tightly correlates with LCL-LD formation.

To more directly test whether the biophysical properties of LD lipids influenced Erg6-mNg localization, rather than other metabolic changes attributed to AGR stress, we briefly heated Erg6-mNg expressing yeast after 4hrs AGR to 40°C, which is above the predicted phase transition temperature for smectic-phase SEs. Indeed, Erg6-mNg significantly, although not fully, re-localized from the ER network to LDs after only 15 minutes at 40°C (**Figure 3.2B**). To quantify the extent of Erg6-mNg LD localization, we calculated its relative Manders M1 coefficient, which measures total Erg6-mNg signal that overlaps with LD marker MDH. 4hrs AGR stress was accompanied by an ~75% decrease in Erg6-mNg positive LDs (**Figure 3.2C**).

In agreement with imaging, addition of 0.1% OA returned the M1 coefficient to WT values. Brief heating also significantly, though not fully, increased the M1 coefficient.

Next, we investigated whether AGR caused a general de-localization of other canonical LD proteins from LDs. However, Pln1-mNg, a perilipin-like protein also known as Pet10 (Gao et al., 2017), maintained stable LD association following 4hrs AGR, suggesting the de-localization of LD proteins during LCL-LD formation may be selective (**Figure 3.2D, E**). Recently, perilipin homo-oligomerization was proposed to contribute to the stable association of perilipins on LDs (Giménez-Andrés et al., 2021). To test whether oligomerization could enhance LD protein targeting during AGR, we artificially oligomerized Erg6 by tagging it with tetrameric DsRed2. Indeed, unlike monomeric Erg6-mNg, Erg6-DsRed2 maintained LD targeting during 4hrs AGR (**Supplementary Figure 3.2B**). Collectively, this suggests that: 1) LD protein de-localization during AGR-associated LCL-LD formation may be selective for certain proteins, and 2) oligomerization may enhance protein retention on these LDs.

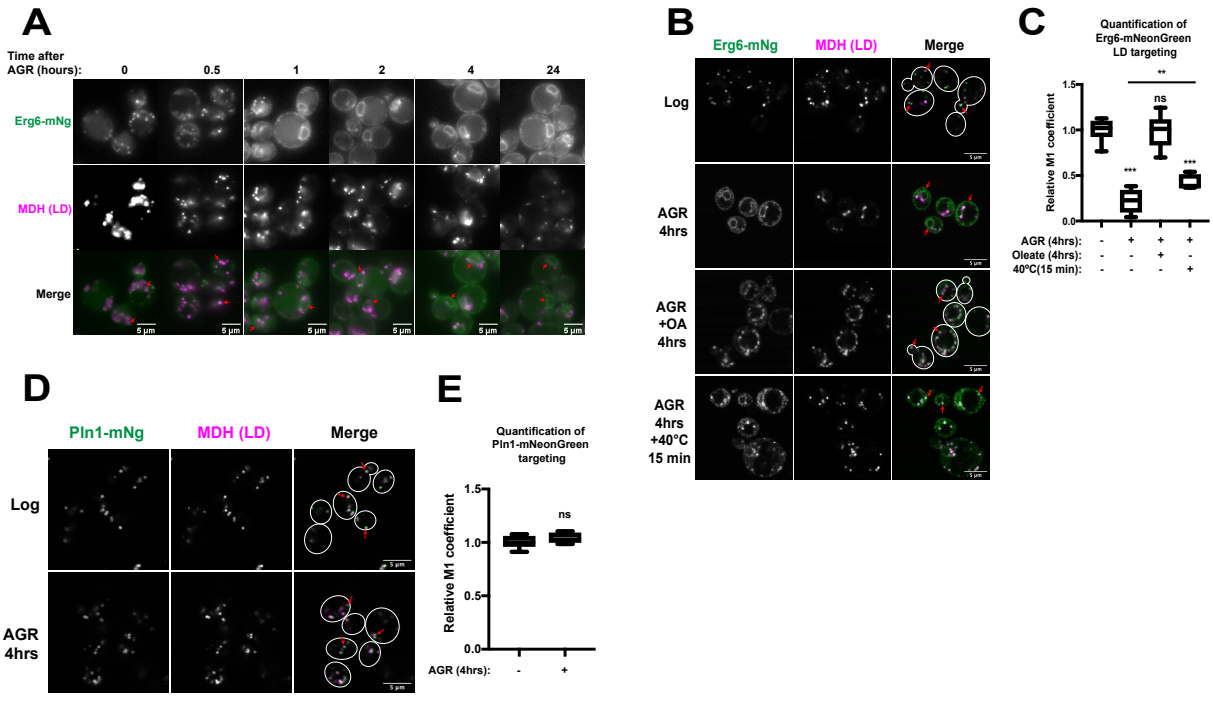


**Figure 3.2. Erg6 LD de-localization correlates with LCL-LD formation.**

**A)** Yeast expressing Erg6-mNeonGreen (mNg) and stained for LDs (monodansylpentane, MDH) at time-points when yeasts were transferred from log-phase (2% glucose) to acute glucose restriction (AGR). Red arrows indicate protein targeting.
**B)** Yeast with Erg6-mNg and LD/MDH stain in log-phase (2% glucose), AGR, and AGR+0.1% oleate (OA), and AGR+15min 40°C.
**C)** Manders M1 coefficient of Erg6-mNg colocalization with LD stain MDH in various conditions**.**
**D)** Pln1/Pet10-mNg in log and 4hrs AGR.
**E)** M1 coefficient of Pln1-mNG with LD targeting. Statistics are one-way ANOVA. Scale bars 5µm.

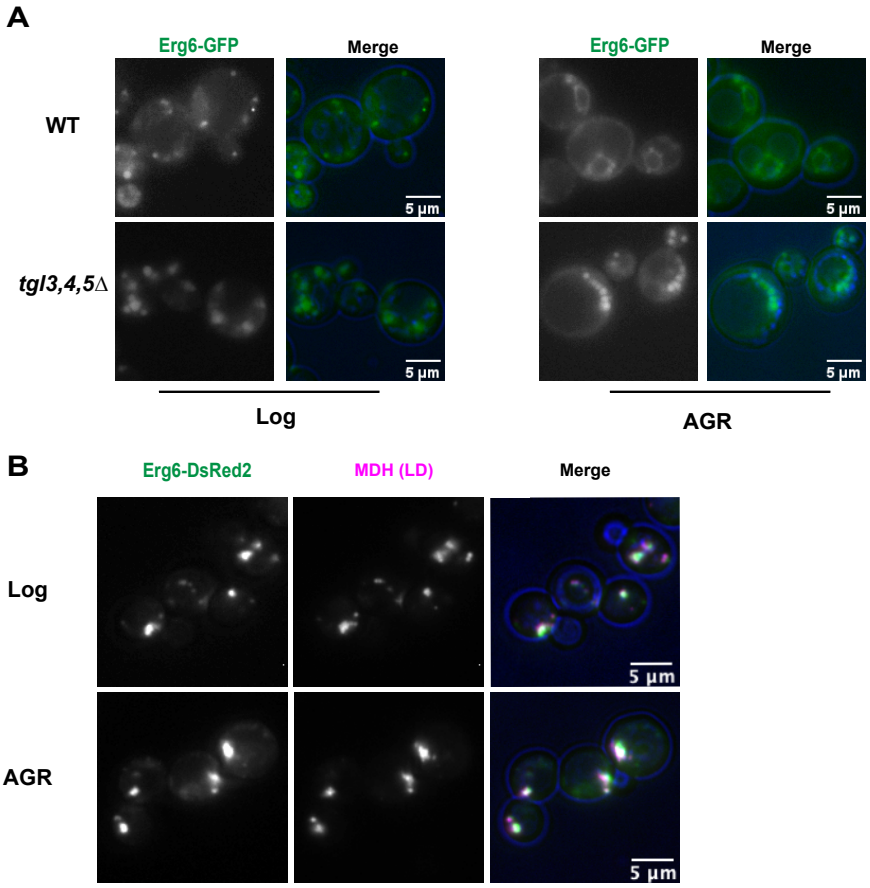


**Supplementary Figure 3.2. Erg6 LD targeting is influenced by AGR-associated LCL-LD formation.**
**A)** WT or *tgl3,4,5Δ* Erg6-GFP yeast in log or AGR conditions.
**B)** Erg6-DsRed2 localized to LDs in log and 4hrs AGR. Scale bars 5µm

## Imaging known LD proteins reveals their selective retargeting to the ER during AGR

Given the different targeting patterns of Erg6 and Pln1 in AGR, we next examined the localization of other annotated LD proteins by tagging them with mNeonGreen (mNg) and examining them in log-phase and 4hrs AGR treated yeast. As expected two LD proteins, Rer2-

mNg and Hfd1-mNg, primarily decorated LDs in log-phase yeast. However, both displayed ER and nuclear envelope localization after 4hrs AGR, and displayed significantly reduced M1 coefficients, similar to Erg6 (**Figure 3.3A, B**). Similarly, Yeh1-mNg, a LD-localized SE lipase, decorated LDs in log-phase yeast, but was primarily localized to the ER network following 4hrs AGR. We also imaged mNg-Say1, which is annotated to target both LDs and the ER network. Indeed, in log-phase yeast mNg-Say1 showed bright LD localization with some ER targeting. However, following 4hrs AGR the LD targeting was reduced and ER targeting appeared more distinct. This corresponded with a decreased M1 coefficient for LD colocalization, suggesting mNg-Say1 distributed more to the ER network versus LDs in AGR (**Figure 3.3A, B**). Similarly, Ayr1-mNg (a bifunctional lipase), as well as Anr2-mNg (a LD protein of unknown function predicted to be palmitoylated) also localized to LDs in log-phase yeast, but displayed primarily ER network targeting in 4hrs AGR (**SFigure 3A**). Collectively, this suggests that similar to Erg6, many canonical LD proteins exhibit more ER localization following AGR exposure, and indicates that LCL-LD formation may alter the protein composition of the LD surface.

Protein movement between the LD and ER compartments has previously been described for Type I LD proteins, which move between the ER and LDs via lipidic bridges connecting them (Wang et al., 2016). Although we observed several proteins that localized more prominently at the ER versus LDs during AGR, whether any of these represent canonical Type I LD proteins was not clear. Therefore, to interrogate whether Type I LD proteins could be re-targeted to the ER during LCL-LD formation, we monitored GFP-tagged LiveDrop (Wang et al., 2016), a minimal model polypeptide for Type I LD proteins, in log-phase and 4hrs AGR-treated yeast. As expected, GFP-LiveDrop localized predominantly to LDs in log-phase yeast, but a dim ER network signal was also detected, consistent with its dual organelle targeting (**Figure 3.3C**). In contrast, following 4hrs AGR GFP-LiveDrop was more prominently at the ER network, and its M1 coefficient was significantly decreased (**Figure 3.3C, D**). This suggests that AGR and its associated LCL-LD formation promotes the re-distribution or retention of Type I LD proteins at the ER network versus LDs.

Since TG lipases were required for LCL-LD formation in AGR (**Figure 3.1G,L**), we next monitored the sub-cellular localization of all Tgl lipases by fluorescence microscopy. As expected the major TG lipase Tgl3-mNg as well as Tgl4-mNg (TG lipase) and Tgl1-mNg (SE lipase) all decorated LDs in log-phase yeast (**Figure 3.3E,F**). Remarkably, all three proteins retained LD localization following 4hrs AGR, likewise displaying unaltered M1 coefficients. Tgl5-mNg (TG lipase) also displayed LD targeting in both log-phase and 4hrs AGR yeast (**Supplementary Figure 3.3B**). This suggests that in contrast to several other LD proteins, Tgl lipases maintain LD association during AGR, where they locally deplete the LD TG pool which, in turn, promotes lipid phase transitions within the LD.

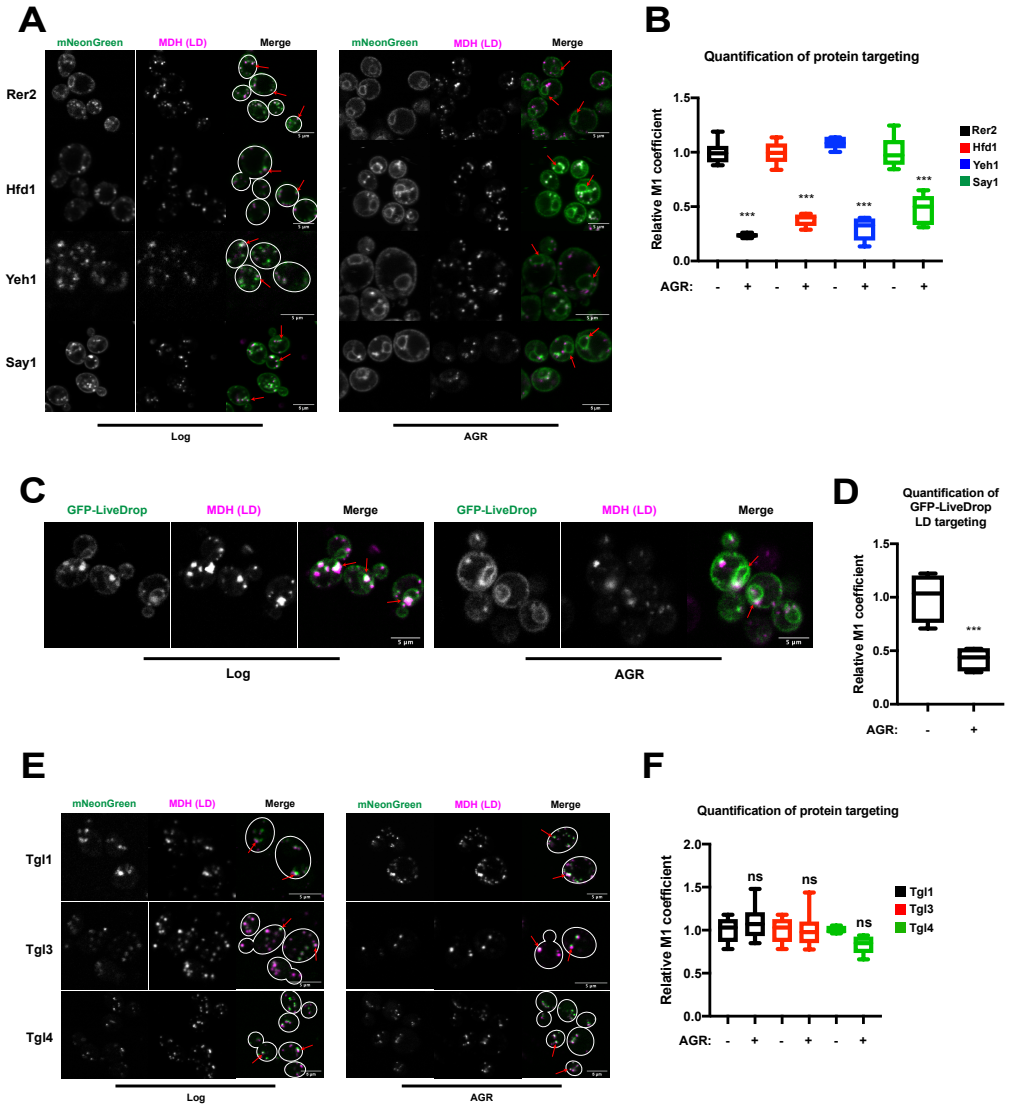


**Figure 3.3. Fluorescence imaging reveals selective remodeling of LD proteome during AGR.**
**A)** Yeast with mNeongreen (mNg)-tagged LD proteins with MDH LD stain in log and 4hrs AGR.
**B)** M1 coefficient of proteins in A.
**C)** Yeast with GFP-LiveDrop and MDH LD stain in log and 4hrs AGR yeast.
**D)** M1 coefficient of proteins in C.
**E)** Yeast with mNg-tagged Tgl1,3,4 and stained with MDH LD marker in log-phase or 4hrs AGR.
**F)** M1 coefficient of proteins in E. Scale bars 5µm.

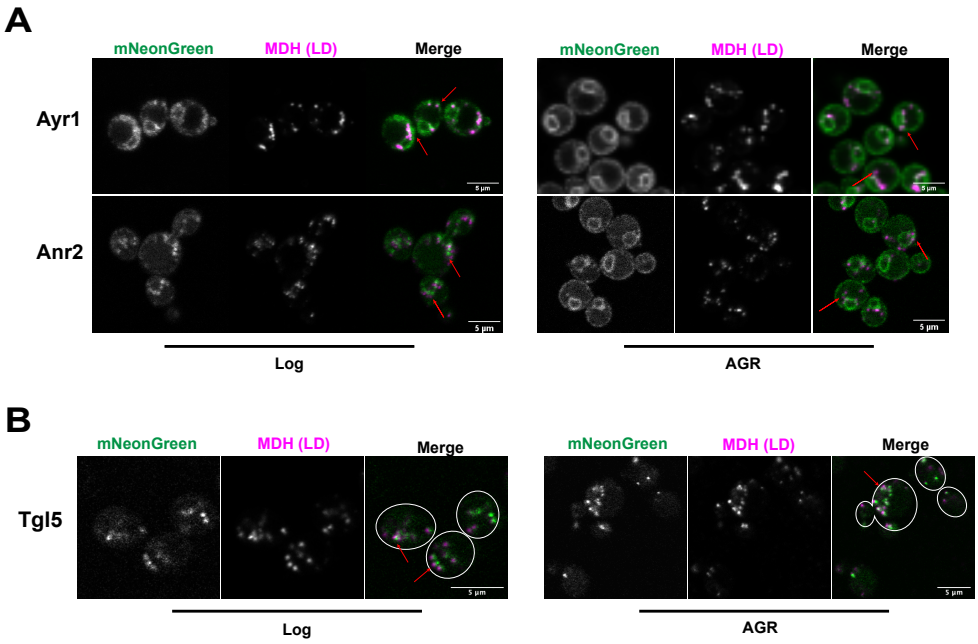


**Supplementary Figure 3.3. Selective delocalization of LD proteins during AGR stress.**

**A)** Yeast expressing mNg-tagged Ayr1 and Anr2 and stained with LD marker MDH in log-phase or 4hrs AGR conditions.

**B)** Yeast expressing Tgl5-mNg with MDH LD stain. Scale bars 5µm.

## Comparative proteomics reveals changes to the LD proteome in AGR stress

Since fluorescence imaging revealed that several LD proteins change sub-cellular distribution in AGR conditions, we next aimed to comprehensively map how AGR stress alters the LD proteome. We performed LC-MS/MS proteomics on LDs that were isolated from log-phase and 4hrs AGR-treated yeast using density gradient centrifugation (**Figure 3.4A**). To evaluate the quality of our LD isolation protocol, we performed Western blotting of whole-cell lysates and the subsequent LD isolation fractions. We found a clear de-enrichment of mitochondrial protein Por1 and the abundant plasma membrane protein Pma1 in the LD fractions, suggesting the LD fractions were relatively pure (**Figure 3.4B**).

Given that AGR stress likely changes the global abundance of some proteins, we also conducted LC-MS/MS proteomics on the non-LD infranatant fractions generated during LD isolation, as well as whole-cell lysates of yeast in log-phase or 4hrs AGR treatment. We

combined these datasets with our isolated LD proteomics to obtain a more robust dataset of high-confidence LD proteins in these conditions. This approach generated an adjusted LD enrichment score, defined as the "LD confidence score". This approach is based on previous work from (Bersuker et al., 2018), and accounts for the spectral abundance of each protein in the LD fraction, while subtracting out the corresponding abundance from the non-LD infranatant fraction. Plotting this LD confidence score as a function of protein whole-cell abundances thus clearly identified candidate proteins that enriched or de-enriched in AGR-associated LD fractions (**Figure 3.4C**).

As expected, this approach revealed that Erg6 was among the most de-enriched proteins in LD fractions at 4hrs AGR (**Figure 3.4C**, **left side of plot**), whereas Pln1 was one of the most enriched (**Figure 3.4C**, **right side of plot**). It also detected nearly all annotated LD proteins (Currie et al., 2014), although some of these displayed changes in abundance that appeared different from the localization patterns we observed by fluorescence microscopy (**Supplementary Figure 3.4A**). The reason for these distinctions likely reflects the differences between imaging and biochemical methodologies, may be also be due to the co-purification of ER membranes together with LDs during the LD isolation protocol.

Using this approach, our proteomics also revealed a subset of proteins that are not annotated to localize to LDs, but were nonetheless detected in high abundance in the isolated LD fractions during AGR stress. This included Iml2, which is required for the clearance of protein inclusions, and was previously observed associated with LDs bound to inclusion bodies in previous work (Moldavski et al., 2015) (**Figure 3.4C, right side of plot**). To investigate this, we mNg-tagged Iml2. While our imaging showed that Iml2-mNg was throughout cytoplasm in log-phase yeast, it subtly decorated the nuclear envelope and ER network at 4hrs AGR (**Supplementary Figure 3.4B**). Even though we did not visibly detect Iml2-mNg on LDs, this may be because LDs need to be associated with protein inclusions for Iml2 to visibly enrich on them by microscopy (Moldavski et al., 2015).

Our proteomics also indicated that two proteins containing Bin/Amphiphysin/Rvs (BAR) domains involved in Golgi/endosomal membrane trafficking, Snx4 and Gvp36, were enriched on LDs following 4hrs AGR (**Figure 3.4C)**. BAR domains are membrane binding modules,

and many BAR proteins contain amphipathic helices or other membrane inserting modules that could, in principle, insert into LDs. Furthermore, BAR protein GRAF1a was previously observed on LDs in human cells (Lucken-Ardjomande Häsler et al., 2014). Indeed, while Snx4-mNg formed cytoplasmic foci not colocalized with LDs in log-phase growth, Snx4-mNg foci did appear co-localized with a subset of LDs following 4hrs AGR (**Figure 3.4D**). In contrast, Gvp36-mNg distributed mostly throughout the cytoplasm in both log-phase and 4hr AGR stress, and was not detectably enriched on LDs by microscopy (**Supplementary Figure 3.4B**). Collectively, this indicates that AGR stress selectively remodels the LD proteome, and may lead to enhanced LD association of non-canonical factors or membrane trafficking components with the phospholipid surface of LDs.

**Global proteomics indicates AGR promotes metabolic remodeling and fatty acid oxidation**

Energy depletion drives metabolic remodeling in yeast, favoring the reorganization of organelles and the utilization of alternative carbon sources when glucose is restricted (Eisenberg and Büttner, 2014; Marini et al., 2020). Since we conducted whole-cell LC-MS/MS proteomics of log-phase and 4hrs AGR yeast, we next examined these datasets to determine whether changes in whole-cell protein abundances revealed patterns of metabolic remodeling that involved LDs and their lipids. Indeed, this indicated that 4hrs AGR stress induced changes to the abundances of many proteins involved in fatty acid metabolism. In particular, peroxisome enzymes involved in fatty acid oxidation (FAO), including Pot1, Fox2, and Cta1 were among the most increased in abundance during AGR compared to log-phase growth (**Figure 3.4E**). Also elevated were the peroxisome-associated fatty acyl-CoA ligase Faa2, the acetyl-CoA transporter Crc1 (which transports acetyl-CoA derived from peroxisome FAO to mitochondria), as well as Yat1, a carnitine acetyl-transferase that works with Crc1 to promote acetyl-CoA utilization within mitochondria. Enzymes related to the tricarboxylic acid cycle including Icl1 and Idp2, the malate synthase Mls1, and acetyl-CoA synthase Acs1 were also among the most elevated proteins in AGR-treated yeast. In contrast, amino acid transporters like Mup1 and Lyp1 were significantly decreased in abundance, consistent with their turnover

during glucose starvation that promotes metabolic remodeling (Lang et al., 2014; Wood et al., 2020).

Collectively, this indicates that glucose restriction promotes the mobilization of TGs from LDs that may provide fatty acids as fuel for cellular energetics in peroxisomes and mitochondria. An additional consequence of this Tgl-dependent TG mobilization is a shift in the neutral lipid ratios in LDs, ultimately giving rise to phase transitions within the LD core that drives SEs to transition into a liquid-crystalline phase.

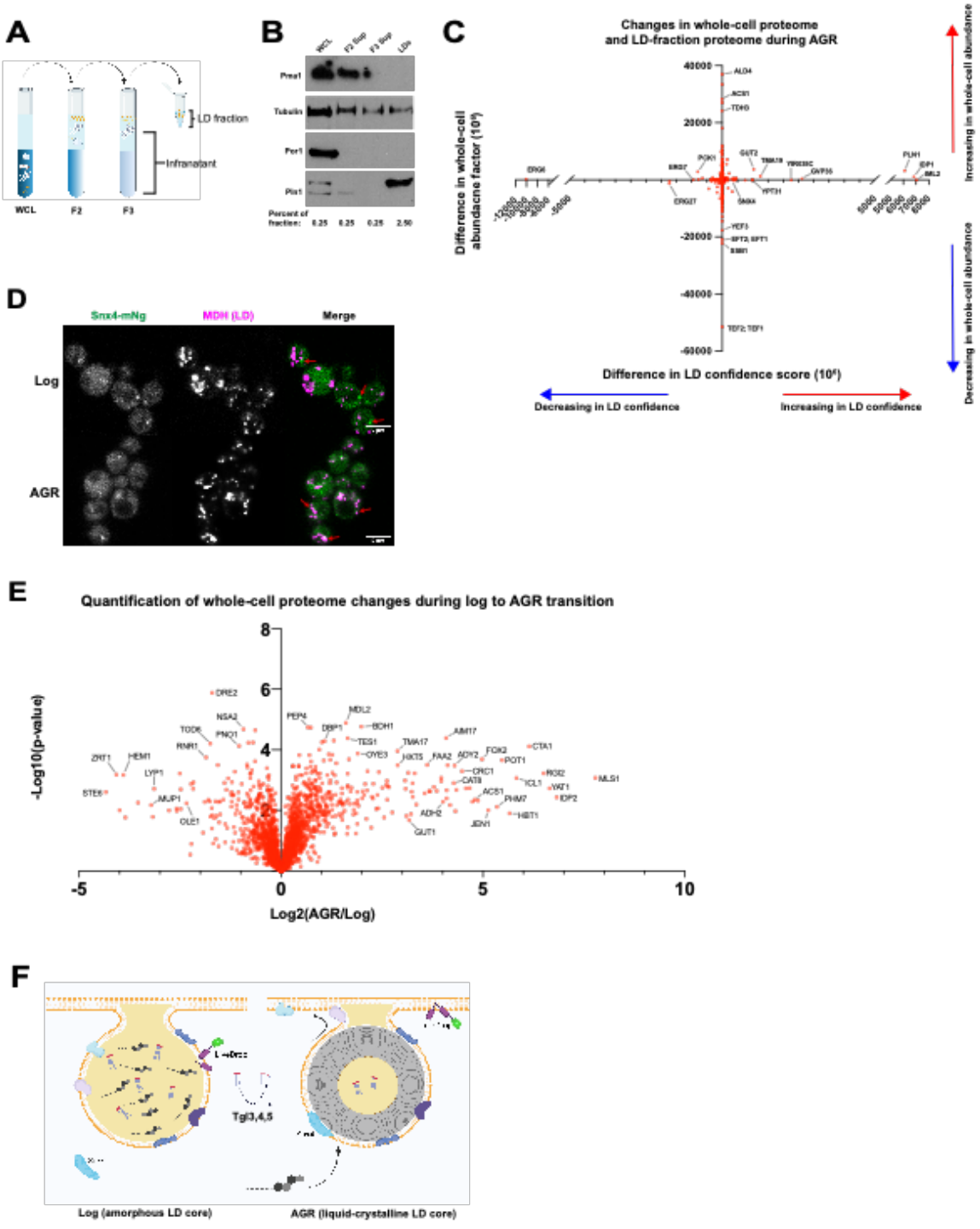


**Figure 3.4. Comparative proteomics indicates non-canonical protein association with LDs, and metabolic remodeling during AGR.**

**A)** Schematic of LD isolation protocol.

**B)** Western blot of whole cell lysate (WCL), and fractions of LD isolation protocol as in A. Pma1: plasma membrane marker, Por1: mitochondria marker. Pln1: LD marker. Tubulin: cytoplasmic marker

**C)** Plot of protein abundances in whole-cell proteomics (y-axis) versus their change in LD confidence score (see methods for description of this value) Data are average of 4 independent expts.
**D)** Micrographs of Snx4-mNg and LD/MDH stain in log and 4hrs AGR yeast with M1 coefficient of LD colocalization.
**E)** Volcano plot showing $\log_{10}$ p-value and $\log_2$ abundance changes in whole-cell abundance of proteins in 4hrs AGR treatment versus 2% glucose log-phase growth. Proteins on right are increased in whole-cell abundance with 4hrs AGR, those of left decreased in abundance. Data are average of 4 independent expts.
**F)** Model depicting TG lipolysis driven LCL-LD formation, and resulting changes in LD translocation to ER network targeting. Scale bars 5µm.

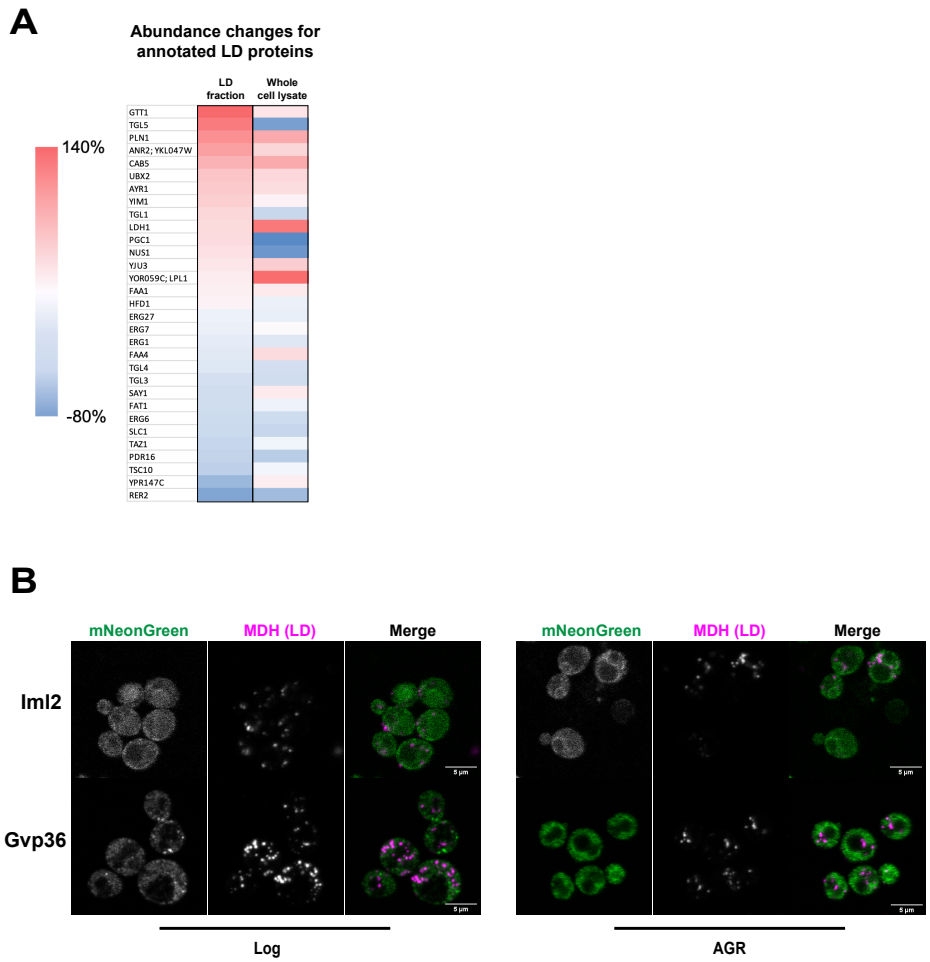


**Supplementary Figure 3.4. Additional LD proteins examined in log-phase and AGR conditions.**
**A)** Heat map depicting relative % changes in annotated LD proteins from log to 4hrs AGR conditions. Average of 4 independent log-phase and 4hrs AGR experiments.
**B)** Yeast with mNg-tagged Iml2 or Gvp36 and stained with MDH in log-phase and 4hrs AGR conditions. Scale bars 5µm.

## Discussion

Emerging evidence suggests the phase transition properties of cellular biomolecules, such as proteins in membraneless organelles, directly influence cell physiology and organization. Like proteins, lipids also undergo phase transitions, and can form liquid-crystalline lattices that are observed in human diseases like atherosclerosis, or in organelles like LDs. However, the metabolic cues that drive these phenomena, and their impact on organelle physiology, are unclear. Here we show that in yeast, AGR stress promotes the formation of liquid-crystalline lipid phase transitions within LDs. These transitions require TG lipolysis, suggesting the loss of TG within the hydrophobic core of LDs promotes the transition of SEs from an amorphous to a smectic liquid-crystalline phase. In agreement with this, we find AGR drives metabolic remodelling that elevates peroxisome-mediated lipid oxidation. Furthermore, we provide evidence that LCL-LD phase transitions alter the LD proteome (**Figure 3.4F**).

How proteins are targeted to LDs is still poorly understood, and involves trafficking from the ER network or cytoplasm to the LD surface. In this study, we revealed that the LD proteome dramatically differs between AGR-treatment and log-phase growth. Erg6, a canonical LD protein, relocalizes or is retained at the ER network, suggesting it moves from LDs to the ER via a lipidic bridge. This LD delocalization appears suppressed or quickly reversed when yeast cells are briefly heated to 40°C, i.e. above the predicted melting temperature of smectic-phase SEs, suggesting direct movement of the proteins between LD and ER via ER-LD bridges. In line with this, GFP-LiveDrop, which under log-phase conditions targets to both LDs and the ER, appears predominantly ER localized during AGR. Collectively, this suggests that Type I LD proteins favor ER localization versus the surface of LCL-LDs. This also indicates that many yeast LDs maintain connections to the ER network and thus exhibit lipidic bridges necessary for this inter-organelle trafficking, consistent with earlier work (Jacquier et al., 2011). The redistribution of LD proteins to the ER may be due to changes in LD monolayer fluidity with LCL-LD formation, which could alter the energetic favorability of proteins to remain on the LD surface. We also cannot rule out that the lipid composition of the ER network changes during AGR to a state that favors protein targeting or retention. We also find that artificially multimerizing Erg6 with a DsRed2 tag promotes its LD retention at AGR, implying

protein oligomerization enhances LD residency, as has previously been observed for perilipins (Giménez-Andrés et al., 2021).

Whereas Erg6 delocalized from LDs during AGR, TG lipases Tgl3,4,5 remained LD bound. Although the LD anchoring mechanisms for Tgl lipases are not fully understood, this implies that LDs continue to mobilize TG during AGR, gradually altering the TG:SE neutral lipid ratio. Indeed, AGR-treated yeast contain less TGs, consistent with lipolysis that provides fatty acids to fuel metabolic energetics. Fatty acids derived from these TGs are likely substrates for peroxisome FAO, of which several key enzymes are elevated during AGR stress. The acetyl-CoA produced from this FAO could also fuel mitochondrial energetic pathways, several proteins of which are also elevated by proteomics. LCL-LDs also exhibited de-targeting of enzymes like Hfd1, Rer2, and Say1. It is possible these enzymes' re-distributions influences their activities, and therefore promote metabolic remodeling. Indeed, several Erg pathway enzymes also appeared de-enriched from LDs during AGR by proteomics, and Erg1 is more active at the ER than on LDs (Leber et al., 1998).

Our proteomic and imaging analysis also revealed that LDs may become decorated with non-LD proteins during AGR stress. This included the BAR domain protein Snx4, which co-localized with some LDs only during AGR stress. As BAR proteins contain membrane binding/inserting modules, it is possible that Snx4 associates with LDs during AGR by inserting into its monolayer surface. Since the LD surface is normally densely coated with proteins, it is also possible Snx4 and other proteins may associate with the LD surface as it is uncoated of canonical LD proteins during AGR stress. Proteomics also detected Iml2 on LDs during AGR. Previous work proposed that Iml2 associated with LDs, and promoted the delivery of sterols to protein inclusions during their clearance in an unknown mechanism involving LDs (Moldavski et al., 2015). Although unclear, it is possible Iml2 may influence sterol metabolism on LCL-LDs.

This study is a significant step toward enhancing understanding how lipid phase transitions influence LD and organelle protein composition and ultimately function. Future studies will interrogate whether such changes in the LD proteome reflect metabolic remodeling that ultimately enable yeast to adapt to glucose shortage.

# CHAPTER FOUR

## Analysis of Neutral Lipid Synthesis in *Saccharomyces cerevisiae* by Metabolic Labeling and Thin Layer Chromatography


### Abstract

Neutral lipids (NLs) are a class of hydrophobic, chargeless biomolecules that play key roles in energy and lipid homeostasis. NLs are synthesized de novo from acetyl-CoA and are primarily present in eukaryotes in the form of triglycerides (TGs) and sterol-esters (SEs). The enzymes responsible for the synthesis of NLs are highly conserved from *Saccharomyces cerevisiae* (yeast) to humans, making yeast a useful model organism to dissect the function and regulation of NL metabolism enzymes. While much is known about how acetyl-CoA is converted into a diverse set of NL species, mechanisms for regulating NL metabolism enzymes, and how mis-regulation can contribute to cellular pathologies, are still being discovered. Numerous methods for the isolation and characterization of NL species have been developed and used over decades of research; however, a quantitative and simple protocol for the comprehensive characterization of major NL species has not been discussed. Here, a simple and adaptable method to quantify the de novo synthesis of major NL species in yeast is presented. We apply $^{14}$C-acetic acid metabolic labeling coupled with thin layer chromatography to separate and quantify a diverse range of physiologically important NLs. Additionally, this method can be easily applied to study in vivo reaction rates of NL enzymes or degradation of NL species over time.


### Introduction

Acetyl-CoA is the fundamental building block of diverse biomolecules including neutral lipids (NLs), which serve as a versatile biomolecular currency for building membranes, generating ATP, and regulating cell signaling (Arrese et al., 2014; Konige et al., 2014). The availability of NLs to be shunted into any of these respective pathways is, in part, regulated by their storage. Lipid droplets (LDs), cytoplasmic organelles composed of hydrophobic cores of triglycerides

(TGs) and sterol-esters (SEs), are the main storage compartments of most cellular NLs. As such, LDs sequester and regulate NLs, which can be degraded and subsequently utilized for biochemical and metabolic processes (Olzmann and Carvalho, 2019; Walther et al., 2017). It is known that the mis-regulation of NL and LD-associated proteins is correlated with the onset of pathologies including lipodystrophy and metabolic syndromes (Krahmer et al., 2013; Ross, 1993). Because of this, current LD research is intensely focused on how NL synthesis is regulated spatially, temporally, and across distinct tissues of multi-cellular organisms. Due to the ubiquitous cellular roles for NLs, many enzymes responsible for the synthesis and regulation of NLs are conserved throughout eukaryotes (Zhang and Liu, 2017). Indeed, even some prokaryotes store NLs in LDs. Therefore, genetically tractable model organisms such as *Saccharomyces cerevisiae* (budding yeast) have been useful for the study of NL synthesis and regulation.

The separation and quantification of NLs from cell extracts can be accomplished in a myriad of ways, including gas chromatography-mass spectrometry (GC-MS), high-performance liquid chromatography (HPLC), and ultra-performance liquid chromatography-mass spectrometry (UPLC-MS) (Borrull et al., 2015; Knittelfelder et al., 2014; Kotapati and Bates, 2020). Perhaps the simplest method for separating NLs is via thin layer chromatography (TLC), which allows for subsequent densitometric quantification from a standard curve (Bui et al., 2018; Ruiz and Ochoa, 1997). Although TLC provides only a course-grained separation of NLs, it remains a powerful technique because it is inexpensive, and it allows for the rapid separation of NLs from several samples simultaneously. Two of the most considerable challenges facing the study of NLs via TLC are: 1) the broad range of cellular abundances of NL species and their intermediates, and 2) the range of hydrophilicity/hydrophobicity of lipid intermediates within NL synthesis pathways. Consequently, the quantification of NL species via TLC is typically restricted to the most abundant species; however, introduction of a $^{14}$C-acetic acid radiolabel can significantly enhance the detection of low abundance intermediates within NL pathways. Acetic acid is rapidly converted into acetyl-CoA by the acetyl-CoA synthetase ACS2 (Pronk et al., 1996), which makes $^{14}$C-acetic acid a suitable radiolabeling substrate in yeast (Buttke

and Pyle, 1982). Additionally, separation of both hydrophobic NLs and hydrophilic intermediates of NLs can be achieved by TLC through the use of multiple solvent systems (Touchstone, 1995). Here, a method is presented for the separation of NLs using $^{14}$C-acetic acid metabolic labeling in yeast. Lipids labeled during the pulse period are subsequently isolated by a well-established total lipid isolation protocol (Folch et al., 1957), followed by the separation of NL species by TLC. Developing of TLC plates by both autoradiography to visualize labeled lipids, and a chemical spray to visualize total lipids, permits for multiple methods of quantification. Individual lipid bands can also be easily extracted from the TLC plate using a razor blade, and scintillation counting can be used to quantify amount of radiolabeled material within the band.

**Protocol**

**1. Growth and labeling of yeast cells with $^{14}$C-acetic acid**

1.1. Inoculate a yeast culture by picking a colony from a plate and dispensing it into 20mL of synthetic complete (SC) media containing 2% dextrose (see **Recipe section** for the recipe of SC media). Incubate at 30 ˚C for overnight with shaking at 200 rpm.

NOTE: Growth condition, sample volume, and treatment will differ based on the lipid(s) of interest. Prior to running full experiments, optimal growth conditions and culture volumes should be empirically determined. This protocol discusses radiolabeling of yeast cultures grown to stationary phase, a growth phase when biomembrane and cell growth slows, and NL synthesis is very active.

1.2. Measure the $OD_{600}$ of the overnight culture using a spectrophotometer and dilute the yeast cell culture to a final $OD_{600}$ of 0.2 in 50 mL of fresh SC media containing 2% dextrose. Grow the cells for 24 h, or until they have reached the stationary phase (which is commonly defined by a flat lining of the cell doubling $OD_{600}$ measurement).

1.3. Before collecting the cells, make the quenching buffer (60% methanol; 10mM Tricine pH 7.0). Make two 20 mL aliquots of quenching buffer for each sample (i.e., 40 mL quenching buffer for each sample) and split evenly into two 50 mL conical tubes). Store the quenching buffer aliquots at -80 ˚C for future use.

1.4. Once the cultures have reached the desired OD or growth phase, collect the cells by centrifuging at 4,100 x *g* for 10 min. While samples are in the centrifuge, prepare radiolabeling media by adding [1-$^{14}$C] acetic acid sodium salt to dextrose-free SC media at a final concentration of 10 μCi/mL.

CAUTION: Proper personal protective equipment (PPE) should be worn all times when working with radioactive materials. Always follow local guidelines for the proper storage, usage, and disposal of radioactive materials.

NOTE: Both the concentration of $^{14}$C-acetic acid in the labeling media and the radiolabeling incubation time should be adjusted according to the metabolite(s) of interest. Here, a 20 min radiolabeling pulse incubation is used, which is sufficient to label NL species with a range of abundance.

1.5. Remove the supernatant from the pelleted cells, and wash cell the pellet once with 20 mL of dextrose-free SC media by resuspending the pellet with a pipette. Collect the cells again by centrifuging at 4,100 x *g* for 5 min.

1.6. Resuspend the cells in 1 mL of dextrose-free SC media, and transfer the cells to a labeled 2 mL microcentrifuge tube. Collect the cells again by centrifuging at 4,100 x *g* for 2 min.

1.7. Resuspend the cells once more in 500 μL of dextrose-free SC media. Pre-cool a centrifuge equipped for 50 mL conical tubes to -10 ˚C or on the lowest temperature setting.

1.8. Begin the radiolabeling period by quickly adding 500 µL of radiolabeling media to each 500 µL of cell suspension (final $^{14}$C-acetic acid concentration = 5 µCi/mL). Incubate the tubes in a rotating incubator at 30 ˚C for 20 min. 2 min before the end of the labeling period, transfer one 20 mL aliquot of quenching buffer for each sample from the -80 ˚C freezer to a bucket of ice.

1.9. Once the radiolabeling period has ended, use a pipette to plunge the entire 1 mL sample into 20 mL of cold quenching buffer. Vortex the conical tubes for 5-10 s to ensure that the sample has been thoroughly mixed with the quenching buffer. Incubate the samples in quenching buffer for 2 min on ice.

1.10. Collect the cell pellet by spinning in a centrifuge at 5,000 x *g* for 3 min set to -10 ˚C or on the lowest temperature setting. While sample tubes are spinning, transfer another set of quenching buffer aliquot from the -80 ˚C freezer to a bucket filled with ice (i.e., one 20 mL tube of quenching buffer per sample).

1.11. Remove the quenching buffer supernatant from cell pellets and replace it with 20 mL fresh, cold, quenching buffer. Vortex and shake the samples until the pellet has been dislodged from the bottom of the conical tube and resuspended fully in quenching buffer. Centrifuge the samples again at 5,000 x *g* for 3 min at -10 ˚C to collect the cells.

1.12. Once the cells are pelleted, thoroughly remove all quenching buffer from the samples by pouring off the supernatant and removing the excess with a pipette. Store tubes at -80 ˚C for further processing.

**2. Isolation of total lipids from yeast**

NOTE: The following protocol for lipid isolation is based on a well-established and frequently used method that efficiently extracts most neutral lipid species (Folch et al., 1957)(Breil et al., 2017).

CAUTION: When using organic solvent, always wear appropriate PPE and work inside of a fume hood when possible. During lipid extraction, avoid using plastics that are incompatible with organic solvents. Polypropylene tubes are suitable for the following protocol.

2.1. Weigh 0.3 g of acid-washed glass beads for each sample and store them in 2 mL microcentrifuge tubes on ice. Remove the cell pellets from the -80 ˚C freezer and keep them on ice. Add 350 µL methanol and 700 µL chloroform to each sample, resuspend, and transfer to microcentrifuge tubes containing pre-weighed glass beads.

2.2. Lyse cells by agitating tubes on a vortex 3x for 1 min, with 30 s incubations on ice between agitations. Alternatively, cells can be lysed using a mini bead-beater for three 1-min cycles. Save 25-30 µL of whole cell lysate in a separate tube for scintillation counting.

NOTE: The saved lysate will be used to determine the relative amount of radioisotope taken up by each sample during the pulse period, which will influence the amount of each sample loaded onto the TLC plate. This is discussed further in step 3.2.

2.3. Pour the entire contents of the 2 mL microcentrifuge tube into a 15 mL glass centrifuge tube [Tube A]. Wash the 2 mL microcentrifuge tubes by adding 1 mL of methanol and vortexing for 10-15 s. Transfer the 1 mL methanol wash to tube A and add 2 mL of chloroform to tube A followed by 400 µL of water for a final sample volume of 4.45 mL.

2.4. Vortex samples for 1 min followed by a 5 min centrifugation at 1,000 x *g*. After centrifugation, the aqueous (upper) and organic (lower) phases should be clearly visually separated with cell debris lying at the interface.

2.5. Using a glass Pasteur pipette, collect the organic phase from tube A and move to a new 15 mL glass centrifuge tube (Tube B). Add 1 mL of 1M KCl to tube B. To tube A, add 1 mL of methanol and 2 mL of chloroform. Repeat the vortexing and centrifugation steps on tube A.

2.6. Once again collect the organic phase from tube A and add it to tube B. Dispose of tube A in an appropriate container. Vortex tube B for 1 min followed by a 5 min centrifugation at 1,000 x *g*.

2.7. Remove the upper aqueous layer from tube B and dispose. Add 1 mL of fresh 1 M KCl back to tube B and repeat the vortexing/centrifugation step. Once layers are separated, carefully collect the entire bottom organic layer into a labeled 4 mL glass vial.

NOTE: At this step, lipid extracts can be stored at -80 ˚C, or the protocol can be continued for TLC separation of lipids.

**3. Separation and quantification of radioisotope-labeled NLs by thin layer chromatography**

3.1. If lipid extracts were placed at -80 ˚C, slowly bring to room temperature by incubating on ice and subsequently on a benchtop. Completely evaporate solvent from lipid extracts by vacuum drying or using a gentle stream of inert gas (e.g., argon or nitrogen). Meanwhile, pre-heat an oven to 145 ˚C for heating the TLC plate.

3.2. Before samples can be loaded onto the TLC plate, determine relative amounts of radiolabel taken up by the cells. Pipette 10 µL of the whole cell lysate from step 2.2 into a 6 mL glass scintillation vial, add 6 mL of scintillation fluid and place vials in a rack. Use a scintillation counter to measure the cpm or dpm of each sample using the **count single rack** option set to a

1 min counting time. Measure each whole cell lysate in duplicate to obtain an average for each sample. Adjust the loading amount according to a wild type or reference sample

NOTE: The amount of each sample to load onto the TLC plate can be determined using the following equation: (average sample counts)/(average reference counts) x desired loading volume. For example, if 20 μL of the reference sample is to be loaded onto the TLC plate, and has an average count of 1,000, then an experimental sample with an average count of 2,000 will have 10 μL loaded onto the TLC plate.

3.3. Reconstitute the sample lipids in 40-50 μL of 1:1 (v/v%) chloroform:methanol by vortexing for 5 min. Prepare 101 mL of the mobile phase solvent in a glass graduated cylinder (see **Figure 4.1** for an example of major NL species separation by a 50:40:10:1 (v/v/v/v%) Hexane:Petroleum ether:Diethyl ether:Acetic acid solvent).

3.4. Pour the solvent into a glass TLC chamber containing a 20 x 20 TLC saturation pad and a tight-fitting lid. Prepare a channeled 20 x 20 silica gel 60 G plate by gently marking a line 1.5 cm above the bottom of the plate using a pencil. The line designates the origin and where the lipids will be loaded. Below the line, gently label the sample that will be loaded in each lane. Once the TLC plate has been prepped, incubate the plate in a 145 ˚C oven for at least 30 min to pre-heat the plate and remove any excess moisture.

3.5. Once the plate has been sufficiently heated, and the TLC saturation pad is saturated with solvent, remove the TLC plate from the oven and immediately proceed to loading the TLC plate. Loading the plate while it is warm ensures rapid solvent evaporation. For each lipid species of interest, load 5-20 μg of a purified lipid standard onto a lane of the TLC plate to track separation and expected migration distance. Using a pipette, spot 5μL of sample onto the origin of each lane located 1.5 cm above the bottom the of TLC plate. Repeat loading of 5 μL spots until 20-40 μL of sample has been loaded into each lane.

NOTE: 5-20 μg of unlabeled purified lipids can be added to each sample lane as tracers that can be stained and visualized following TLC separation of lipids. The presence of a stained standard allows for easy tracking and excision of radiolabeled lipid bands for subsequent scintillation counting. Which purified standards are loaded onto the plate will be determined by the NL species of interest. See **Figure 4.1** for examples of separating oleic acid (FFA), 1,2 dioleoyl-glycerol (DG), triolein (TG), cholesterol (Chol), cholesteryl-linoleate (SE), and squalene (SQ) in lanes adjacent to the sample lanes.

3.6. Once the standard and the experimental samples have been loaded, place the plate in the developing chamber and wait until the solvent has reached the top of the plate (40-60 min). Once the plate is fully developed, remove it from the chamber and allow it to dry in the fume hood for 20 minutes.

3.5 After the plate is dried, cover it with plastic film and place it in a developing cassette with an autoradiography screen. Allow the plate to develop with the screen for 24-48 h.

**4. Visualization and quantification of TLC separated lipids**

4.1. Remove the screen from the developing cassette and place inside of a phosphor imager. Select the **Phosphor Imaging** option and develop at 800-1000 V.

NOTE: Phosphor imaging gives a qualitative view of radiolabeled lipids on the TLC plate. However, quantification of radiolabeled lipids is best accomplished by scintillation counting, which is described subsequently.

4.2. Mix 100 mL of p-anisaldehyde reagent (see **Recipe section**) and deposit in a glass spray bottle. Spray the TLC plate with p-anisaldehyde reagent until the silica is saturated. Bake the plate in a 145 ˚C oven for 5 min, or until bands have appeared.

4.3. To quantify individual lipid species using radiolabel scintillation counting, use a razor blade to scrape the silica gel from the glass TLC plate. Transfer each silica gel band corresponding to a single radiolabeled lipid species to a glass scintillation vial and add 6 mL scintillation fluid. Vortex vigorously until the silica band has been reduced to small pieces.

4.3.1. Alternatively, lipids can be extracted from the silica gel band using the lipid extraction protocol in section 3. If lipids are extracted from the silica gel, evaporate the solvent entirely as in step 3.1, and add 6 mL scintillation fluid to the dried lipids. Place the rack containing scintillation vials into a scintillation counter. Select the **Count single rack** option and adjust the counting time to 2 min per vial. Results from the scintillation counter will be printed and can be visualized as a bar graph.

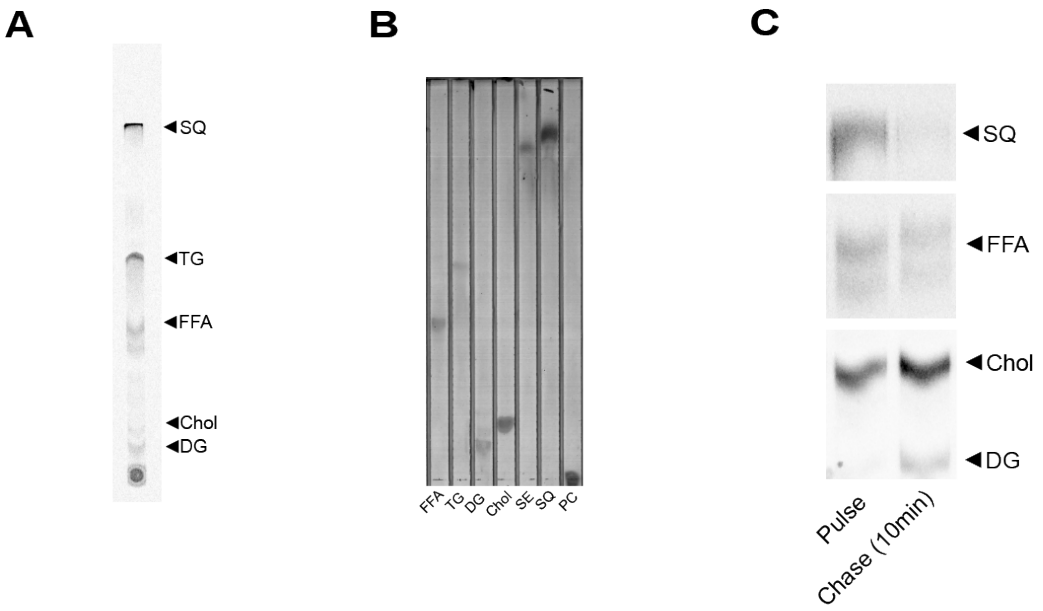


**Figure 4.1. $^{14}$C-Acetic acid radiolabeling allows for detection of multiple NL species**
**A)** Autoradiogram of lipids separated by TLC isolated from yeast radiolabeled with $^{14}$C-acetic acid in stationary phase. Clearly detectable species include free fatty acid (FFA), triglyceride (TG), diacylglycerol (DG), cholesterol (Chol), and squalene (SQ). Unlabeled bands are unidentified NL species.
**B)** Purified lipid species separated by TLC and visualized by p-anisaldehyde staining. Visualized species include all lipids mentioned in (A) in addition to sterol-esters (SE) and phosphatidylcholine (PC).
**C)** Autoradiogram of lipids separated by TLC isolated from yeast pulsed with $^{14}$-acetic acid in stationary phase followed by a 10 min chase period in radiolabel-free media. Disappearance of SQ is met with increase in Chol. Rise in DG in the chase period is accompanied by decrease in FFA species.

**Recipes**

**20% dextrose solution:**

For one liter of 20% dextrose: Dissolve 200g of dextrose in 600mL of MilliQ water. Once all the dextrose has dissolved, bring the solution up to 1000mL with MilliQ water and filter sterilize using a 0.45μm or 0.22μm membrane.

**Complete dropout powder mix:**

In a 500mL beaker, add together 1.25g adenine, 0.9g arginine, 3.0g aspartate, 3.0g glutamate, 0.9g lysine, 0.6g methionine, 1.5g phenylalanine, 11.25g serine, 6.0g threonine, 0.9g tyrosine, 4.5g valine, 1.2g alanine, 1.2g asparagine, 1.2g cysteine, 1.2g glutamine, 1.2g glycine, 1.2g isoleucine, 1.2g proline, 0.6g histidine, 1.8g leucine, 1.2g tryptophan, and 0.6g uracil. Once all powders have been deposited in the beaker, mix thoroughly with a spatula. In small increments, transfer portions of the mixed powder to a mortar, and gently crush with a pestle. Transfer the crushed powder to a new 500mL beaker. Once all powder has been crushed, mix again thoroughly and store in 50mL conical tubes at room temperature.

**Synthetic-Complete (SC) media:**

For one liter of SC media, dissolve the following in 600mL of MilliQ water: 10g succinic acid, 6g sodium hydroxide, 5g ammonium sulfate, 1.7g yeast nitrogen base without ammonium sulfate and amino acids, and 1.3g complete dropout powder mix (see recipe for details). Once all components are dissolved, bring the solution up to 900mL wilh MilliQ water and autoclave to sterilize. After the media has cooled, add 100mL of filter-sterilized 20% dextrose to the media (final dextrose concentration = 2%).

**p-anisaldehyde reagent:**

For 100mL of p-anisaldehyde spray reagent: Add 500μL of p-anisaldehyde to 10mL of glacial acetic acid. Once mixed, add 85mL of 200 proof absolute ethanol and 5mL of concentrated sulfuric acid.

**Discussion**

Here, a versatile radiolabeling protocol to quantitatively monitor the synthesis of NL species in yeast is presented. This protocol is very modular, which allows for the procedure to be finished within 3-6 days. Additionally, a wealth of literature exists on the use of TLC to separate lipid species and metabolites, which should permit the user to detect several lipid species of interest with a simple change of TLC solvent systems (Fuchs et al., 2011; Touchstone, 1995). This protocol is conducive to the separation, detection, and quantification of radiolabeled lipids. It can also be coupled with a chase period in un-labeled media to detect the turnover time of labeled NLs. Collectively, this procedure gives a useful structure to begin exploring the radiolabeling of NL species.

Other methods, such as HPLC, GC-MS, and UPLC-MS provide higher resolution of lipid separation and quantification; however, it is typically not optimal to run radiolabeled samples through MS, although this can be overcome by using stable-isotopes. Nevertheless, this radiolabel method provides high detection sensitivity and versatility for many lipid species. Another advantage of this protocol compared to MS is its affordability. TLC separation of lipids is relatively simple, requires no extravagant equipment, and relies on common laboratory materials. Regarding limitations: certain low-abundance species, like lyso-lipids, may not be detectable even following incorporation of a $^{14}C$ label. Additionally, most TLC approaches are not suitable for 'lipidomic' characterizations, due to the course-grained separation of lipid species within a given solvent.

Yeast offer a convenient, genetically tractable model system for the study of lipids via radiolabel biochemical approaches. However, it should be noted that in specific genetic backgrounds, or during a particular metabolic growth conditions, the cellular uptake of radiolabeled-acetic acid or other radiolabels may be reduced. Labeling of cells with $^{14}C$-acetic acid in the absence of glucose robustly increases the uptake of the radiolabel. Long incubations in the absence of glucose will proportionally increase radiolabel uptake; however, this may also influence the pathways in question. Therefore, labeling efficiency for a particular growth

condition should be established prior to following the $^{14}$C-acetic acid radiolabeling protocol in full. In particular, pay attention to the length of the radiolabeling period. The labeling time should be kept as short as possible to detect the lipid species-of-interest. Altogether, this procedure allows for the study of important lipid synthesis reactions and should permit the investigation of NL regulation in intact cells.

# CHAPTER FIVE

## Materials and Methods

### Strains, plasmids, and yeast growth conditions

W303 (leu2-3,112 trp1-1 can1-100 ura3-1 ade2-1 his3-11,15) was used as the wild type parental strain for all experiments and cloning in this study. All strains used in these studies can be found in Appendix A-Supplementary Table 1. Deletion of endogenous genes, C-terminal tagging at endogenous loci, and transformation of plasmids was accomplished by the traditional lithium acetate method. Endogenous knockins and knockouts were validated by genomic PCR, and plasmids were validated by sequencing. Plasmids generated for this study were created using RepliQa HiFi assembly (Quantabio cat. 95190) following the manufacturer's protocol. For cloning into pRS305 plasmids, destination vectors were cut with XhoI and SacI enzymes, while linearization of pFa6a plasmids was accomplished by digestion with AscI and PacI enzymes. Synthetic complete media supplemented with amino acids was used for all experiments, except where leucine or uracil was omitted from the media to accommodate growth of strains carrying pRS305 or pBP73G plasmids, respectively. All yeast were grown in 30C incubators shaking at 210RPM. Log phase yeast were grown to an $OD_{600}$ of 0.5 in the presence of 2% dextrose. AGR-treated yeast were grown to $OD_{600}$ of 0.5 in the presence of 2% dextrose, collected, washed with dextrose-free media, and resuspended in media containing 0.001% dextrose for the indicated time period. Where indicated, Terbinafine (Sigma T8826), Lovastatin (Sigma 1370600), Cycloheximide (Sigma C7698), MG132 (Sigma M7449), or oleic acid were added to the media at the beginning of AGR treatment to final concentrations of 10μg/mL, 20μg/mL, 100μg/mL, and 25μM, and 0.1%, respectively.

### Fluorescence microscopy

For confocal microscopy, cells were grown as described above, collected by centrifugation at 3,000xg for two minutes, and resuspended in glucose-free media at approximately one one-hundredth of original volume. All images were taken as single slices at approximately mid-

plane using a Zeiss LSM880 inverted laser scanning confocal microscope equipped with Zen software. Images were taken with a 63x oil objective NA=1.4 at room temperature. Prior to imaging, cells were incubated for three hours with 0.5μg/mL FM4-64 dye (Invitrogen T13320) to visualize vacuoles.

For epifluorescence microscopy, cells were grown, stained, and collected as described above. Vacuoles were also stained with 5μg/mL CMAC (ThermoFisher C2110) dye for two hours prior to imaging, where indicated. Imaging was performed on an EVOS FL Cell Imaging System at room temperature.

Hmg1 NVJ partitioning was quantified using Fiji software. For quantification, RGB images were converted to 16-bit and a background subtraction was performed by subtracting original images by a duplicate 'Gaussian blur' filtered image (sigma (radius)=5.0). Five-pixel line scans were taken across the nuclear envelope toward the NVJ, and the 'plot profile' function was used in Fiji to produce a fluorescence histogram of nuclear envelope signal. The sum area under each curve was calculated and plotted as the ratio of fluorescence intensity of NVJ-associated signal by fluorescence intensity of Non-NVJ associated NE signal.

For Mander's colocalization quantification, confocal microscopy images were split into respective channels and analyzed using the JACoP plugin (Bolte and Cordelières, 2006). M1 and M2 coefficient analysis was used with automatic thresholding. Relative M1 values were calculated with the average of log-phase M1 values as the reference.

**FRAP and FLIP analysis**

Yeast used for FRAP and FLIP were grown and collected as described above, and imaging was conducted for one hour after collection. Photobleaching movies were taken on an Andor spinning disk confocal microscope through a 63x oil objective (NA=1.4). The microscope is equipped with an Andor Ultra EMCCD and Metamorph software. For FRAP measurements, a single circular ROI of 0.77$\mu m^2$ that corresponds to the NVJ was selected and bleached with a 408nm laser at 100% power and 100ms dwell time. One image was taken before the bleach, and subsequent images were taken every 500ms for a total movie length of 25 seconds. For FLIP measurements, single circular ROIs of 0.77$\mu m^2$ were selected, taking care to select an

area of the NE that was furthest from the NVJ. Each bleaching cycle consisted of a pre-bleach image, a single bleach with a 408nm laser with a 100ms dwell time, and four post-bleach images taken 500ms apart. Each movie captured a total of 50 bleach cycles, which corresponds to 300 second movies. Fiji software was used to quantify bleaching curves and halftimes. Pre-processing of images included background subtraction as described above and 3D Gaussian smoothing (sigma=0.5). FRAP quantification was performed using the double normalization method as previously described (Phair and Misteli, 2000). Briefly, intensity was measured for all time points in an ROI corresponding to the bleached region ($I_{frap}$) and an ROI corresponding to the whole cell ($I_{whole\text{-}cell}$), and normalized intensities were generated for each timepoint ($I_{normalized}(t)$) using equation S1:

$$I_{normalized}(t) = \frac{I_{whole-cell-pre}}{I_{whole-cell}(t)} * \frac{I_{frap}(t)}{I_{frap-pre}} \quad \text{(Eq S1)}$$

In the equation above, the 'pre' subtext indicates the timepoint preceding ROI bleaching. Intensity recovery curves were created for each movie by further normalizing values such that pre-bleach intensities were set to 1 and post-bleach intensity of an ROI was set to 0. Full normalization was accomplished using equation S2 followed by subtracting the normalized $I_{frap\text{-}bleach}$ value from all timepoints.

$$I_{normalized-full}(t) = \frac{I_{normalized}(t)}{I_{frap-pre} - I_{frap-bleach}} \quad \text{(Eq S2)}$$

In equation S2, $I_{frap\text{-}bleach}$ indicates the intensity of the photobleached ROI at the time of photobleaching. Halftimes were calculated from individual fluorescence recovery curves using Graphpad Prism 8 software and fitting the data to a one-phase exponential association. Pre-processing for FLIP images was the same as for FRAP images. FLIP movies were quantified using Fiji to monitor the intensity of NVJ-associated signal over time. Intensity measurements were normalized using equation S3.

$$I_{FLIP}(t) = \frac{I_{NVJ}(t)}{I_{NVJ-pre-bleach}} \quad \text{(Eq S3)}$$

In equation S3, $I_{FLIP}(t)$ is the relative fluorescence at the NVJ at time t, $I_{NVJ}(t)$ is the raw intensity value at the NVJ at time t, and $I_{NVJ\text{-}pre\text{-}bleach}$ is the intensity at the NVJ before bleaching occurred. Halftimes were calculated from FLIP decay curves, which were generated in Graphpad Prism 8 software by fitting the data to a one-phase exponential decay.

**Lipid extraction and thin layer chromatography – steady state lipid analyses**

For lipid extraction, approximately 50OD units of cells were collected for each sample, and pellet wet weight was normalized and noted prior to extraction. Lipid extraction was performed using a modified Folch method (Folch et al., 1957). Briefly, cell pellets were resuspended in MilliQ water with glass beads and lysed by three one-minute cycles on a bead beater. Chloroform and methanol were added to the lysate to achieve a 2:1:1 chloroform:methanol:water ratio. Samples were vortexed, centrifuged to separate the organic and aqueous phases, and the organic phase was collected. Extraction was repeated a total of three times. Prior to thin layer chromatography, lipid samples were dried under a stream of argon gas and resuspended in 1:1 chloroform:methanol to a final concentration corresponding to 4μL of solvent per 1mg cell pellet wet weight. Isolated lipids were spotted onto heated glass-backed silica gel 60 plates (Millipore Sigma 1057210001), and neutral lipids were separated in a mobile phase of 80:20:1 hexane:diethyl ether:glacial acetic acid. TLC bands were visualized by spraying dried plates with cupric acetate in 8% phosphoric acid and baking at 140°C for an hour. To quantify TLC bands, all plates were run with an internal neutral lipid standard. Densitometry of bands was performed in Fiji.

**Batch culture growth curves**

Cells were treated with AGR for ten hours, as described above. Some samples were also co-treated with 10μg/mL mevalonate (Sigma 50838) at the beginning of AGR treatment. After a ten hour treatment with AGR, cultures were diluted to an $OD_{600}$ of 0.1 in SC media containing 2% glucose. The $OD_{600}$ of cultures was measured each hour and plotted in Prism 8 software.

**Single cell time-lapse microscopy**

Cells were imaged using a Zeiss Observer Z1 microscope equipped with automated hardware focus, motorized stage, temperature control, a Zeiss EC Plan-Apochromat 63X 1.4 or 40X 1.3 oil immersion objectives, and an AxioCam HRm Rev 3 camera. Exposure times for experiments shown in Supp Fig 2.5B: Phase contrast 20ms, Whi5-mKoκ 150 ms, Erg6-mTFP1

20 ms, Vma1-mNeptune2.5 75ms, Nvj1-mRuby3 75ms, Msn2-mNeonGreen 40ms. Exposure times for experiments shown in Fig 2.7 and Supp Fig 2.7: Phase contrast: 40 ms, Hmg1-mRuby3 or Hmg1-DsRed2: 100 ms.

All experiments were performed with a Y04C Cellasic microfluidic device (http://www.cellasic.com/) using 1 psi flow rate. Images are taken every 6 minutes. Prior to loading into the microfluidics chamber, cells were sonicated and mixed with 50μL SCD media to achieve an $OD_{600}$ of approximately 0.1. In the chamber, cells are first grown for 2hrs in SCD. Next, they are exposed to acute glucose restriction (AGR) by switching to SC for 10 hrs which is followed by glucose replenishment by 4 hrs SCD. To determine time of growth resumption, cells are segmented and tracked as described previously (Doncic et al., 2013; Wood and Doncic, 2019). Next, the time of resumption is annotated semi-automatically using a custom MATLAB software by determining the time of bud growth or new bud emergence during the four-hour glucose replenishment following AGR.

**Lipid droplet isolation by density centrifugation**

Procedure for the isolation of lipid droplets was adapted from previous methods (Mannik et al., 2014). Specifically, approximately 600OD units of cells was grown to appropriate growth phase in SCD media. Cells were collected by centrifugation at 4,100xg for 10 minutes at room temperature and resuspended in reducing buffer (10mM Tris-HCl pH 9.4, 10mM DTT) to a final concentration of 100OD/mL. After a five minute incubation at room temperature, cells were pelleted again by centrifugation at 4,100xg for 5 minutes. Reducing buffer was removed and replaced with equal volume spheroplasting buffer (10mM Tris-HCl pH 7.4, 700mM sorbitol, 7.5 g/L yeast extract, 15g/L peptone, 1mM DTT). Spheroplasting was initiated by addition of zymolyase 20T (120491-1, AMSBIO) to a final concentration of 1mg/100OD cell units. For log-phase cells, spheroplasting buffer was supplemented with glucose to a final concentration of 0.5% (w/v), while AGR-treated cells were spheroplasted in the absence of glucose. Cells were incubated in spheroplasting buffer for 40 minutes in a 30°C incubator shaking at 130RPM. Once spheroplasting was complete, cells were pelleted by centrifugation at 4,100xg for 5 minutes at 4°C. Spheroplasting buffer was thoroughly removed and cells were

gently resuspended in cold lysis buffer using a cut pipette tip (10mM Tris-HCl pH 7.4, 12% ficoll, 200μM EDTA, 1x protease/phosphatase inhibitor cocktail (78444, ThermoFisher), 50μM Mg132, 1mM DTT) to a final concentration of 500OD/mL. Spheroplasts were once again pelleted by centrifugation at 4,100xg for 5 minutes at 4°C and resuspended in cold lysis buffer to a final concentration of 1000OD/mL and stored at -80°C. For cell lysis, spheroplasts were thawed on ice and diluted to a concentration of 500OD/mL using cold lysis buffer. Spheroplasts were transferred to a chilled glass dounce homogenizer and lysed by 25 strokes of a loose-fitting pestle. Resulting lysate was loaded into a 11x60mm ultracentrifuge tube (344062, Beckman), overlayed with equivalent volume of lysis buffer, and centrifuged in a SW60Ti rotor at 100,000xg for 1.5 hours at 4°C set to accel=max and decel=none. Float fractions were collected using a cut P200 pipette tip and loaded into a new 11x60 ultracentrifuge tube. The bottom fraction volume was adjusted to approximately 1.5mL using cold lysis buffer and was overlayed with overlay buffer #1 (10mM Tris-HCl pH 7.4, 8% ficoll, 200μM EDTA, 1x protease/phosphatase inhibitor cocktail, 50μM Mg132, 1mM DTT). Centrifugation was repeated for 1 hour under the same settings listed above. The second float fraction was collected and transferred to a new 11x60 ultracentrifuge tube. The volume was adjusted to 1.5mL with overlay buffer #1 and supplemented with sorbitol to a final concentration of 600mM. Fractions were then overlayed with overlay buffer #2 (10mM Tris-HCl pH 7.4, 250mM sorbitol, 200μM EDTA, 1x protease/phosphatase inhibitor cocktail, 50μM Mg132, 1mM DTT) and centrifugation step was repeated for one hour. The final float fraction was collected, transferred to a 1.5mL microcentrifuge tube, and concentrated by removing the bottom infranatants following repetitive centrifugations at 20,000xg in a 4°C microcentrifuge. LD fractions were concentrated to approximately 200μL and stored at -80°C along with corresponding infranatant fractions.

**Protein extractions**

***Protein extraction for Hmg1 protein analysis***

Approximately 50OD units of cells were collected for protein extraction. Prior to protein extraction, cell pellet wet weights were normalized. Protein extraction was accomplished by

precipitating proteins with 20% TCA for thirty minutes on ice, followed by three washes of the pellet with cold 100% acetone. The protein pellet was dried for fifteen minutes in a speed-vac to remove residual acetone, and all pellets were resuspended in 2x SDS sample buffer (65.8mM Tris-HCl, pH 6.8; 2% SDS; 25% glycerol; 10% 2-mercaptoethanol; 0.01% bromophenol blue). Resuspended protein samples were heated at 70°C for ten minutes prior to being loaded onto a gel.

***Native protein isolation for blue-native PAGE***

Approximately 100OD units of cells were collected for BN-PAGE analysis. Cell pellets were collected into 2mL screw-cap tubes and frozen at -80°C until further processing. For cell lysis, one large scoop of glass beads and 300µL of lysis buffer was added to each tube (50mM HEPES-NaOH, pH 7.0; 50mM NaCl; 250mM sorbitol; 10% glycerol; 20mM arginine; 20mM glutamic acid; 1.5mM $MgCl_2$; 1.0mM $CaCl_2$; 1mM EDTA; 1mM DTT; 50µM Mg132; 1x protease/phosphatase inhibitor cocktail (ThermoFisher cat. 78429)). Tubes containing frozen cell pellet, glass beads and lysis buffer were agitated for one minute using a bead beater followed by two minutes on ice and another minute of agitation with a bead beater. After glass bead lysis, another 700µL of lysis buffer was added to each tube followed by a brief mixing via vortex. Cell debris was cleared by a 5 minute 1,000xg spin at 4°C. Supernatants were transferred to a new 1.5mL tube and centrifuged again at 21,000xg for 30 minutes at 4°C to isolate a crude microsomal fraction. The supernatants from the first spin were discarded and crude microsomes were washed with 1000µL of cold lysis buffer followed by another spin at 21,000xg for 30 minutes at 4°C. Supernatants were again discarded and crude microsomes were resuspended in 60µL of lysis buffer containing digitonin at a final concentration of 1.5%. Tubes were kept on ice for 30 minutes and gentle pipetting was applied every ten minutes to aid in solubilization of the microsomes. To clear insoluble materials, tubes were centrifuged at 100,000xg for 30 minutes at 4°C in a Beckman TLA-55 fixed angle rotor. Supernatants were transferred to new tubes on ice after the clearance spin. Approximately 30µL was reserved for BN-PAGE and 20uL for SDS-PAGE. The remaining 10µL was used to quantify protein concentrations in duplicate with the Pierce detergent compatible Bradford kit (ThermoFisher cat. 23246). For SDS-PAGE samples, 4x NuPAGE LDS sample buffer (cat. NP0007) was

added to each sample for a final concentration of 1x. Each sample was supplemented with 2-mercaptoethanol and urea at final concentrations of 5% and 8M, respectively. SDS-PAGE samples were heated at 37°C for 40 minutes and loaded onto homemade 4-15% polyacrylamide gels. SDS-PAGE and immunoblotting was performed as described below.

***Lipid droplet fraction de-lipidation and protein extraction***

LD fractions were mixed with 1mL of -20°C 100% acetone and stored at -80°C overnight to precipitate proteins. After overnight incubation, tubes were centrifuged at 20,000xg for 10 minutes at 4°C to pellet the proteins. The supernatant was removed and the protein pellet was subjected to three washes, each followed by the same centrifugation step listed above. The washes were performed with -20°C 100% acetone, 4°C 1:1 acetone:diethyl ether, and room temperature 100% diethyl ether. After the final wash, the supernatant was removed and the protein pellet was dried in a room temperature speed vac for 15 minutes. The resultant dried pellet was resuspended in 100µL of resuspension buffer (2x NuPAGE LDS sample buffer (NP0008, ThermoFisher), 10% beta-mercaptoethanol, 8M urea). Samples were heated at 37°C for two hours accompanied by gentle mixing with a pipette prior to being subjected to SDS-PAGE.

***Whole-cell and infranatant protein extractions from LD isolations***

Whole cell protein extracts were isolated from 50OD units of cells. Frozen cell pellets stored at -80°C were incubated with 20% trichloroacetic acid for 30 minutes on ice with occasional mixing using a vortex. Precipitated proteins were pelleted in a 4°C centrifuge at 15,000xg for 5 minutes. After removing the supernatant, the pellet was washed three times with cold 100% acetone followed by brief sonication. After the washes, protein pellets were dried in a room temperature speed vac for fifteen minutes to remove residual acetone. For infranatant fraction analysis, 2mL of each infranatant was reserved after LD isolation and stored at -80°C. TCA was added to each infranatant fraction to a final concentration of 20%. From this point, proteins were extracted as indicated above for whole-cell lysates. Dried protein pellets from whole-cell lysates and infranatant fractions were resuspended in 200µL of resuspension buffer and heated as indicated above for LD fractions.

**Immunoblot analysis**

Unless otherwise indicated, proteins were separated on a homemade 4-15% gradient gel in TGS running buffer. Proteins were transferred to a 0.45μm nitrocellulose membrane in Towbin SDS transfer buffer using a Criterion tank blotter with plate electrodes (BioRad 1704070). Immediately following transfer, membranes were stained with PonceauS and cut using a clean razor blade. Membranes were blocked with 5% milk dissolved in TBS-T buffer, and primary antibodies were allowed to bind overnight at 4°C. Primary antibodies used for determining Hmg1 protein expression are as follows: GFP (Abcam ab290; 1:10,000 dilution), mRuby3 (Invitrogen R10367; 1:1,000 dilution), and DsRed2 (OriGene TA180005; 1:1,000 dilution). Primary antibodies used to monitor protein expressions from LD isolations were: Pma1 (Abcam ab4645; 1:1,000 dilution), Porin (ThermoFisher CAT 459500; 1:1,000 dilution), and Pet10/Pln1 (Joel Goodman's lab, 1:1,000). Rat monoclonal antibody to tubulin (Abcam ab6160; 1:10,000 dilution) and rabbit polyclonal antibody to Sec61 (Jonathan Friedman lab; 1:5,000 dilution) were used as loading controls. Immunoblots were developed by binding HRP-conjugated anti-rabbit IgG (Sigma A0545; 1:10,000), anti-rat IgG (Abcam ab97057; 1:10,000), or anti-mouse IgG (Abcam ab6728; 1:2,000) secondary antibodies to the membrane for one hour in the presence of 5% milk followed by three washes in TBS-T and developing with ECL substrate (BioRad cat. 1705061). Signal was captured by x-ray film.

**Blue native PAGE and immunoblotting from native protein extracts**

Prior to BN-PAGE, 3.3μL of BN-PAGE loading buffer was added to each sample (100mM Bis-Tris, pH 7.0; 500mM 6-aminocaprioc acid; 5% Coomassie G-250) and gentle mixing was applied via vortex. Samples were loaded onto NativePAGE 3-12% Bis-Tris gels (ThermoFisher cat. BN1001BOX) alongside a NativeMark unstained protein standard (ThermoFisher cat. LC0725). Separation was performed in a mini gel tank (ThermoFisher cat. A25977) with 1x NativePAGE running buffer (ThermoFisher cat. BN2001) in the anode and 1x NativePAGE running buffer containing 1x cathode buffer additive (ThermoFisher cat. BN2002) in the cathode. Electrophoresis was performed at 150V for 30 minutes, after which cathode buffer was replaced with 1x NativePAGE running buffer containing 0.1x cathode

buffer additive and ran at 150V for another 30 minutes. After one hour at 150V, voltage was increased to 300V until the dye front was at the bottom of the gel. Once gel case was removed, the wells and dye front were excised and discarded from the gel with a clean razor blade. The ladder was excised and stained separately in GelCode blue stain (ThermoFisher cat. 24594) according to the manufacturer's instructions. The remaining gel was incubated in denaturing buffer (300mM Tris; 100mM acetic acid; 1% SDS) for 20 minutes on a rocker, after which, the gel was placed between two glass plates wetted with denaturing buffer and incubated for one hour. Proteins were transferred to a 0.2μm PVDF membrane overnight by wet transfer at 25V in a cold room with BN-PAGE transfer buffer (150mM Tris; 50mM acetic acid). After overnight transfer, the membrane was incubated in 8% acetic acid for five minutes followed by a five minute incubation in MiilliQ water. The membrane was dried for one hour at room temperature and then washed quickly four times with 100% methanol followed by a quick wash with MilliQ water. The membrane was then placed in 5% milk for one hour, and subsequent steps for immunoblotting were performed as described above. For detection of Hmg1-3HA, an anti-HA primary antibody was used (Abcam ab9110; 1:2,000 dilution) followed by rabbit secondary described above.

**Sample preparation and LC-MS/MS proteomics**

Protein samples were isolated and heated as described in the 'protein extraction' sections. Samples were centrifuged at 20,000xg for 5 minutes to remove insoluble materials and the 40μL of each supernatant was loaded onto a 10% mini-protean TGX gel (4561033, Bio-Rad). Samples were subjected to electrophoresis at 130V constant until the dye front was approximately 10cm into the gel. The gel was subsequently removed from the casing and stained with Coomassie reagent (0.5 Coomassie G-250, 50% methanol, 10% acetic acid) for one hour on a room temperature rocker. The gel was then subjected to destaining (40% methanol 10% acetic acid) for two hours. Once the gel was sufficiently destained, 10cm gel bands were excised from each lane, taking care to exclude the stacking gel and dye front. Gel bands were further cut into 1cm squares and placed into microcentrifuge tubes. Samples were digested overnight with trypsin (Pierce) following reduction and alkylation with DTT and

iodoacetamide (Sigma–Aldrich). The samples then underwent solid-phase extraction cleanup with an Oasis HLB plate (Waters) and the resulting samples were injected onto an Orbitrap Fusion Lumos mass spectrometer coupled to an Ultimate 3000 RSLC-Nano liquid chromatography system. Samples were injected onto a 75 μm i.d., 75-cm long EasySpray column (Thermo) and eluted with a gradient from 0-28% buffer B over 90 min. Buffer A contained 2% (v/v) ACN and 0.1% formic acid in water, and buffer B contained 80% (v/v) ACN, 10% (v/v) trifluoroethanol, and 0.1% formic acid in water. The mass spectrometer operated in positive ion mode with a source voltage of 1.5-2.0 kV and an ion transfer tube temperature of 275°C. MS scans were acquired at 120,000 resolution in the Orbitrap and up to 10 MS/MS spectra were obtained in the ion trap for each full spectrum acquired using higher-energy collisional dissociation (HCD) for ions with charges 2-7. Dynamic exclusion was set for 25 s after an ion was selected for fragmentation. Raw MS data files were analyzed using Proteome Discoverer v 2.4 (Thermo), with peptide identification performed using Sequest HT searching against the *S. cerevisiae* protein database from UniProt. Fragment and precursor tolerances of 10 ppm and 0.6 Da were specified, and three missed cleavages were allowed. Carbamidomethylation of Cys was set as a fixed modification, with oxidation of Met set as a variable modification. The false-discovery rate (FDR) cutoff was 1% for all peptides.

**Proteomics quantification**

Proteomics quantification and analysis was performed using excel. All samples were analyzed in quadruplicate. To adjust for total protein differences between samples, the sum of all spectral counts within each sample was taken and divided by the average of the spectral count sums in log-phase LD fractions. This ensures differences observed in the proteomics data is not due to unequal ‘loading’ into the MS. To generate heat maps and volcano plots, Log2 values were calculated for the ratio of average protein expression in log-phase and AGR (i.e. Log2(protein A in AGR/protein A in log)). Confidence analysis on LD fractions was performed essentially as described previously (Bersuker et al., 2018). Specifically, the LD confidence score is a measurement of spectral counts for each protein in the LD fraction, subtracted by their spectral counts in the infranatant fraction. Therefore, the score reports on the most abundant proteins

present in the LD fraction in a given growth condition. Confidence score is calculated as the product of two equations outlined below:

$$Equation\ \#1 = \sum_{LD=1}^{LD=k} (X_{LD,P} - X_{Inf,P})$$

$$Equation\ \#2 = \sum_{LD=1}^{LD=k} R_{LD,P}$$

In equation #1, X is the spectral abundance of a given protein in the LD fraction ($X_{LD,P}$) or in the infranatant fraction ($X_{Inf,\ P}$). Equation #2 describes the number of times a protein was detected in the LD fraction dataset for a given growth condition. For proteins that were more abundant in the infranatant fraction than the LD fraction, i.e. equation #1<0, values were artificially set to zero. Difference in LD confidence scores was calculated by subtracting the AGR LD confidence score for each protein by the log-phase LD confidence score. Whole-cell abundance factors represent the sum of spectral counts for each protein in a given growth condition. Differences in whole-cell abundance factors represent protein abundance in AGR subtracted by protein abundance in log-phase.

**Radiolabeling, metabolite extraction, and metabolite separation**

Method for radiolabeling is generally outlined in **Chapter** four but will be repeated briefly here. Approximately 100OD units of cells were used for radiolabeling experiments. All cells were grown and treated with AGR as previously described. Prior to radiolabeling, cells were collected by centrifugation and washed with dextrose-free media. All liquid was removed from cell pellets prior to labeling. To start radiolabeling, 1.0mL of dextrose-free media containing 5μCi/mL $^{14}$C-Acetate was quickly added to each tube, followed by mixing with pipetting. Tubes were tumbled in a 30°C rotating incubator for fifteen minutes. To quench the radiolabeling reaction, and wash the cells, samples were pipetted into 20mL of -40°C quenching buffer (60% methanol; 1mM tricine pH 7.4). Cells were incubated in quenching buffer for three minutes, centrifuged at 3,000xg at -10°C, and washed with 20mL of -40°C quenching buffer. Cells were again pelleted by centrifugation, and pellets for lipid extraction

were stored at -80°C. For pellets undergoing soluble metabolite extraction, all quenching buffer was thoroughly removed and 1.5mL of 80°C 75% ethanol was added to each sample followed by a three-minute incubation at 80°C and a subsequent five minute incubation on ice. Debris was removed from metabolite extract by centrifuging at 20,000xg for one minute. HMG-CoA labeled during the pulse was separated and quantified as mevalonate. To convert endogenous HMG-CoA to mevalonate, ethanol was thoroughly evaporated from isolated metabolites under argon gas, and each sample was resuspended in HMGCR buffer (50mM Tris-HCl, pH 6.8; 1mM NaCl; 1mM $MgCl_2$; 1mM DTT; 100mM glucose-6-phosphate; 1mM NADP+; 1mM NADPH). The samples were split into two tubes, one tube would be treated with enzymes, and the untreated tubes acted as blanks for endogenous mevalonate labeled during the pulse. For treated tubes, 2U of HMGCR enzyme (Sigma H7039) and 2U of glucose-6 phosphate dehydrogenase (Sigma G6378) were added. Reactions were carried out over night at 37°C. Prior to loading samples onto TLC plates, total radioactivity in each sample was quantified by scintillation counting and loading was adjusted accordingly. HMGCR Reactions were spotted onto Silica gel G plates (Miles scientific P01911) and separated with a mobile phase of 70:25:5 Diethyl ether:glacial acetic acid:water. Each lane was doped with 5µg of unlabeled mevalonate to act as a tracer for downstream scraping/quantification. TLC plates were developed overnight by autoradiography and visualized in an Amersham Typhoon FLA 9500 developer. To visualize the unlabeled tracer mevalonate, plates were sprayed with p-anisaldehyde reagent and baked at 140°C for ten minutes. Individual bands were scraped, mixed with 6mL of EcoLume scintillation cocktail (VWR cat. IC88247001), and quantified by scintillation counting in a Beckman LS 6500 instrument. Mevalonate from the untreated samples was averaged and subtracted from the final values of the treated samples. For lipid extracts, an aliquot of cell lysate was taken immediately following bead beating and radioactivity was quantified by scintillation counting to serve as a normalization standard prior to loading samples onto the TLC plate. Lipid extraction was performed as described above. To separate squalene, ergosterol, DAG, and sterol-esters, total lipid extracts were spotted onto silica gel 60G plates (Fisher cat. NC9825743), and developed in a mobile phase of 55:35:10:1 hexane:petroleum ether:diethyl ether:glacial acetic acid. Autoradiography and scintillation

counting was performed as indicated above. Prior to TLC separation, unlabeled squalene, ergosterol and sterol-ester was added to each lane of the plate as tracer. DAG and ergosterol were quantified by densitometry in Fiji.

**Cryo-sample preparation and Cryo-FIB milling**

4 µl of the cultured yeast cells were added to a glow-discharged (30 seconds at -30 mA) copper R2/2 holey carbon grid (Quantifoil Micro Tools GmbH, Jena, Germany), then the grid was rapidly plunge frozen in liquid ethane using a homemade plunge freezer and stored in liquid nitrogen until used. Cryo-FIB milling was performed as previously described (Hariri et al., 2019). Briefly, grids were mounted in notched cryo-FIB Autogrids (Thermo Fisher Scientific, MA, USA), then loaded into a shuttle under cryogenic conditions and transferred into an Aquilos dual-beam instrument equipped with a cryo-stage (FIB/SEM; Thermo Fisher Scientific). The sample surface was sputter-coated with platinum for 20 s at 30 mA current and then coated with a layer of organometallic platinum using the gas injection system for 6s at a distance of 1 mm before milling. Bulk milling was performed with a 30 kV gallium ion beam of 0.1 nA perpendicular to the grid on two side of a target yeast cell. The stage was then tilted to 10°-18° (so that the bulk-mill-holes lined up in front and behind the cell), and the cell was milled with 30 kV gallium ion beams of 100 pA current for rough milling and 30 pA for polishing until the final lamella was 100-200nm thick.

**Cryo-ET and image processing**

Lamellae were imaged using a Titan Krios transmission electron microscope (FEI/Thermo Fisher Scientific) operated at 300 kV. Images were captured using a 4k × 4k K2 direct detection camera (Gatan, Pleasanton, CA) at a magnification of 26,000x (5.5 Å pixel size) or a 5k × 6k K3 direct detection camera (Gatan, Pleasanton, CA) at a magnification of 15,000x (5.7 Å pixel size). Tilt series were collected from 60° to -60° in 2° increments using a dose-symmetric tilting scheme (Hagen et al., 2017). Counting modes of the K2 and K3 cameras were used and for each tilt image 15 frames (0.4 s exposure time per frame for K2 and 0.04 s exposure time per frame for K3) were recorded. Both cameras were placed behind a post-column energy filter

(Gatan) that was operated in zero-loss mode (20-eV slit width). The defocus was set to −0.5 μm using a Volta phase plate (Danev et al., 2014). Data acquisition was performed using the microscope control software SerialEM (Mastronarde, 2005) in low-dose mode, and the total electron dose per tilt series was limited to ∼100 e/Å2. The frames of each tilt series image were motion-corrected using MotionCor2 (Zheng et al., 2017) and then merged using the script extracted from the IMOD software package (Kremer et al., 1996) to generate the final tilt serial data set. Tilt series images were aligned fiducial-less using patch tracking (800 × 800-pixel size) and the tomogram was reconstructed by the back-projection method using the IMOD software package (Kremer et al., 1996). To reduce noise, the cryo-tomograms were filtered with nonlinear anisotropic diffusion in the IMOD package.

**Statistical analysis**

T-tests and one-way ANOVA tests were performed using Graphpad Prism8 software. Kolmogorov-Smirnov test was conducted using kstest2 MATLAB function. All unpaired t-tests were performed with Welch's correction. For one-way ANOVA, Brown-Forsyth and Welch ANOVA was performed to account for non-uniform standard deviations, followed by Turkey's post-hoc test to extract p-values. For all t-tests and ANOVAs. * p-value<0.05, **p-value<0.01, ***p-value<0.001. Dotted lines in violin plots represent the median of the data, while upper and lower dotted lines represent the upper and lower quartiles. Bar graphs show mean of the data with error bars indicating the standard deviation.

# CHAPTER SIX

## Discussion and future directions

### Significance

Though the NVJ is often noted as one of the most well-characterized ER-MCSs, the specific functions of the NVJ have proven to be elusive. Proteins involved in multiple cellular processes have been localized to the NVJ, and the mechanism of targeting for a sub-set of these proteins has been revealed. However, several questions remain about the mechanistic underpinnings of the NVJ and its influence on resident client proteins. **The goal of my research was to better understand how the NVJ regulates non-canonical ER-MCS clients and the down-stream physiological effects of enriching these clients at a sub-organelle compartment**. Like several other ER-MCSs observed between yeast and humans, the tethering complexes of the NVJ are not conserved, but mechanism by which the NVJ influences client proteins might be conserved, making the NVJ an excellent model to study enzyme compartmentalization at MCSs. Importantly, the spatial regulation of human HMGCR has not been characterized, owing potentially to HMGCR's sensitivity to tagging with fluorescent proteins. If HMGCR could be reliably visualized at high resolution in mammalian cells, we could corroborate our findings in a new model organism and potentially uncover a novel mechanism of regulation for this biomedically relevant enzyme. Similarly, LCL-LDs have been observed in the fatty streaks of human aorta. While it is not understood if they perform a protective or pathological function, studies in yeast may aid our understanding of their proteomes, lipidomes, and functions.

### Protein compositional control at the NVJ

One outstanding question about ER-MCSs is how they accomplish compositional plasticity, especially how client proteins are recruited during stress states but freely diffuse through an ER-MCS in non-stress states. The NVJ has served as an important model system for this question. One mechanism for NVJ compositional control appears to function through

transcriptional elements. Nvj1 is transcriptionally up-regulated during times of nutrient starvation (Hariri et al., 2018), but this alone may not be sufficient to recruit a sub-set of client proteins. Indeed, here we found Hmg1 requires the transcription factor Upc2 to enrich at the NVJ, but partitions independent of the glucose-sensitive protein Snf1. Upc2-dependent Hmg1 partitioning, surprisingly, functions independent of Nvj1 expression or localization. This points to a requirement for additional proteins that assist Hmg1 NVJ partitioning. One possible candidate is the client protein Snd3, which also partitions at the NVJ in glucose starvation. Recently, Snd3 was shown to be required for proper NVJ assembly during glucose starvation, but how Snd3 acts on Nvj1 is unclear (Tosal-Castano et al., 2021).

Another model emerging from this work is the lack of client interdependence in NVJ compositional control. That is, Nvj1 is required to recruit several clients to the NVJ, but the clients may not be strictly required to recruit each other. This is specifically true for the independence of Hmg1 on the client proteins Osh1 and Lam6/Ltc1. Deletion of either of these did not impact Hmg1 recruitment to the NVJ, implying their NVJ residency was independent of each other. This highlights Nvj1's role as the central factor dictating NVJ protein. Along these lines, Nvj1 recruits client proteins via several distinct domains. Hmg1 is recruited to the NVJ via the luminal portion of Nvj1; however, Tsc13 and Osh1 are recruited through the transmembrane and cytosolic portions of Nvj1, respectively (Kvam, 2004; Kvam et al., 2005). All these observations point to Nvj1 being a multi-functional client recruitment factor, or scaffold, which may require accessory proteins or post-translational modifications to establish a distinct protein composition at the NVJ. Although clients can enrich at the NVJ independent of one another, functional cooperativity at the NVJ may exist amongst client proteins, but additional studies will be required to uncover such cooperativity.

**Physiochemical environment of the NVJ**

One of the key knowledge gaps in the field of sub-organelle metabolic regulation continues to be what distinct physiochemical properties, if any, are associated with organelle sub-domains and how those properties assist the underlying functions of their associated sub-domains.

Changes in nutrient status have been linked to alterations of organelle physiochemical environments, such as pH and local ion concentration, particularly in the cytoplasm (Munder et al., 2016). One outstanding question is whether ER-MCSs promote or protect proteins from changing physiochemical conditions. In the work above, photobleaching experiments revealed that Hmg1 that is not clustered at the NVJ can still pass through the contact site (Figure 2.3A,B). Interestingly, Hmg1 mobility on the ER appears to slow down during AGR, even in the absence of Nvj1. While more data is required to draw a conclusion, this is consistent with lower protein mobility on the nuclear envelope during AGR. If true, this could be induced either by the gel-like transition adopted by the cytoplasm during glucose starvation or by altering the lipid composition of the nuclear envelope.

HMGCR in yeast and humans is sensitive to ER membrane composition, particularly the concentration of sterol in the ER . One possible mechanism by which the NVJ could influence its clients is by harboring a unique lipid composition. Direct observation of NVJ lipids via biosensors has not been performed to date. However, restricted localization of catalytically active Pah1 is consistent with high concentrations of PA at the NVJ (Barbosa et al., 2015). The NVJ also partitions the ELOVL enzyme Tsc13, but whether VLCFAs are spatially concentrated at the NVJ is not known. Via high-resolution EM, some groups have reported distinct ER membrane morphologies at the NVJ. Specifically, the ER membrane adjacent to the vacuole appears ‘pinched’ or narrow relative to the rest of the nuclear envelope (Millen et al., 2008), but this could be attributed to several, yet unidentified, factors. Additionally, long-term starvation promotes the formation of phase separated domains on the yeast vacuole (Rayermann et al., 2017; Toulmay and Prinz, 2013). The NVJ is noted to consistently coordinate with liquid-disordered domains on the vacuole, but whether phase separation of the vacuole membrane influences ER membrane composition, or vice-versa, remains to be uncovered. Indeed, at least one study has provided evidence suggesting ER-MCSs are phase-separated domains themselves (King et al., 2020), but this has not been verified under physiological conditions or for the NVJ.

LD biogenesis is another cellular process acutely sensitive to membrane environment. Although LD biogenesis can concentrate at the NVJ, it is not clear which step becomes enriched. Unique lipid compositions of the NVJ could aid in lens formation, recruitment of assembly factors, or accomplishment of directional budding. Loss of the NVJ, and the perturbed LD organization, leads to defects in nuclear pore assembly (Lord and Wente, 2020). Therefore, NVJ-associated LD biogenesis could help to control the lipid composition of the nuclear envelope and help maintain protein homeostasis therein. Additional studies are required to probe the membrane environment of the NVJ relative to the rest of the nuclear envelope and whether this environment influences the activity of NVJ client enzymes (Pah1, Tsc13, Hmg1) or LD biogenesis.

**NVJ-derived mevalonate production and cell growth resumption**

One down-stream effect of NVJ Hmg1 partitioning that we have identified is an influence on cell growth resumption following a low-glucose to high-glucose transition of yeast cells. This indicates that the lack of HMGCR partitioning at the NVJ impacts cell adaptation to changes in nutrient availability. Mevalonate production has been tied to cell cycle progression previously (Quesney-Huneeus et al., 1983). However, due to the myriad destinations and utilities of mevalonate and its derivative metabolites, identifying the exact mechanism for mevalonate-controlled growth resumption has not yet been possible. It has also been noted elsewhere that NVJ size strongly correlates with cell fate decision, thereby supporting a model where the NVJ, and its resident clients, help define cellular metabolic states that promote longevity (Wood et al., 2020). One critical destination for mevalonate, aside from sterol, is the production of CoQ. CoQ is an essential cofactor in the electron transport chain and is synthesized, in part, from mevalonate-derived isoprenoids. Therefore, CoQ production, and mevalonate production, become important during states that require cellular respiration, like AGR treatment.

An alternative destination for NVJ-mediated mevalonate production is the storage of SEs into LCL-LDs, discussed at length in chapter three. No functions have been described for LCL-

LDs in either yeast or mammalian cells; however, the preferential protection of SE over TAG supports a model where SEs may become important during times of cell growth. Indeed, SEs contain two moieties that are essential for building membranes in times of cellular growth: sterol and FFAs. Therefore, NVJ-derived mevalonate may somehow be preferentially shunted into SEs to support late-term growth resumption following starvation.

**Spatial regulation of HMGCR at the NVJ**

Above, we demonstrated that artificial multimerization of Hmg1 can bypass the loss of Nvj1 and rescue growth defects of an Nvj1 knock-out. AGR-induced clustering of Hmg1 at the NVJ and subsequent up-regulation of mevalonate pathway flux correlates with the appearance of HMW Hmg1 species. Although sizing estimates based on BN-PAGE biochemical analysis gives only a coarse-grained understanding of protein complex sizes, HMW species of Hmg1 were observed around 720kDa, which is much larger than the expected ~400kDa of an Hmg1 tetramer. Human HMGCR tetramerization is undoubtedly necessary for proper HMGCR catalytic function; however, the oligomeric state of yeast Hmg1 has not been empirically demonstrated. Although, both the catalytic domain and residues predicted to participate in HMGCR oligomerization are conserved from yeast to humans. One question that remains open is 'how does concentration of Hmg1 at the NVJ affect Hmg1 activity?'. A few recent studies have showed that liquid-liquid phase separation of proteins into condensates can increase enzymatic activity (Loring et al., 2021; Peeples and Rosen, 2021). One possibility is that binding to a scaffold, Nvj1 in this case, increases the lifetime of the catalytic multimer by inhibiting complex disassembly. Little is known about Hmg1 multimerization kinetics; therefore, further experiments are required before conclusions can be made about Nvj1's influence on Hmg1 multimerization and activity.

One well-characterized form of HMGCR regulation is through protein synthesis and degradation, as discussed in the introduction section. Loss of Nvj1 clearly impacts Hmg1 protein synthesis; however, a conclusion has not yet been made about the role of Nvj1 in Hmg1 degradation. It seems that during Hmg1 NVJ partitioning, Hmg1 steady-state protein levels

stabilize, which is consistent with a cellular demand for mevalonate production and lower Hmg1 protein degradation. It is not clear, however, whether NVJ partitioning of Hmg1 increases the half-life of Hmg1 protein. While it is possible that NVJ partitioning could protect a pool of Hmg1 from degradation, we do not yet have enough data to conclude this.

**LCL-LD formation and LD proteome remodeling**

In chapter three, TAG lipolysis was found to play a critical role in LCL-LD formation; however, *de-novo* SE synthesis may play a yet unidentified role as well. Nvj1 knock-out cells are able to produce LCL-LDs as efficiently as WT cells, but this could be explained by an adjustment of Hmg1/2 protein expression in the absence of Nvj1. Alternatively, *de-novo* SE synthesis from NVJ-derived mevalonate may not be necessary for LCL-LD formation, and SE phase separation could predominantly arise from TAG lipolysis on existing LDs. In accordance with this, Erg6 falls off LDs after approximately 1 hour of AGR treatment; meanwhile, Hmg1/2 clustering is not visible until about 2-3 hours following AGR treatment. Therefore, LCL-LD formation may precede Hmg1/2 clustering and NVJ-mediated mevalonate production. Undoubtedly, more work needs to be done before we comprehensively understand the coordination between Hmg1 clustering, NVJ-mediated LD biogenesis, and LCL-LD formation during AGR stress.

Our proteomics of LCL-LDs identified a surprising decrease in ergosterol biosynthesis proteins on LDs. Although this appears counterintuitive to the increase in AGR-induced mevalonate pathway flux, mass exit of Erg proteins could support SE biosynthesis. Erg1 shows dual targeting between the ER and LDs during ambient conditions. However, LD-localized Erg1 is less catalytically active than the ER-localized enzyme (Leber et al., 1998). This could be due to preference of the enzyme for a bilayer over a monolayer surface, or due to preferential partitioning of Erg1 substrate to the ER. While this has been demonstrated for Erg1, catalytic activity of other Erg proteins have not been reported to be modulated by LD/ER targeting. Importantly, Erg1 is the second rate-limiting step in sterol biogenesis, and up-regulation of Hmg1/Erg1 together may be sufficient to drive mevalonate pathways flux.

**Future directions**

The NVJ has proven a useful model ER-MCS to uncover several unexpected cellular phenomena, including regulation of enzyme activity via spatial partitioning, and the formation of peculiar, phase separated, LDs. The utility of NVJ is, partially, derived from the diversity of proteins that concentrate there and the genetic malleability provided by yeast that allows for the mechanistic dissection of NVJ function. With the closing of the studies presented above, the field is now poised to attain mechanistic understanding of several important biochemical processes that occur at the NVJ and on LCL-LDs.

*NVJ protein and lipid composition*

With the advent of cross-linking mass-spectrometry (XL-MS), a greater appreciation may be gained for the complex protein composition of the NVJ under distinct stress states. Furthermore, *in-vitro* reconstitution of Nvj1 and its client proteins may provide evidence for how Nvj1 recruits and maintains several distinct clients simultaneously. Understanding Nvj1-client protein interactions will be essential to gain an understanding of how Nvj1 exerts its influence over non-canonical ER-MCS clients, like Hmg1.

Similarly, the NVJ is involved in several lipid metabolic processes, but it is not yet known if the NVJ possesses a unique lipid environment that helps facilitate these processes. *In-vivo* fluorescent lipid biosensors are rapidly being developed for a wide array of lipid species. One obvious target to measure at the NVJ would be PA. Active Pah1 binds PA and is also found concentrated at the NVJ in certain states. Additionally, PA is an important branchpoint in lipid metabolism because it can be shunted into growth lipids (i.e. phospholipids) or storage lipids (i.e. triglyceride). Given the connection between the NVJ and the storage of lipids into LDs, the NVJ may represent a spatial platform for the conversion of PA into TAG for subsequent storage.

*NVJ regulation of mevalonate flux*

If a greater understanding of Nvj1's influence on Hmg1 is to be attained, much more needs to be understood about how Hmg1 localizes to the NVJ. The key to unlocking the mystery behind Hmg1 partitioning could be the transcription factor Upc2. It is unlikely that Upc2 physically localizes to the NVJ during AGR; rather, Upc2 most likely is required for the expression of an accessory protein that is necessary for Hmg1 partitioning. One path to dissecting this problem could be through global proteomic analysis of Upc2 knock-out cells during log-phase and AGR. Identification of potential accessory proteins would provide additional genetic tools for interpreting the mechanistic influence of Hmg1 NVJ partitioning. Mechanistic understanding of Hmg1 catalytic activity at the NVJ will likely require *in-vitro* reconstitutions of minimal NVJ components and subsequent enzyme kinetic characterization. One standing inquiry about the NVJ is whether Hmg1 specifically 'needs' the NVJ. Artificial multimerization of Hmg1 appears sufficient to bypass loss of Nvj1, therefore, the NVJ may not be strictly required for proper Hmg1 function. However, localization at the NVJ may influence mevalonate pathway flux in unexpected ways.

Though AGR clearly promotes mevalonate pathway flux, it is not yet clear the end-point destination for this mevalonate, and how its division into distinct cellular destinations is altered during stress such as glucose restriction. One barrier to investigation of this is the incorporation of mevalonate into such diverse sets of biomolecules. Mevalonate can be shunted into tRNA synthesis, protein prenylation, vitamin production, heme synthesis, and several diverse lipids. Measuring all these products would be difficult; however, it may be possible to measure several of these species via a multi-omics approach (i.e. metabolomics, lipidomics, proteomics). Coupling multi-omics with stable isotope labelling to track mevalonate destinations during Hmg1 clustering would provide an even greater understanding of the role mevalonate plays during cellular respiration states. It may also help to answer a long-standing question about how cells decide to portion-out their mevalonate stores into multiple distinct destinations.

*LCL-LD functions and maintenance*

Potential functions of LCL-LDs have been difficult to identify owing to a lack of treatments that prevent or inducibly reverse LCL-LD formation. The preferential storage of SEs during AGR is particularly curious, given they are a significant source of FFAs. Whole-cell proteomics data reveals that β-oxidation in the peroxisomes, and subsequent up-regulation of cellular respiration, is prevalent during AGR stress. However, yeast preferentially mobilize TAG in preference to SE as an alternative carbon source. One possibility is that SE hydrolysis would not only create available FFAs for β-oxidation, but also an abundance of free sterol, which could prove cytotoxic. Therefore, it appears that SEs are retained for times of active growth. Although TAG is significantly turned-over during AGR, yeast maintain a small pool of TAG. An alternative hypothesis, therefore, is that SE phase transitions protect a small pool of TAG in the hydrophobic core of LDs from degradation. One *in-vitro* study of artificial LDs has shown that increasing concentrations of SE in LDs protects TAG from oxidative stress (Lange et al., 2021). Though the authors did not specify, this could be linked to SE phase transitions protecting TAG-rich LD cores from oxidative damage induced by free radicals.

*In conclusion….*

Sub-organelle organization of metabolic processes continues to be an exciting and challenging topic to investigate experimentally. The NVJ has proven a useful model ER-MCS to understand not only this broad category of biology, but also to better understand the behavior and utilities of ER-MCSs. The connections drawn between the NVJ, the mevalonate pathway, and LD core phase separation would have never been made if not for exploration-based methods. It is my sincere hope that future investigations into the NVJ will continue to shine light on uncovered areas of biology in unexpected ways.

## Appendix A

## Featured publications

1) Chapter two was replicated in full from my first author publication (Rogers et al. *eLife* 2021)

2) Chapter three was my first author contribution to a manuscript that was recently submitted and can be found as a pre-print on *BioRxiv*

3) Chapter four was replicated in full from my first author publication (Rogers and Henne. *JOVE* 2021)

# Bibliography


AhYoung, A.P., and Egea, P.F. (2019). Determining the Lipid-Binding Specificity of SMP Domains: An ERMES Subunit as a Case Study. Methods Mol Biol *1949*, 213–235.

Alva, V., and Lupas, A.N. (2016). The TULIP superfamily of eukaryotic lipid-binding proteins as a mediator of lipid sensing and transport. Biochim Biophys Acta *1861*, 913–923.

Aronova, M.A., Sousa, A.A., and Leapman, R.D. (2011). EELS characterization of radiolytic products in frozen samples. Micron (Oxford, England : 1993) *42*, 252–256.

Arrese, E.L., Saudale, F.Z., and Soulages, J.L. (2014). Lipid Droplets as Signaling Platforms Linking Metabolic and Cellular Functions. Lipid Insights *7*, 7–16.

Bacle, A., Gautier, R., Jackson, C.L., Fuchs, P.F.J., and Vanni, S. (2017). Interdigitation between Triglycerides and Lipids Modulates Surface Properties of Lipid Droplets. Biophys J *112*, 1417–1430.

Banani, S.F., Lee, H.O., Hyman, A.A., and Rosen, M.K. (2017). Biomolecular condensates: organizers of cellular biochemistry. Nat Rev Mol Cell Biol *18*, 285–298.

Barbosa, A.D., Sembongi, H., Su, W.-M., Abreu, S., Reggiori, F., Carman, G.M., and Siniossoglou, S. (2015). Lipid partitioning at the nuclear envelope controls membrane biogenesis. MBoC *26*, 3641–3657.

Bartok, A., Weaver, D., Golenár, T., Nichtova, Z., Katona, M., Bánsághi, S., Alzayady, K.J., Thomas, V.K., Ando, H., Mikoshiba, K., et al. (2019). IP3 receptor isoforms differently regulate ER-mitochondrial contacts and local calcium transfer. Nat Commun *10*, 3726.

Basso, V., Marchesan, E., and Ziviani, E. (2020). A trio has turned into a quartet: DJ-1 interacts with the IP3R-Grp75-VDAC complex to control ER-mitochondria interaction. Cell Calcium *87*, 102186.

Beaty, N.B., and Lane, M.D. (1983). Kinetics of activation of acetyl-CoA carboxylase by citrate. Relationship to the rate of polymerization of the enzyme. J Biol Chem *258*, 13043–13050.

Belgareh-Touzé, N., Cavellini, L., and Cohen, M.M. (2017). Ubiquitination of ERMES components by the E3 ligase Rsp5 is involved in mitophagy. Autophagy *13*, 114–132.

Ben M'barek, K., Ajjaji, D., Chorlay, A., Vanni, S., Forêt, L., and Thiam, A.R. (2017). ER Membrane Phospholipids and Surface Tension Control Cellular Lipid Droplet Formation. Dev Cell *41*, 591-604.e7.

Bersuker, K., and Olzmann, J.A. (2017). Establishing the lipid droplet proteome: Mechanisms of lipid droplet protein targeting and degradation. Biochim Biophys Acta Mol Cell Biol Lipids *1862*, 1166–1177.

Bersuker, K., Peterson, C.W.H., To, M., Sahl, S.J., Savikhin, V., Grossman, E.A., Nomura, D.K., and Olzmann, J.A. (2018). A Proximity Labeling Strategy Provides Insights into the Composition and Dynamics of Lipid Droplet Proteomes. Dev Cell *44*, 97-112.e7.

Bhatt-Wessel, B., Jordan, T.W., Miller, J.H., and Peng, L. (2018). Role of DGAT enzymes in triacylglycerol metabolism. Arch Biochem Biophys *655*, 1–11.

Blachly-Dyson, E., and Forte, M. (2001). VDAC channels. IUBMB Life *52*, 113–118.

Bolte, S., and Cordelières, F.P. (2006). A guided tour into subcellular colocalization analysis in light microscopy. Journal of Microscopy *224*, 213–232.

Bononi, A., Missiroli, S., Poletti, F., Suski, J.M., Agnoletto, C., Bonora, M., De Marchi, E., Giorgi, C., Marchi, S., Patergnani, S., et al. (2012). Mitochondria-associated membranes (MAMs) as hotspot Ca(2+) signaling units. Adv Exp Med Biol *740*, 411–437.

Borrull, A., López-Martínez, G., Poblet, M., Cordero-Otero, R., and Rozès, N. (2015). A simple method for the separation and quantification of neutral lipid species using GC-MS: Simple method for separation & quantification of neutral lipid using GC-MS. Eur. J. Lipid Sci. Technol. *117*, 274–280.

Breil, C., Abert Vian, M., Zemb, T., Kunz, W., and Chemat, F. (2017). "Bligh and Dyer" and Folch Methods for Solid–Liquid–Liquid Extraction of Lipids from Microorganisms. Comprehension of Solvatation Mechanisms and towards Substitution with Alternative Solvents. IJMS *18*, 708.

Bui, Q., Sherma, J., and Hines, J.K. (2018). Using High Performance Thin Layer Chromatography-Densitometry to Study the Influence of the Prion [RNQ+] and Its Determinant Prion Protein Rnq1 on Yeast Lipid Profiles. Separations *5*.

Burg, J.S., and Espenshade, P.J. (2011). Regulation of HMG-CoA reductase in mammals and yeast. Prog Lipid Res *50*, 403–410.

Buttke, T.M., and Pyle, A.L. (1982). Effects of unsaturated fatty acid deprivation on neutral lipid synthesis in Saccharomyces cerevisiae. J Bacteriol *152*, 747–756.

Caillon, L., Nieto, V., Gehan, P., Omrane, M., Rodriguez, N., Monticelli, L., and Thiam, A.R. (2020). Triacylglycerols sequester monotopic membrane proteins to lipid droplets. Nat Commun *11*, 3944.

Cartwright, B.R., Binns, D.D., Hilton, C.L., Han, S., Gao, Q., and Goodman, J.M. (2015). Seipin performs dissectible functions in promoting lipid droplet biogenesis and regulating droplet morphology. MBoC *26*, 726–739.

Castro, I.G., Eisenberg-Bord, M., Persiani, E., Rochford, J.J., Schuldiner, M., and Bohnert, M. (2019). Promethin Is a Conserved Seipin Partner Protein. Cells *8*, E268.

Chan, C.Y., Zhao, H., Pugh, R.J., Pedley, A.M., French, J., Jones, S.A., Zhuang, X., Jinnah, H., Huang, T.J., and Benkovic, S.J. (2015). Purinosome formation as a function of the cell cycle. Proc Natl Acad Sci USA *112*, 1368–1373.

Chang, C.-L., and Liou, J. (2015). Phosphatidylinositol 4,5-Bisphosphate Homeostasis Regulated by Nir2 and Nir3 Proteins at Endoplasmic Reticulum-Plasma Membrane Junctions. Journal of Biological Chemistry *290*, 14289–14301.

Chang, T.Y., Chang, C.C., and Cheng, D. (1997). Acyl-coenzyme A:cholesterol acyltransferase. Annu Rev Biochem *66*, 613–638.

Cho, K.F., Branon, T.C., Rajeev, S., Svinkina, T., Udeshi, N.D., Thoudam, T., Kwak, C., Rhee, H.-W., Lee, I.-K., Carr, S.A., et al. (2020). Split-TurboID enables contact-dependent proximity labeling in cells. Proc Natl Acad Sci USA *117*, 12143–12154.

Chorlay, A., and Thiam, A.R. (2018). An Asymmetry in Monolayer Tension Regulates Lipid Droplet Budding Direction. Biophys J *114*, 631–640.

Chorlay, A., and Thiam, A.R. (2020). Neutral lipids regulate amphipathic helix affinity for model lipid droplets. J Cell Biol *219*, e201907099.

Chorlay, A., Monticelli, L., Veríssimo Ferreira, J., Ben M'barek, K., Ajjaji, D., Wang, S., Johnson, E., Beck, R., Omrane, M., Beller, M., et al. (2019). Membrane Asymmetry Imposes Directionality on Lipid Droplet Emergence from the ER. Developmental Cell *50*, 25-42.e7.

Chung, J., Wu, X., Lambert, T.J., Lai, Z.W., Walther, T.C., and Farese, R.V. (2019). LDAF1 and Seipin Form a Lipid Droplet Assembly Complex. Developmental Cell *51*, 551-563.e7.

Cogliati, S., Enriquez, J.A., and Scorrano, L. (2016). Mitochondrial Cristae: Where Beauty Meets Functionality. Trends in Biochemical Sciences *41*, 261–273.

Cottier, S., and Schneiter, R. (2022). Lipid droplets form a network interconnected by the endoplasmic reticulum through which their proteins equilibrate. Journal of Cell Science *135*, jcs258819.

Currie, E., Guo, X., Christiano, R., Chitraju, C., Kory, N., Harrison, K., Haas, J., Walther, T.C., and Farese, R.V. (2014). High confidence proteomic analysis of yeast LDs identifies additional droplet proteins and reveals connections to dolichol synthesis and sterol acetylation. J Lipid Res *55*, 1465–1477.

Czabany, T., Wagner, A., Zweytick, D., Lohner, K., Leitner, E., Ingolic, E., and Daum, G. (2008). Structural and Biochemical Properties of Lipid Particles from the Yeast Saccharomyces cerevisiae. Journal of Biological Chemistry *283*, 17065–17074.

Danev, R., Buijsse, B., Khoshouei, M., Plitzko, J.M., and Baumeister, W. (2014). Volta potential phase plate for in-focus phase contrast transmission electron microscopy. Proc. Natl. Acad. Sci. U.S.A. *111*, 15635–15640.

Di Mattia, T., Martinet, A., Ikhlef, S., McEwen, A.G., Nominé, Y., Wendling, C., Poussin-Courmontagne, P., Voilquin, L., Eberling, P., Ruffenach, F., et al. (2020). FFAT motif phosphorylation controls formation and lipid transfer function of inter-organelle contacts. EMBO J *39*, e104369.

Dickson, E.J., Jensen, J.B., Vivas, O., Kruse, M., Traynor-Kaplan, A.E., and Hille, B. (2016). Dynamic formation of ER–PM junctions presents a lipid phosphatase to regulate phosphoinositides. Journal of Cell Biology *213*, 33–48.

Doncic, A., Eser, U., Atay, O., and Skotheim, J.M. (2013). An algorithm to automate yeast segmentation and tracking. PLoS ONE *8*, e57970.

Dudkina, N.V., Eubel, H., Keegstra, W., Boekema, E.J., and Braun, H.-P. (2005). Structure of a mitochondrial supercomplex formed by respiratory-chain complexes I and III. Proceedings of the National Academy of Sciences *102*, 3225–3229.

Dueber, J.E., Wu, G.C., Malmirchegini, G.R., Moon, T.S., Petzold, C.J., Ullal, A.V., Prather, K.L.J., and Keasling, J.D. (2009). Synthetic protein scaffolds provide modular control over metabolic flux. Nat Biotechnol *27*, 753–759.

Eisenberg, T., and Büttner, S. (2014). Lipids and cell death in yeast. FEMS Yeast Res *14*, 179–197.

Eisenberg-Bord, M., Shai, N., Schuldiner, M., and Bohnert, M. (2016). A Tether Is a Tether Is a Tether: Tethering at Membrane Contact Sites. Dev Cell *39*, 395–409.

Eisenberg-Bord, M., Mari, M., Weill, U., Rosenfeld-Gur, E., Moldavski, O., Castro, I.G., Soni, K.G., Harpaz, N., Levine, T.P., Futerman, A.H., et al. (2018). Identification of seipin-linked factors that act as determinants of a lipid droplet subpopulation. Journal of Cell Biology *217*, 269–282.

Eisenberg-Bord, M., Tsui, H.S., Antunes, D., Fernandez-del-Rio, L., Bradley, M.C., Dunn, C.D., Nguyen, T.P.T., Rapaport, D., Clarke, C.F., and Schuldiner, M. (2019). The Endoplasmic Reticulum-Mitochondria Encounter Structure Complex Coordinates Coenzyme Q Biosynthesis. Contact.

Elbaz-Alon, Y., Rosenfeld-Gur, E., Shinder, V., Futerman, A.H., Geiger, T., and Schuldiner, M. (2014). A dynamic interface between vacuoles and mitochondria in yeast. Dev Cell *30*, 95–102.

Elbaz-Alon, Y., Eisenberg-Bord, M., Shinder, V., Stiller, S.B., Shimoni, E., Wiedemann, N., Geiger, T., and Schuldiner, M. (2015). Lam6 Regulates the Extent of Contacts between Organelles. Cell Rep *12*, 7–14.

Engelman, D.M., and Hillman, G.M. (1976). Molecular organization of the cholesteryl ester droplets in the fatty streaks of human aorta. J. Clin. Invest. *58*, 997–1007.

English, A.M., Schuler, M.-H., Xiao, T., Kornmann, B., Shaw, J.M., and Hughes, A.L. (2020). ER-mitochondria contacts promote mitochondrial-derived compartment biogenesis. J Cell Biol *219*, e202002144.

Ericson, D., Ellen, R.P., and Buivids, I. (1987). Labeling of binding sites for beta 2-microglobulin (beta 2m) on nonfibrillar surface structures of mutans streptococci by immunogold and beta 2m-gold electron microscopy. J Bacteriol *169*, 2507–2515.

Folch, J., Lees, M., and Sloane Stanley, G.H. (1957). A simple method for the isolation and purification of total lipides from animal tissues. J. Biol. Chem. *226*, 497–509.

Friedman, J.R., Lackner, L.L., West, M., DiBenedetto, J.R., Nunnari, J., and Voeltz, G.K. (2011). ER Tubules Mark Sites of Mitochondrial Drivision. Science *334*, 358–362.

Fuchs, B., Süß, R., Teuber, K., Eibisch, M., and Schiller, J. (2011). Lipid analysis by thin-layer chromatography—A review of the current state. Journal of Chromatography A *1218*, 2754–2774.

Gaigg, B., Simbeni, R., Hrastnik, C., Paltauf, F., and Daum, G. (1995). Characterization of a microsomal subfraction associated with mitochondria of the yeast, Saccharomyces cerevisiae. Involvement in synthesis and import of phospholipids into mitochondria. Biochimica et Biophysica Acta (BBA) - Biomembranes *1234*, 214–220.

Gao, Q., Binns, D.D., Kinch, L.N., Grishin, N.V., Ortiz, N., Chen, X., and Goodman, J.M. (2017). Pet10p is a yeast perilipin that stabilizes lipid droplets and promotes their assembly. J Cell Biol *216*, 3199–3217.

Gatta, A.T., and Levine, T.P. (2017). Piecing Together the Patchwork of Contact Sites. Trends Cell Biol *27*, 214–229.

Gault, C.R., Obeid, L.M., and Hannun, Y.A. (2010). An overview of sphingolipid metabolism: from synthesis to breakdown. Adv Exp Med Biol *688*, 1–23.

Ghai, R., Du, X., Wang, H., Dong, J., Ferguson, C., Brown, A.J., Parton, R.G., Wu, J.-W., and Yang, H. (2017). ORP5 and ORP8 bind phosphatidylinositol-4, 5-biphosphate (PtdIns(4,5)P 2) and regulate its level at the plasma membrane. Nat Commun *8*, 757.

Gibellini, F., and Smith, T.K. (2010). The Kennedy pathway--De novo synthesis of phosphatidylethanolamine and phosphatidylcholine. IUBMB Life *62*, 414–428.

Giménez-Andrés, M., Čopič, A., and Antonny, B. (2018). The Many Faces of Amphipathic Helices. Biomolecules *8*, E45.

Giménez-Andrés, M., Emeršič, T., Antoine-Bally, S., D'Ambrosio, J.M., Antonny, B., Derganc, J., and Čopič, A. (2021). Exceptional stability of a perilipin on lipid droplets depends on its polar residues, suggesting multimeric assembly. Elife *10*, e61401.

Ginsburg, G.S., Walsh, M.T., Small, D.M., and Atkinson, D. (1984). Reassembled plasma low density lipoproteins. Phospholipid-cholesterol ester-apoprotein B complexes. The Journal of Biological Chemistry *259*, 6667–6673.

Gomez-Suaga, P., Paillusson, S., Stoica, R., Noble, W., Hanger, D.P., and Miller, C.C.J. (2017). The ER-Mitochondria Tethering Complex VAPB-PTPIP51 Regulates Autophagy. Curr Biol *27*, 371–385.

Gu, J., Wu, M., Guo, R., Yan, K., Lei, J., Gao, N., and Yang, M. (2016). The architecture of the mammalian respirasome. Nature *537*, 639–643.

Guo, R., Gu, J., Zong, S., Wu, M., and Yang, M. (2018). Structure and mechanism of mitochondrial electron transport chain. Biomedical Journal *41*, 9–20.

Hagen, W.J.H., Wan, W., and Briggs, J.A.G. (2017). Implementation of a cryo-electron tomography tilt-scheme optimized for high resolution subtomogram averaging. J. Struct. Biol. *197*, 191–198.

Hampton, R.Y., and Bhakta, H. (1997). Ubiquitin-mediated regulation of 3-hydroxy-3-methylglutaryl-CoA reductase. Proceedings of the National Academy of Sciences *94*, 12944–12948.

Hampton, R.Y., and Rine, J. (1994). Regulated degradation of HMG-CoA reductase, an integral membrane protein of the endoplasmic reticulum, in yeast. Journal of Cell Biology *125*, 299–312.

Hampton, R., Dimster-Denk, D., and Rine, J. (1996). The biology of HMG-CoA reductase: the pros of contra-regulation. Trends Biochem Sci *21*, 140–145.

Hanada, K. (2003). Serine palmitoyltransferase, a key enzyme of sphingolipid metabolism. Biochim Biophys Acta *1632*, 16–30.

Hanada, K., Kumagai, K., Tomishige, N., and Yamaji, T. (2009). CERT-mediated trafficking of ceramide. Biochim Biophys Acta *1791*, 684–691.

Hariri, H., Rogers, S., Ugrankar, R., Liu, Y.L., Feathers, J.R., and Henne, W.M. (2018). Lipid droplet biogenesis is spatially coordinated at ER –vacuole contacts under nutritional stress. EMBO Rep *19*, 57–72.

Hariri, H., Speer, N., Bowerman, J., Rogers, S., Fu, G., Reetz, E., Datta, S., Feathers, J.R., Ugrankar, R., Nicastro, D., et al. (2019). Mdm1 maintains endoplasmic reticulum homeostasis by spatially regulating lipid droplet biogenesis. J. Cell Biol. *218*, 1319–1334.

Hedbacker, K., and Carlson, M. (2008). SNF1/AMPK pathways in yeast. Front. Biosci. *13*, 2408–2420.

Henne, W.M., Zhu, L., Balogi, Z., Stefan, C., Pleiss, J.A., and Emr, S.D. (2015). Mdm1/Snx13 is a novel ER–endolysosomal interorganelle tethering protein. Journal of Cell Biology *210*, 541–551.

Henry, S.A., Kohlwein, S.D., and Carman, G.M. (2012). Metabolism and Regulation of Glycerolipids in the Yeast *Saccharomyces cerevisiae*. Genetics *190*, 317–349.

Hirabayashi, Y., Kwon, S.-K., Paek, H., Pernice, W.M., Paul, M.A., Lee, J., Erfani, P., Raczkowski, A., Petrey, D.S., Pon, L.A., et al. (2017). ER-mitochondria tethering by PDZD8 regulates Ca2+ dynamics in mammalian neurons. Science *358*, 623–630.

Hoffmann, P.C., Bharat, T.A.M., Wozny, M.R., Boulanger, J., Miller, E.A., and Kukulski, W. (2019). Tricalbins Contribute to Cellular Lipid Flux and Form Curved ER-PM Contacts that Are Bridged by Rod-Shaped Structures. Developmental Cell *51*, 488-502.e8.

Istvan, E.S. (2001). Bacterial and mammalian HMG-CoA reductases: related enzymes with distinct architectures. Curr Opin Struct Biol *11*, 746–751.

Istvan, E.S., Palnitkar, M., Buchanan, S.K., and Deisenhofer, J. (2000). Crystal structure of the catalytic portion of human HMG-CoA reductase: insights into regulation of activity and catalysis. EMBO J. *19*, 819–830.

Jacquier, N., Choudhary, V., Mari, M., Toulmay, A., Reggiori, F., and Schneiter, R. (2011). Lipid droplets are functionally connected to the endoplasmic reticulum in *Saccharomyces cerevisiae*. Journal of Cell Science *124*, 2424–2437.

Jentsch, J.-A., Kiburu, I., Pandey, K., Timme, M., Ramlall, T., Levkau, B., Wu, J., Eliezer, D., Boudker, O., and Menon, A.K. (2018). Structural basis of sterol binding and transport by a yeast StARkin domain. J Biol Chem *293*, 5522–5531.

Jeong, H., Park, J., Kim, H.-I., Lee, M., Ko, Y.-J., Lee, S., Jun, Y., and Lee, C. (2017). Mechanistic insight into the nucleus–vacuole junction based on the Vac8p–Nvj1p crystal structure. Proc Natl Acad Sci USA *114*, E4539–E4548.

Jin, M., Fuller, G.G., Han, T., Yao, Y., Alessi, A.F., Freeberg, M.A., Roach, N.P., Moresco, J.J., Karnovsky, A., Baba, M., et al. (2017). Glycolytic Enzymes Coalesce in G Bodies under Hypoxic Stress. Cell Reports *20*, 895–908.

Jo, Y., and Debose-Boyd, R.A. (2010). Control of cholesterol synthesis through regulated ER-associated degradation of HMG CoA reductase. Crit Rev Biochem Mol Biol *45*, 185–198.

Jordá, T., and Puig, S. (2020). Regulation of Ergosterol Biosynthesis in Saccharomyces cerevisiae. Genes *11*, 795.

Joshi, A.S., Nebenfuehr, B., Choudhary, V., Satpute-Krishnan, P., Levine, T.P., Golden, A., and Prinz, W.A. (2018). Lipid droplet and peroxisome biogenesis occur at the same ER subdomains. Nat Commun *9*, 2940.

Joyner, R.P., Tang, J.H., Helenius, J., Dultz, E., Brune, C., Holt, L.J., Huet, S., Muller, D.J., and Weis, K. (2016). A glucose-starvation response regulates the diffusion of macromolecules. ELife.

Kakimoto, Y., Tashiro, S., Kojima, R., Morozumi, Y., Endo, T., and Tamura, Y. (2018). Visualizing multiple inter-organelle contact sites using the organelle-targeted split-GFP system. Sci Rep *8*, 6175.

Kassan, A., Herms, A., Fernandez-Vidal, A., Bosch, M., Schieber, N.L., Reddy, B.J., Fajardo, A., Gelabert-Baldrich, M., Tebar, F., Enrich, C., et al. (2013). Acyl-CoA synthetase 3 promotes lipid droplet biogenesis in ER microdomains. The Journal of Cell Biology *203*, 985–1001.

Katz, S.S., Small, D.M., Brook, J.G., and Lees, R.S. (1977). The storage lipids in Tangier disease. A physical chemical study. J Clin Invest *59*, 1045–1054.

Kawano, S., Tamura, Y., Kojima, R., Bala, S., Asai, E., Michel, A.H., Kornmann, B., Riezman, I., Riezman, H., Sakae, Y., et al. (2018). Structure-function insights into direct lipid transfer between membranes by Mmm1-Mdm12 of ERMES. J Cell Biol *217*, 959–974.

Kim, S., and Swanson, J.M.J. (2020). The Surface and Hydration Properties of Lipid Droplets. Biophysical Journal *119*, 1958–1969.

Kim, C.-W., Moon, Y.-A., Park, S.W., Cheng, D., Kwon, H.J., and Horton, J.D. (2010). Induced polymerization of mammalian acetyl-CoA carboxylase by MIG12 provides a tertiary level of regulation of fatty acid synthesis. Proc. Natl. Acad. Sci. U.S.A. *107*, 9626–9631.

Kim, Y.J., Guzman-Hernandez, M.-L., Wisniewski, E., and Balla, T. (2015). Phosphatidylinositol-Phosphatidic Acid Exchange by Nir2 at ER-PM Contact Sites Maintains Phosphoinositide Signaling Competence. Dev Cell *33*, 549–561.

King, C., Sengupta, P., Seo, A.Y., and Lippincott-Schwartz, J. (2020). ER membranes exhibit phase behavior at sites of organelle contact. Proc Natl Acad Sci USA *117*, 7225–7235.

Knittelfelder, O.L., Weberhofer, B.P., Eichmann, T.O., Kohlwein, S.D., and Rechberger, G.N. (2014). A versatile ultra-high performance LC-MS method for lipid profiling. Journal of Chromatography B *951–952*, 119–128.

Kojima, R., Endo, T., and Tamura, Y. (2016). A phospholipid transfer function of ER-mitochondria encounter structure revealed in vitro. Sci Rep *6*, 30777.

Konige, M., Wang, H., and Sztalryd, C. (2014). Role of adipose specific lipid droplet proteins in maintaining whole body energy homeostasis. Biochim Biophys Acta *1842*, 393–401.

Kornmann, B., Currie, E., Collins, S.R., Schuldiner, M., Nunnari, J., Weissman, J.S., and Walter, P. (2009). An ER-mitochondria tethering complex revealed by a synthetic biology screen. Science *325*, 477–481.

Kory, N., Farese, R.V., and Walther, T.C. (2016). Targeting Fat: Mechanisms of Protein Localization to Lipid Droplets. Trends in Cell Biology *26*, 535–546.

Kotapati, H.K., and Bates, P.D. (2020). Normal phase HPLC method for combined separation of both polar and neutral lipid classes with application to lipid metabolic flux. J Chromatogr B Analyt Technol Biomed Life Sci *1145*, 122099.

Krahmer, N., Farese, R.V., and Walther, T.C. (2013). Balancing the fat: lipid droplets and human disease. EMBO Mol Med *5*, 973–983.

Kremer, J.R., Mastronarde, D.N., and McIntosh, J.R. (1996). Computer visualization of three-dimensional image data using IMOD. J. Struct. Biol. *116*, 71–76.

Kroon, P.A. (1981). The order-disorder transition of the core cholesteryl esters of human plasma low density lipoprotein. A proton nuclear magnetic resonance study. J. Biol. Chem. *256*, 5332–5339.

Kühlbrandt, W. (2015). Structure and function of mitochondrial membrane protein complexes. BMC Biol *13*, 89.

Kumar, N., Leonzino, M., Hancock-Cerutti, W., Horenkamp, F.A., Li, P., Lees, J.A., Wheeler, H., Reinisch, K.M., and De Camilli, P. (2018). VPS13A and VPS13C are lipid transport proteins differentially localized at ER contact sites. J Cell Biol *217*, 3625–3639.

Kvam, E. (2004). Nvj1p is the outer-nuclear-membrane receptor for oxysterol-binding protein homolog Osh1p in Saccharomyces cerevisiae. Journal of Cell Science *117*, 4959–4968.

Kvam, E., Gable, K., Dunn, T.M., and Goldfarb, D.S. (2005). Targeting of Tsc13p to nucleus-vacuole junctions: a role for very-long-chain fatty acids in the biogenesis of microautophagiv vesicles. MBoC *16*, 3987–3998.

Lang, A.B., Peter, A.T.J., Walter, P., and Kornmann, B. (2015). ER–mitochondrial junctions can be bypassed by dominant mutations in the endosomal protein Vps13. Journal of Cell Biology *210*, 883–890.

Lang, M.J., Martinez-Marquez, J.Y., Prosser, D.C., Ganser, L.R., Buelto, D., Wendland, B., and Duncan, M.C. (2014). Glucose starvation inhibits autophagy via vacuolar hydrolysis and induces plasma membrane internalization by down-regulating recycling. The Journal of Biological Chemistry *289*, 16736–16747.

Lange, M., Wagner, P.V., and Fedorova, M. (2021). Lipid composition dictates the rate of lipid peroxidation in artificial lipid droplets. Free Radical Research 1–12.

Leapman, R.D., and Sun, S. (1995). Cryo-electron energy loss spectroscopy: observations on vitrified hydrated specimens and radiation damage. Ultramicroscopy *59*, 71–79.

Leber, R., Zinser, E., Zellnig, G., Paltauf, F., and Daum, G. (1994). Characterization of lipid particles of the yeast, Saccharomyces cerevisiae. Yeast (Chichester, England) *10*, 1421–1428.

Leber, R., Landl, K., Zinser, E., Ahorn, H., Spök, A., Kohlwein, S.D., Turnowsky, F., and Daum, G. (1998). Dual localization of squalene epoxidase, Erg1p, in yeast reflects a relationship between the endoplasmic reticulum and lipid particles. Mol Biol Cell *9*, 375–386.

Lee, S., and Min, K.-T. (2018). The Interface Between ER and Mitochondria: Molecular Compositions and Functions. Mol Cells *41*, 1000–1007.

Lees, J.A., and Reinisch, K.M. (2020). Inter-organelle lipid transfer: a channel model for Vps13 and chorein-N motif proteins. Curr Opin Cell Biol *65*, 66–71.

Lev, S. (2012). Nonvesicular lipid transfer from the endoplasmic reticulum. Cold Spring Harb Perspect Biol *4*.

Lobo-Jarne, T., and Ugalde, C. (2018). Respiratory chain supercomplexes: Structures, function and biogenesis. Seminars in Cell & Developmental Biology *76*, 179–190.

Lord, C.L., and Wente, S.R. (2020). Nuclear envelope–vacuole contacts mitigate nuclear pore complex assembly stress. Journal of Cell Biology *219*, e202001165.

Loring, H.S., Czech, V.L., Icso, J.D., O'Connor, L., Parelkar, S.S., Byrne, A.B., and Thompson, P.R. (2021). A phase transition enhances the catalytic activity of SARM1, an NAD+ glycohydrolase involved in neurodegeneration. ELife *10*, e66694.

Lowther, J., Naismith, J.H., Dunn, T.M., and Campopiano, D.J. (2012). Structural, mechanistic and regulatory studies of serine palmitoyltransferase. Biochem Soc Trans *40*, 547–554.

Lucken-Ardjomande Häsler, S., Vallis, Y., Jolin, H.E., McKenzie, A.N., and McMahon, H.T. (2014). GRAF1a is a brain-specific protein that promotes lipid droplet clustering and growth, and is enriched at lipid droplet junctions. Journal of Cell Science *127*, 4602–4619.

Lundberg, B. (1985). Chemical composition and physical state of lipid deposits in atherosclerosis. Atherosclerosis *56*, 93–110.

Luo, J., Yang, H., and Song, B.-L. (2020). Mechanisms and regulation of cholesterol homeostasis. Nat Rev Mol Cell Biol *21*, 225–245.

Lynch, E.M., Hicks, D.R., Shepherd, M., Endrizzi, J.A., Maker, A., Hansen, J.M., Barry, R.M., Gitai, Z., Baldwin, E.P., and Kollman, J.M. (2017). Human CTP synthase filament structure reveals the active enzyme conformation. Nat Struct Mol Biol *24*, 507–514.

Mahamid, J., Tegunov, D., Maiser, A., Arnold, J., Leonhardt, H., Plitzko, J.M., and Baumeister, W. (2019). Liquid-crystalline phase transitions in lipid droplets are related to cellular states and specific organelle association. Proc Natl Acad Sci USA *116*, 16866–16871.

Manford, A.G., Stefan, C.J., Yuan, H.L., Macgurn, J.A., and Emr, S.D. (2012). ER-to-plasma membrane tethering proteins regulate cell signaling and ER morphology. Dev Cell *23*, 1129–1140.

Manik, M.K., Yang, H., Tong, J., and Im, Y.J. (2017). Structure of Yeast OSBP-Related Protein Osh1 Reveals Key Determinants for Lipid Transport and Protein Targeting at the Nucleus-Vacuole Junction. Structure *25*, 617-629.e3.

Mannik, J., Meyers, A., and Dalhaimer, P. (2014). Isolation of Cellular Lipid Droplets: Two Purification Techniques Starting from Yeast Cells and Human Placentas. JoVE 50981.

Marini, G., Nüske, E., Leng, W., Alberti, S., and Pigino, G. (2020). Reorganization of budding yeast cytoplasm upon energy depletion. Molecular Biology of the Cell *31*, 1232–1245.

Mastronarde, D.N. (2005). Automated electron microscope tomography using robust prediction of specimen movements. J. Struct. Biol. *152*, 36–51.

Meredith, M.J., and Lane, M.D. (1978). Acetyl-CoA carboxylase. Evidence for polymeric filament to protomer transition in the intact avian liver cell. J. Biol. Chem. *253*, 3381–3383.

Michel, A.H., and Kornmann, B. (2012). The ERMES complex and ER-mitochondria connections. Biochem Soc Trans *40*, 445–450.

Mikoshiba, K. (2007). The IP3 receptor/Ca2+ channel and its cellular function. Biochem Soc Symp 9–22.

Millen, J.I., Pierson, J., Kvam, E., Olsen, L.J., and Goldfarb, D.S. (2008). The Luminal N-Terminus of Yeast Nvj1 is an Inner Nuclear Membrane Anchor. Traffic *9*, 1653–1664.

Mirheydari, M., Dey, P., Stukey, G.J., Park, Y., Han, G.-S., and Carman, G.M. (2020). The Spo7 sequence LLI is required for Nem1-Spo7/Pah1 phosphatase cascade function in yeast lipid metabolism. J Biol Chem *295*, 11473–11485.

Moldavski, O., Amen, T., Levin-Zaidman, S., Eisenstein, M., Rogachev, I., Brandis, A., Kaganovich, D., and Schuldiner, M. (2015). Lipid Droplets Are Essential for Efficient Clearance of Cytosolic Inclusion Bodies. Developmental Cell *33*, 603–610.

Montesinos, J., and Area-Gomez, E. (2020). Isolation of mitochondria-associated ER membranes. Methods Cell Biol *155*, 33–44.

Moser von Filseck, J., opi, A., Delfosse, V., Vanni, S., Jackson, C.L., Bourguet, W., and Drin, G. (2015). Phosphatidylserine transport by ORP/Osh proteins is driven by phosphatidylinositol 4-phosphate. Science *349*, 432–436.

Mullen, T.D., Hannun, Y.A., and Obeid, L.M. (2012). Ceramide synthases at the centre of sphingolipid metabolism and biology. Biochem J *441*, 789–802.

Munder, M.C., Midtvedt, D., Franzmann, T., Nüske, E., Otto, O., Herbig, M., Ulbricht, E., Müller, P., Taubenberger, A., Maharana, S., et al. (2016). A pH-driven transition of the cytoplasm from a fluid- to a solid-like state promotes entry into dormancy. ELife *5*, e09347.

Murley, A., Sarsam, R.D., Toulmay, A., Yamada, J., Prinz, W.A., and Nunnari, J. (2015). Ltc1 is an ER-localized sterol transporter and a component of ER–mitochondria and ER–vacuole contacts. Journal of Cell Biology *209*, 539–548.

Murphy, S.E., and Levine, T.P. (2016). VAP, a Versatile Access Point for the Endoplasmic Reticulum: Review and analysis of FFAT-like motifs in the VAPome. Biochimica et Biophysica Acta (BBA) - Molecular and Cell Biology of Lipids *1861*, 952–961.

Naito, T., Ercan, B., Krshnan, L., Triebl, A., Koh, D.H.Z., Wei, F.-Y., Tomizawa, K., Torta, F.T., Wenk, M.R., and Saheki, Y. (2019). Movement of accessible plasma membrane cholesterol by the GRAMD1 lipid transfer protein complex. ELife *8*, e51401.

Nguyen, T.T., Lewandowska, A., Choi, J.-Y., Markgraf, D.F., Junker, M., Bilgin, M., Ejsing, C.S., Voelker, D.R., Rapoport, T.A., and Shaw, J.M. (2012). Gem1 and ERMES do not directly affect phosphatidylserine transport from ER to mitochondria or mitochondrial inheritance. Traffic *13*, 880–890.

Ohsaki, Y., Cheng, J., Fujita, A., Tokumoto, T., and Fujimoto, T. (2006). Cytoplasmic lipid droplets are sites of convergence of proteasomal and autophagic degradation of apolipoprotein B. Molecular Biology of the Cell *17*, 2674–2683.

Olarte, M.-J., Kim, S., Sharp, M.E., Swanson, J.M.J., Farese, R.V., and Walther, T.C. (2020). Determinants of Endoplasmic Reticulum-to-Lipid Droplet Protein Targeting. Dev Cell *54*, 471-487.e7.

Olzmann, J.A., and Carvalho, P. (2019). Dynamics and functions of lipid droplets. Nat. Rev. Mol. Cell Biol. *20*, 137–155.

Pan, X., Roberts, P., Chen, Y., Kvam, E., Shulga, N., Huang, K., Lemmon, S., and Goldfarb, D.S. (2000). Nucleus–Vacuole Junctions in *Saccharomyces cerevisiae* Are Formed Through the Direct Interaction of Vac8p with Nvj1p. MBoC *11*, 2445–2457.

Park, C.K., and Horton, N.C. (2019). Structures, functions, and mechanisms of filament forming enzymes: a renaissance of enzyme filamentation. Biophys Rev *11*, 927–994.

Park, W.-J., and Park, J.-W. (2020). The role of sphingolipids in endoplasmic reticulum stress. FEBS Lett *594*, 3632–3651.

Parton, R.G., Tillu, V.A., and Collins, B.M. (2018). Caveolae. Curr Biol *28*, R402–R405.

Pedley, A.M., and Benkovic, S.J. (2018). Detecting Purinosome Metabolon Formation with Fluorescence Microscopy. In Protein Complex Assembly, J.A. Marsh, ed. (New York, NY: Springer New York), pp. 279–289.

Peeples, W., and Rosen, M.K. (2021). Mechanistic dissection of increased enzymatic rate in a phase-separated compartment. Nat Chem Biol *17*, 693–702.

Petrovska, I., Nüske, E., Munder, M.C., Kulasegaran, G., Malinovska, L., Kroschwald, S., Richter, D., Fahmy, K., Gibson, K., Verbavatz, J.-M., et al. (2014). Filament formation by metabolic enzymes is a specific adaptation to an advanced state of cellular starvation. ELife *3*, e02409.

Phair, R.D., and Misteli, T. (2000). High mobility of proteins in the mammalian cell nucleus. Nature *404*, 604–609.

Porter, K.R., Claude, A., and Fullam, E.F. (1945). A STUDY OF TISSUE CULTURE CELLS BY ELECTRON MICROSCOPY : METHODS AND PRELIMINARY OBSERVATIONS. J Exp Med *81*, 233–246.

Prévost, C., Sharp, M.E., Kory, N., Lin, Q., Voth, G.A., Farese, R.V., and Walther, T.C. (2018). Mechanism and Determinants of Amphipathic Helix-Containing Protein Targeting to Lipid Droplets. Dev Cell *44*, 73-86.e4.

Pronk, J.T., Yde Steensma, H., and Van Dijken, J.P. (1996). Pyruvate metabolism in Saccharomyces cerevisiae. Yeast *12*, 1607–1633.

Puchulu-Campanella, E., Chu, H., Anstee, D.J., Galan, J.A., Tao, W.A., and Low, P.S. (2013). Identification of the Components of a Glycolytic Enzyme Metabolon on the Human Red Blood Cell Membrane. Journal of Biological Chemistry *288*, 848–858.

Quesney-Huneeus, V., Galick, H.A., Siperstein, M.D., Erickson, S.K., Spencer, T.A., and Nelson, J.A. (1983). The dual role of mevalonate in the cell cycle. J Biol Chem *258*, 378–385.

Radhakrishnan, A., Goldstein, J.L., McDonald, J.G., and Brown, M.S. (2008). Switch-like Control of SREBP-2 Transport Triggered by Small Changes in ER Cholesterol: A Delicate Balance. Cell Metabolism *8*, 512–521.

Rayermann, S.P., Rayermann, G.E., Cornell, C.E., Merz, A.J., and Keller, S.L. (2017). Hallmarks of Reversible Separation of Living, Unperturbed Cell Membranes into Two Liquid Phases. Biophysical Journal *113*, 2425–2432.

Roberts, M.A., and Olzmann, J.A. (2020). Protein Quality Control and Lipid Droplet Metabolism. Annu. Rev. Cell Dev. Biol. *36*, 115–139.

Roberts, P., Moshitch-Moshkovitz, S., Kvam, E., O'Toole, E., Winey, M., and Goldfarb, D.S. (2003). Piecemeal Microautophagy of Nucleus in *Saccharomyces cerevisiae*. MBoC *14*, 129–141.

Rodwell, V.W., Nordstrom, J.L., and Mitschelen, J.J. (1976). Regulation of HMG-CoA reductase. Adv Lipid Res *14*, 1–74.

Rogers, S., Hariri, H., Wood, N.E., Speer, N.O., and Henne, W.M. (2021). Glucose restriction drives spatial reorganization of mevalonate metabolism. ELife *10*, e62591.

Romanauska, A., and Köhler, A. (2018). The Inner Nuclear Membrane Is a Metabolically Active Territory that Generates Nuclear Lipid Droplets. Cell *174*, 700-715.e18.

Ross, R. (1993). The pathogenesis of atherosclerosis: a perspective for the 1990s. Nature *362*, 801–809.

Ruiz, J.I., and Ochoa, B. (1997). Quantification in the subnanomolar range of phospholipids and neutral lipids by monodimensional thin-layer chromatography and image analysis. J Lipid Res *38*, 1482–1489.

Santinho, A., Chorlay, A., Foret, L., and Thiam, A.R. (2021). Fat inclusions strongly alter membrane mechanics. Biophysical Journal *120*, 607–617.

Sassa, T., and Kihara, A. (2014). Metabolism of very long-chain Fatty acids: genes and pathophysiology. Biomol Ther (Seoul) *22*, 83–92.

Schmidt, C., Athenstaedt, K., Koch, B., Ploier, B., and Daum, G. (2013). Regulation of the yeast triacylglycerol lipase TGl3p by formation of nonpolar lipids. The Journal of Biological Chemistry *288*, 19939–19948.

Schulze, R.J., Sathyanarayan, A., and Mashek, D.G. (2017). Breaking fat: The regulation and mechanisms of lipophagy. Biochimica et Biophysica Acta (BBA) - Molecular and Cell Biology of Lipids *1862*, 1178–1187.

Seo, A.Y., Lau, P.-W., Feliciano, D., Sengupta, P., Gros, M.A.L., Cinquin, B., Larabell, C.A., and Lippincott-Schwartz, J. (2017). AMPK and vacuole-associated Atg14p orchestrate μ-lipophagy for energy production and long-term survival under glucose starvation. ELife *6*, e21690.

Shai, N., Yifrach, E., van Roermund, C.W.T., Cohen, N., Bibi, C., IJlst, L., Cavellini, L., Meurisse, J., Schuster, R., Zada, L., et al. (2018). Systematic mapping of contact sites reveals tethers and a function for the peroxisome-mitochondria contact. Nat Commun *9*, 1761.

Shimobayashi, S.F., and Ohsaki, Y. (2019). Universal phase behaviors of intracellular lipid droplets. Proc Natl Acad Sci USA *116*, 25440–25445.

Sohn, M., Korzeniowski, M., Zewe, J.P., Wills, R.C., Hammond, G.R.V., Humpolickova, J., Vrzal, L., Chalupska, D., Veverka, V., Fairn, G.D., et al. (2018). PI(4,5)P2 controls plasma membrane PI4P and PS levels via ORP5/8 recruitment to ER–PM contact sites. Journal of Cell Biology *217*, 1797–1813.

Sorger, D., and Daum, G. (2003). Triacylglycerol biosynthesis in yeast. Appl Microbiol Biotechnol *61*, 289–299.

Srere, P.A. (1972). IS THERE AN ORGANIZATION OF KREBS CYCLE ENZYMES IN THE MITOCHONDRIAL MATRIX? In Energy Metabolism and the Regulation of Metabolic Processes in Mitochondria, (Elsevier), pp. 79–91.

Stefan, C.J., Manford, A.G., Baird, D., Yamada-Hanff, J., Mao, Y., and Emr, S.D. (2011). Osh Proteins Regulate Phosphoinositide Metabolism at ER-Plasma Membrane Contact Sites. Cell *144*, 389–401.

Stoddard, P.R., Lynch, E.M., Farrell, D.P., Dosey, A.M., DiMaio, F., Williams, T.A., Kollman, J.M., Murray, A.W., and Garner, E.C. (2020). Polymerization in the actin ATPase clan regulates hexokinase activity in yeast. Science *367*, 1039–1042.

Subramanian, K., Jochem, A., Le Vasseur, M., Lewis, S., Paulson, B.R., Reddy, T.R., Russell, J.D., Coon, J.J., Pagliarini, D.J., and Nunnari, J. (2019). Coenzyme Q biosynthetic proteins assemble in a substrate-dependent manner into domains at ER–mitochondria contacts. Journal of Cell Biology *218*, 1353–1369.

Sumegi, B., Sherry, A.D., Malloy, C.R., Evans, C., and Srere, P.A. (1991). Is there tight channelling in the tricarboxylic acid cycle metabolon? Biochem Soc Trans *19*, 1002–1005.

Szkopińska, A., Rytka, J., Karst, F., and Palamarczyk, G. (1993). The deficiency of sterol biosynthesis in Saccharomyces cerevisiae affects the synthesis of glycosyl derivatives of dolichyl phosphates. FEMS Microbiol Lett *112*, 325–328.

Thiam, A.R., Farese Jr, R.V., and Walther, T.C. (2013). The biophysics and cell biology of lipid droplets. Nat Rev Mol Cell Biol *14*, 775–786.

Tong, J., Manik, M.K., and Im, Y.J. (2018). Structural basis of sterol recognition and nonvesicular transport by lipid transfer proteins anchored at membrane contact sites. Proc Natl Acad Sci U S A *115*, E856–E865.

Tosal-Castano, S., Peselj, C., Kohler, V., Habernig, L., Berglund, L.L., Ebrahimi, M., Vögtle, F.-N., Höög, J., Andréasson, C., and Büttner, S. (2021). Snd3 controls nucleus-vacuole junctions in response to glucose signaling. Cell Reports *34*, 108637.

Touchstone, J.C. (1995). Thin-layer chromatographic procedures for lipid separation. Journal of Chromatography B: Biomedical Sciences and Applications *671*, 169–195.

Toulmay, A., and Prinz, W.A. (2013). Direct imaging reveals stable, micrometer-scale lipid domains that segregate proteins in live cells. Journal of Cell Biology *202*, 35–44.

Trotter, P.J. (2001). The genetics of fatty acid metabolism in Saccharomyces cerevisiae. Annu Rev Nutr *21*, 97–119.

Turunen, M., Olsson, J., and Dallner, G. (2004). Metabolism and function of coenzyme Q. Biochimica et Biophysica Acta (BBA) - Biomembranes *1660*, 171–199.

Valm, A.M., Cohen, S., Legant, W.R., Melunis, J., Hershberg, U., Wait, E., Cohen, A.R., Davidson, M.W., Betzig, E., and Lippincott-Schwartz, J. (2017). Applying systems-level spectral imaging and analysis to reveal the organelle interactome. Nature *546*, 162–167.

Vance, J.E. (1990). Phospholipid synthesis in a membrane fraction associated with mitochondria. J. Biol. Chem. *265*, 7248–7256.

Vance, J.E. (2015). Phospholipid Synthesis and Transport in Mammalian Cells. Traffic *16*, 1–18.

Voeltz, G.K., Rolls, M.M., and Rapoport, T.A. (2002). Structural organization of the endoplasmic reticulum. EMBO Rep *3*, 944–950.

Wakil, S.J., Stoops, J.K., and Joshi, V.C. (1983). Fatty acid synthesis and its regulation. Annu Rev Biochem *52*, 537–579.

Walther, T.C., Chung, J., and Farese, R.V. (2017). Lipid Droplet Biogenesis. Annu Rev Cell Dev Biol *33*, 491–510.

Wang, M., and Casey, P.J. (2016). Protein prenylation: unique fats make their mark on biology. Nat Rev Mol Cell Biol *17*, 110–122.

Wang, H., Becuwe, M., Housden, B.E., Chitraju, C., Porras, A.J., Graham, M.M., Liu, X.N., Thiam, A.R., Savage, D.B., Agarwal, A.K., et al. (2016). Seipin is required for converting nascent to mature lipid droplets. ELife *5*, e16582.

Webb, B.A., Dosey, A.M., Wittmann, T., Kollman, J.M., and Barber, D.L. (2017). The glycolytic enzyme phosphofructokinase-1 assembles into filaments. Journal of Cell Biology *216*, 2305–2313.

Wegner, M.-S., Schiffmann, S., Parnham, M.J., Geisslinger, G., and Grösch, S. (2016). The enigma of ceramide synthase regulation in mammalian cells. Prog Lipid Res *63*, 93–119.

Welte, M.A., and Gould, A.P. (2017). Lipid droplet functions beyond energy storage. Biochimica et Biophysica Acta (BBA) - Molecular and Cell Biology of Lipids *1862*, 1260–1272.

Wilfling, F., Wang, H., Haas, J.T., Krahmer, N., Gould, T.J., Uchida, A., Cheng, J.-X., Graham, M., Christiano, R., Fröhlich, F., et al. (2013). Triacylglycerol Synthesis Enzymes Mediate Lipid Droplet Growth by Relocalizing from the ER to Lipid Droplets. Developmental Cell *24*, 384–399.

Wong, A.K.O., Young, B.P., and Loewen, C.J.R. (2021). Ist2 recruits the lipid transporters Osh6/7 to ER–PM contacts to maintain phospholipid metabolism. Journal of Cell Biology *220*, e201910161.

Wood, N.E., and Doncic, A. (2019). A fully-automated, robust, and versatile algorithm for long-term budding yeast segmentation and tracking. PLoS ONE *14*, e0206395.

Wood, N.E., Kositangool, P., Hariri, H., Marchand, A.J., and Henne, W.M. (2020). Nutrient Signaling, Stress Response, and Inter-organelle Communication Are Non-canonical Determinants of Cell Fate. Cell Reports *33*, 108446.

Wu, W.-I., and Carman, G.M. (1996). Regulation of Phosphatidate Phosphatase Activity from the Yeast *Saccharomyces cerevisiae* by Phospholipids. Biochemistry *35*, 3790–3796.

Wu, H., Carvalho, P., and Voeltz, G.K. (2018). Here, there, and everywhere: The importance of ER membrane contact sites. Science *361*, eaan5835.

Wu, W.I., Lin, Y.P., Wang, E., Merrill, A.H., and Carman, G.M. (1993). Regulation of phosphatidate phosphatase activity from the yeast Saccharomyces cerevisiae by sphingoid bases. J Biol Chem *268*, 13830–13837.

Yaffe, M.P., and Kennedy, E.P. (1983). Intracellular phospholipid movement and the role of phospholipid transfer proteins in animal cells. Biochemistry *22*, 1497–1507.

Yang, H., Tong, J., Lee, C.W., Ha, S., Eom, S.H., and Im, Y.J. (2015). Structural mechanism of ergosterol regulation by fungal sterol transcription factor Upc2. Nat Commun *6*, 6129.

Yang, M., Li, C., Yang, S., Xiao, Y., Xiong, X., Chen, W., Zhao, H., Zhang, Q., Han, Y., and Sun, L. (2020). Mitochondria-Associated ER Membranes - The Origin Site of Autophagy. Front Cell Dev Biol *8*, 595.

Yang, Y., Lee, M., and Fairn, G.D. (2018). Phospholipid subcellular localization and dynamics. J Biol Chem *293*, 6230–6240.

Yu, J.W., and Lemmon, M.A. (2001). All phox homology (PX) domains from Saccharomyces cerevisiae specifically recognize phosphatidylinositol 3-phosphate. The Journal of Biological Chemistry *276*, 44179–44184.

Zaman, M.F., Nenadic, A., Radojičić, A., Rosado, A., and Beh, C.T. (2020). Sticking With It: ER-PM Membrane Contact Sites as a Coordinating Nexus for Regulating Lipids and Proteins at the Cell Cortex. Front. Cell Dev. Biol. *8*, 675.

Zechner, R., Madeo, F., and Kratky, D. (2017). Cytosolic lipolysis and lipophagy: two sides of the same coin. Nat Rev Mol Cell Biol *18*, 671–684.

Zewe, J.P., Wills, R.C., Sangappa, S., Goulden, B.D., and Hammond, G.R. (2018). SAC1 degrades its lipid substrate PtdIns4P in the endoplasmic reticulum to maintain a steep chemical gradient with donor membranes. ELife *7*, e35588.

Zhang, C., and Liu, P. (2017). The lipid droplet: A conserved cellular organelle. Protein Cell *8*, 796–800.

Zhang, P., and Reue, K. (2017). Lipin proteins and glycerolipid metabolism: Roles at the ER membrane and beyond. Biochimica et Biophysica Acta (BBA) - Biomembranes *1859*, 1583–1595.

Zhang, S., Wang, Y., Cui, L., Deng, Y., Xu, S., Yu, J., Cichello, S., Serrero, G., Ying, Y., and Liu, P. (2016). Morphologically and Functionally Distinct Lipid Droplet Subpopulations. Sci Rep *6*, 29539.

Zhang, Y., Beard, K.F.M., Swart, C., Bergmann, S., Krahnert, I., Nikoloski, Z., Graf, A., Ratcliffe, R.G., Sweetlove, L.J., Fernie, A.R., et al. (2017). Protein-protein interactions and metabolite channelling in the plant tricarboxylic acid cycle. Nat Commun *8*, 15212.

Zheng, S.Q., Palovcak, E., Armache, J.-P., Verba, K.A., Cheng, Y., and Agard, D.A. (2017). MotionCor2: anisotropic correction of beam-induced motion for improved cryo-electron microscopy. Nat. Methods *14*, 331–332.